

**Alma Mater Studiorum
Università di Bologna**

**DOTTORATO DI RICERCA IN
SCIENZE DELLA TERRA**

Ciclo XXV

Settore Concorsuale di afferenza: GEO 04

Settore Scientifico di afferenza: GEO 05

**Land use management in mountainous areas: combining
ground-based and EO (Earth Observation) data to in-
vestigate the shallow landsliding susceptibility in the
Duron valley (Trento, Italy)**

Presentata da: Dott.ssa Martina Chiara Morandi

Coordinatore Dottorato:
Prof. Roberto Barbieri

Relatori:
Prof. Enzo Farabegoli

Dott. Giuseppe Onorevoli

Esame finale anno 2013

ABSTRACT

Throughout the alpine domain, shallow landslides represent a serious geologic hazard, often causing severe damages to infrastructures, private properties, natural resources and in the most catastrophic events, threatening human lives. Landslides are a major factor of landscape evolution in mountainous and hilly regions and represent a critical issue for mountainous land management, since they cause loss of pastural lands.

In several alpine contexts, shallow landsliding distribution is strictly connected to the presence and condition of vegetation on the slopes.

With the aid of high-resolution satellite images, it's possible to divide automatically the mountainous territory in land cover classes, which contribute with different magnitude to the stability of the slopes.

The aim of this research is to combine EO (Earth Observation) land cover maps with ground based measurements of the land cover properties.

In order to achieve this goal, a new procedure has been developed to automatically detect grass mantle degradation patterns from satellite images. Moreover, innovative surveying techniques and instruments are tested to measure *in situ* the shear strength of grass mantle and the geomechanical and geotechnical properties of these alpine soils.

Shallow landsliding distribution is assessed with the aid of physically-based models, which use the EO-based map to distribute the resistance parameters across the landscape.

ABSTRACT

In tutto l'arco alpino, le frane superficiali rappresentano un rischio estremamente attuale che ogni anno causa ingenti danni alle infrastrutture, alle proprietà e, nei casi più tragici, provocano perdite umane.

Le frane superficiali rappresentano un importante fattore di evoluzione del paesaggio alpino in quanto provocano perdita di suolo e modificano quindi la distribuzione dei terreni adibiti al pascolo. L'analisi dei meccanismi di innesco delle frane superficiali e la loro distribuzione, deve essere condotta partendo da una profonda conoscenza dei parametri geomeccanici che caratterizzano il suolo e soprassuolo. Nell'area di studio, un bacino montano situato tra i 1900 e i 2400 m s.l.m., la maggior parte dei versanti è ricoperta da un fitto manto erboso: il *Nardetum*; questa copertura vegetale tuttavia, presenta degli evidenti pattern di degradazione, causati dall'intensa attività pastorizia. Nelle zone in cui il manto erboso è danneggiato, le resistenze calano drasticamente, aumentando quindi la loro vulnerabilità al franamento superficiale.

L'obiettivo di questo lavoro è quello di combinare la suddivisione del territorio, fatta attraverso tecniche di classificazione automatica delle immagini satellitari alle proprietà geomeccaniche e geotecniche delle diverse coperture. La caratterizzazione di queste proprietà del suolo e soprassuolo è stata condotta utilizzando sia strumenti e metodi tradizionali, sia tecniche innovative e strumenti sperimentali.

Infine per studiare la distribuzione delle frane superficiali, i dati raccolti in campagna e suddivisi nelle diverse classi di copertura, sono stati inseriti in modelli di stabilità dei versanti.

Introduction

The alpine environment has always captured the attention of the scientific community because of its extraordinary beauty and the complexity of the physical processes that govern this environmental context.

Landslides, rock falls, floods, avalanches and all the surface processes that take place everyday in the Alps, make this environment an open-air laboratory for studying the physical processes which act on the landscape.

Given the roughness of the alpine terrains, geological and geomorphological surveys performed in these mountainous and remote sites require a great amount of time and conspicuous financial support.

In the past decades, an increasing attention focused on the use of remote sensed data to retrieve physical properties of terrains of difficult accessibility: Earth Observation (EO) data provide indeed an efficient way to investigate those sites and to detect features at electromagnetic wavelengths, which are not visible to the human eye. Satellite images provide the ability to analyze quantitatively multispectral bands and allows the application of computer processing routines to discern and enhance certain compositional properties of Earth surface. Nowadays, Earth Observation (EO) data are successfully used in many different fields such as environmental and urban planning, land use management and hazard assessment.

The Italian Space Agency (ASI) recently funded the “MORFEO” project (Monitoring Landslide Risk through Earth Observation technology), with the aim of developing a system for integrating EO technologies in the traditional methods for landslides investigation. The goal of MORFEO, is testing, evaluating and improving EO technologies at the service of the Civil Protection agency, for what concerns the landslide risk assessment.

My research has been partially conducted in the frame of the "MORFEO" project, which provided me with a large database of high-resolution satellite images.

One of the test areas chosen by this project is the upper part of the Duron valley, in the eastern Italian Dolomites. This small catchment (0.7 km²) represents a typical example of extreme alpine environment, lying in a high-altitude range (1900-2400 m a.s.l.) and covered by snow 8 months per year on average. The slopes of this basin are dissected by the scars of 18 shallow landslides, which involve only the uppermost part of the soil, and cover altogether 4.8% of the catchment area. The Duron basin, which is the study area of my research, is mostly covered by a very thick and extremely resistant grass mantle called *Nardetum*. This tenacious vegetative association is quite common throughout the alpine terrains: it took roots here after the Quaternary glaciations and adjusted since then to the evolving alpine environment.

Although in the past decades there has been an increasing effort in studying the root's shear strengths of shrubs and trees species (Bischetti et al., 2009; Martson, 2010), little attention has been paid to the geomechanical properties and resistances of the grass mantle (Comino and Druetta, 2009).

In the studied alpine context, the shear resistance of the grass mantle seems to play a fundamental role in the stability of the slopes: it is not uncommon to find 60° perfectly stable slopes, covered by undamaged *Nardetum*. Nevertheless, there are portions of the basin where the grass mantle is almost completely sheared and the geomechanical properties of the grass roots are therefore lowered. This is, for instance, the effect of cattle overgrazing, which in the alpine regions represents an important erosion factor (Descroix et al., 2008) since the presently intense pastoral activity has been documented from the Neolithic Age.

Given this alpine context, the issues that I'm going to tackle in my thesis are:

- 1) Which are the strengths of the different types of land cover classes?
- 2) Do remote sensing classification techniques provide reliable results in discriminating these

land use classes, at the catchment's scale?

3) How do these properties influence the shallow landsliding susceptibility predicted by the models?

In order to answer these questions, detailed geological, geomorphological and geotechnical surveys were performed in the study area. The vegetation resistances were measured with an innovative instrument, which measures *in situ* the shear strength of the grass mantle in different conditions of degradation. Finally, in order to combine the information retrieved from the EO data and the measurements performed in the field, physically based models were used to assess the influence of these parameters in the shallow landsliding distribution.

Bischetti, G.B., Chiaradia, E.A., Epis, T. and Morlotti, E., 2009. Root cohesion of forest species in the Italian Alps. *Plant and Soil*, 324(1-2), 71- 89.

Comino, E., Druetta, A., 2009. In situ shear tests of soil samples with grass roots in alpine environment. *American Journal of Environmental Sciences*, 5(4): 475-486.

Descroix, L., Barrios, J.L.G., Viramontes, D., Poulenard, J., Anaya, E., Esteves, M., and Estrada, J., 2008. Gully and sheet erosion on subtropical mountain slopes: their respective roles and the scale effect. *Catena*, 72(3): 325-339.

Marston, R.A., 2010. Geomorphology and vegetation on hillslopes: Interactions, dependencies, and feedback loops. *Geomorphology*, 116(3-4): 206-217.

Contents

| | | |
|----------|--|-----------|
| 1 | The Duron valley | 1 |
| 1.1 | Introduction | 1 |
| 1.2 | Geology | 2 |
| 1.3 | Geomorphology | 4 |
| 1.3.1 | Slopes, hollows and glacial morphology | 5 |
| 1.3.2 | Landslides and outcrops | 7 |
| 1.3.3 | Soils | 10 |
| 1.4 | Vegetation | 10 |
| 1.5 | Discussion | 12 |
| 1.6 | Conclusions | 14 |
| 2 | The cattle grazing effect on the landscape: automatic land cover classification using high-resolution remote sensing data | 19 |
| 2.1 | Introduction | 19 |
| 2.2 | The cattle grazing effect on the landscape | 20 |
| 2.3 | Grazing in the Duron valley | 22 |
| 2.4 | Image processing | 23 |
| 2.4.1 | Image classification | 24 |
| 2.4.2 | Maximum likelihood classification | 24 |
| 2.5 | Vegetation indices | 26 |
| 2.6 | Land cover classification | 28 |
| 2.6.1 | Land cover classes | 29 |
| 2.6.2 | Maximum likelihood classification | 31 |
| 2.7 | Results and discussion | 32 |
| 2.8 | Conclusions | 33 |

| | | |
|----------|--|-----------|
| 3 | Geomechanical and hydrological soil properties of the Duron valley . . . | 38 |
| 3.1 | Introduction | 38 |
| 3.2 | Soil depth | 39 |
| 3.3 | Laboratory analyses | 40 |
| 3.4 | Vane measurements | 42 |
| 3.4.1 | Water content and Guelph permeameter | 44 |
| 3.5 | Results and discussion | 45 |
| 3.6 | Conclusions | 48 |
| 3.7 | References | 50 |
| 4 | The “Turf’s comb”, a new in situ device to measure the shear resistance of the grass mantle: preliminary results and applications | 52 |
| 4.1 | Abstract | 52 |
| 4.2 | Introduction | 53 |
| 4.3 | Materials and methods | 54 |
| 4.4 | Results | 59 |
| 4.5 | Discussion | 67 |
| 4.6 | Conclusion | 69 |
| 4.7 | References | 71 |
| 5 | Hillslope stability analysis: merging EO (Earth Observation) and ground- based data | 74 |
| 5.1 | Introduction | 74 |
| 5.2 | SHALSTAB | 75 |
| 5.2.1 | The hydrological model | 76 |
| 5.2.2 | The slope stability model | 76 |
| 5.2.3 | Data set | 80 |
| 5.2.4 | Results | 82 |
| 5.2.5 | Shalstab with the soil depth map | 86 |
| 5.3 | TRIGRS | 90 |
| 5.3.1 | The hydrological model | 90 |

| | | |
|----------|-------------------------------------|------------|
| 5.3.2 | The slope stability model | 91 |
| 5.3.3 | Data set | 92 |
| 5.3.4 | Results | 93 |
| 5.4 | SLIDE | 96 |
| 5.4.1 | Vegetation cover | 97 |
| 5.4.2 | Slope stability model | 97 |
| 5.4.3 | Results | 98 |
| 5.5 | Discussion | 99 |
| 5.6 | Conclusions | 102 |
| 5.7 | References | 104 |
| 6 | Conclusions | 107 |

CHAPTER 1

The Duron valley

1.1 Introduction

¹ The study area is a small alpine catchment in the eastern Italian Dolomites (Fig.1.1), in that portion of the Italian southern Alps, which has been recently added to the UNESCO's World Heritage list (2009). This catchment (0.7 km²) is the northern most sub-basin of a broader valley (Duron), which elongates in the E-W direction between the provinces of Trento and Bolzano (46° 29'37" N, 11° 39'25" E)(Fig 1.2). Located in one of the most spectacular alpine scenery, the area is surrounded by the massive carbonatic platforms of the Sella and Catinaccio formations and lies on late Ladinian volcanic products. During the last ice age, the thick ice lobes that run beneath the Triassic platforms shaped the valley and left evident signs of glacial ablation and deposition. This chapter aims at describing the geology, geomorphology, soils and vegetation of the study area, postponing more technical descriptions (geomechanics and geotechnics of the soils) to the following chapters.

¹ *This chapter constitutes part of the article by E. Farabegoli, M. C. Morandi, G. Onorevoli and D. Tonidandel: "Geotechnical properties and root reinforcement of soil in a grass mantled Alpine test catchment (Duron valley, Dolomites, Italy)." Submitted to Geomorphology, Elsevier.*



Figure 1.1: View of the Duron valley from the southern side of the Col Rodella mount. The red polyline encloses the study area.

1.2 Geology

The Dolomites are located in the eastern part of the Southern Alps; they're limited to the north by the Periadriatic lineament (Insubric line) and to the south by south-vergent Valsugana overthrust (Leonardi, 1967; Doglioni, 1987, Bosellini, 2003). The central part of the Dolomites is located on a large pop-up synclinorium of the crystalline basement limited to the south by the Val Sugana overthrust and to the north by the Funes conjugate back thrust (Fig. 1.3).

The Duron valley is surrounded by the triassic carbonatic platforms (Sella, Sassolungo, Sciliar and Catinaccio), which in between, comprise a series of anticline-syncline, E-W trending (Note illustrative Carta Geologica d'Italia 1:50.000, Foglio Marmolada). In this complex structural setting, the study area lies between the Sella syncline, which represents the eastern margin of the Siusi syncline and the Tires line (Fig. 1.4). According to the tectonic scheme in fig. 1.4, the Tires normal fault runs along the western side of the study area and follows the lithostratigraphic boundary between the Catinaccio formation (carbonates) and the Fernazza

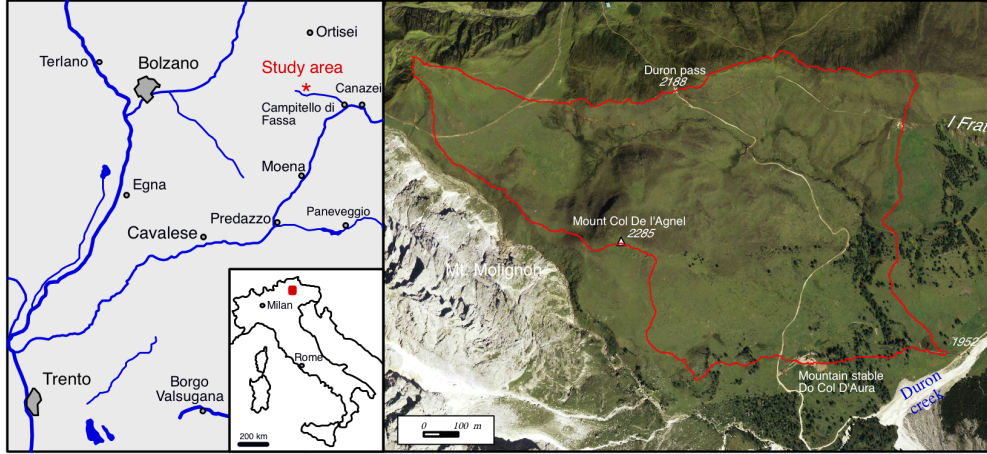


Figure 1.2: Location of the study area (0.7 km²)

volcanic products. During our field surveys we didn't observe any sign of tectonic activity along this margin; we consider therefore the contact between the carbonate and the volcanic breccias to be stratigraphic, not tectonic.

During the past century, many authors studied the geology of the Fassa valley (Castiglioni et al., 1930; Leonardi et al., 1970; Viel, 1979; Masetti and Neri, 1980; Doglioni, 1984; Bosellini, 1991; Brandner, 1991; Castellarin et al., 1998; Neri and Stefani, 1998; Stefani and Caputo, 1998; Trombetta and Bottoli, 1998; Castellarin et al., 2004; Brandner et al., 2007) and several contrasting stratigraphical and tectonic schemes have been proposed to explain the complex geological setting of the Fassa area.

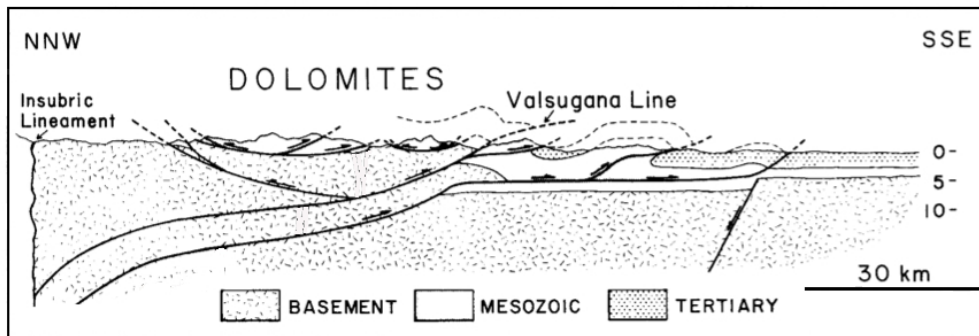


Figure 1.3: Section of the southern Alps, modified from Doglioni, 1987.

To overcome this problem, we performed detailed geologic, geomorphological and land cover maps based on both terrain surveys and interpretation of orthophotos and GeoEye satellite images. All the maps we produced were georeferenced on 2m cell-sized DEM obtained from LiDAR survey (2006).

The geological succession in the study area, ca. 1000 m thick, is entirely represented by Ladinian (Middle Triassic) units (Fig. 1.5). The Catinaccio Formation (i.e. the oldest one) is a dolomitic breccia settled as stacked clinofolds dipping 30°-40° E and NE, which connected the peritidal carbonate facies with the basinal deep marine deposits. The succession changes rapidly upward to volcanic deposits of the Fernazza formation (upper Ladinian; Viel, 1979): pillow lavas, pillow breccias, hyaloclastites and volcanic turbidites dipping 15°-20° NNE. Some volcanic dikes crosscut the entire geological succession. The differential subsidence and the Alpine orogeny tilted the succession approx 10° NNE.

Several sets of disjunctive faults trending NNW- SSE and N-S offset the dolomitic clinofolds of the north-facing side of the Duron valley (Catinaccio d'Antermoia Massif) while orthoimages photo interpretation revealed the presence of N-S set of joints and sub-vertical faults just East of the study area.

1.3 Geomorphology

The geological setting influences strongly the geomorphological and hydrogeological configuration of the catchment, which looks, in plan view, as an irregularly shaped polygon. The hydrographic network is generally angular: surface and sub-surface flow directions are mostly governed by the contacts between lithostratigraphic units. In the northern part, where the bedrock is less permeable, the network becomes locally dendritic. Most of the channel heads are generated by surface runoff; only one is fed by a water spring (Fig.1.6) due to subsurface

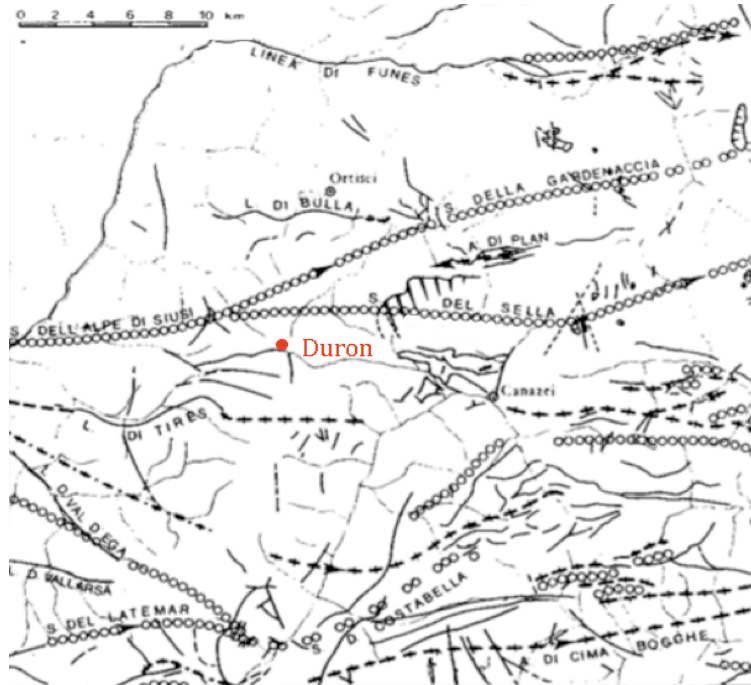


Figure 1.4: Tectonic scheme: the study area is marked with a red dot (Note illustrative *Carta Geologica d'Italia*, 1970).

flow through the bedrock. Generally, channels erode the soil and only in the steepest parts of the catchment incise the bedrock. At the basin outlet, the creek flows on the eastern side of a small alluvial fan. Nowadays, this channel is constrained by two artificial levees ca. 1 m high, a hundred meters before the affluence with the Duron creek.

1.3.1 Slopes, hollows and glacial morphology

Throughout the catchment area slopes are generally gentle (15° - 25°) made exception for the NW side of the basin and the southern side of the Col de l'Agnel, where the slope reaches 60° (Fig.1.7). Here, the narrow stream is incised ca 10 m, and down-slope is laterally confined by small terraces of first and second order. Two major elongated concave-upward structure oriented ca. E-W are located respectively on the northern and southern part of the catchment (Fig.1.6). In the central part, the volcanic bedrock (pillow lavas and pillow

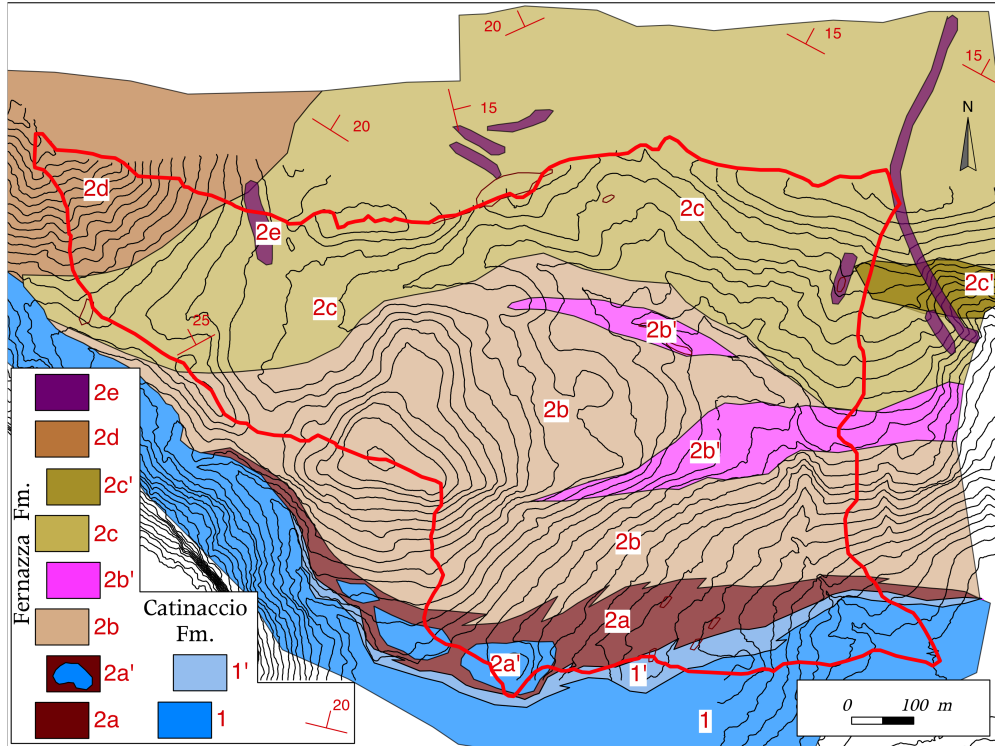


Figure 1.5: Geological map of the study area: 1) Catinaccio formation: doloarenites and dolorudites of carbonate platform: 1a) Carbonate platform slope facies with angular carbonatic clasts deposited on the slope; 2) Pillow breccias with dolomitic blocks; 2a) Pillow breccias with dolomitic blocks (2a'); 2b) pillow breccias; 2b') pillow lavas in lenticular bodies; 2c) Volcanic torbidites and pillow breccias; 2c') Hyaloclastites: centimetric to decimetric strata of gray arenites with volcanic glasses and abundant pyroxene crystals, mostly compacted to obtain a massive structure with concoidal exfoliation; 2d) Brecciated lavas, pillow breccias and hyaloclastite pockets in centimetric to decimetric beds. Submarine slump-induced deformations occur at the stratigraphic contact with the upper unit (the Fernazza hyaloclastites); 2e) Basaltic dykes.

breccias) is characterized by two small sized slightly concave-upward flats, and dome-shaped features surrounded by sub-rounded culminations (e.g. Col de l'Agnel). Glacial striations occur in the southern forms and indicate that the direction of flow of the glacial ice was south-eastward. Therefore, during the last glacial age, the steep southern side of the Col de l'Agnel separated two ice tongues which were fed by the glacier located on the eastern wall of the Mt. Molignon (Fig.1.1). The central part of the northern structure is filled by peaty soils, 1 to 2 m thick, while in the peripheral parts, peaty soils alternate vertically to distal debris of alluvial fans. Few perennial springs supply with water the larger concavities. At the end

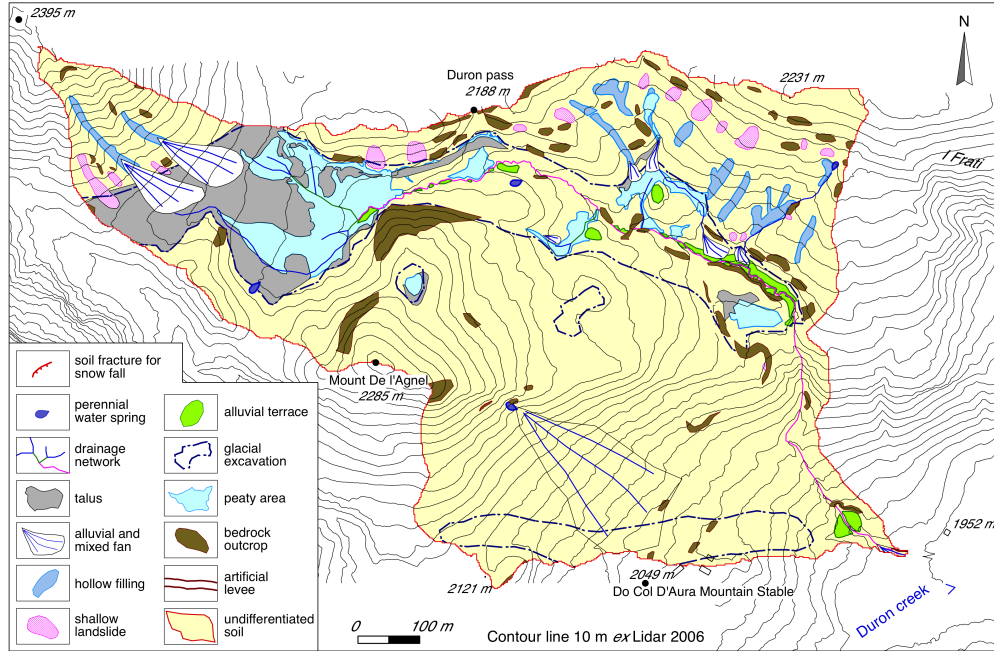


Figure 1.6: Geomorphological map of the study area. The contour lines interdistance is 10 m.

of winter, in autumn and during the heavy rainstorms, the ground water table reaches the surface generating ponds and peat bogs. Peaty areas experience a strong seasonality: they usually reach their maximum extent in May-June during snowmelt and heavy rainfalls but during dry years they might completely vanish. Channels of the second and third Strahler's order incised small alluvial terraced deposits; their top surface elevates respectively 1 and 3 m above the channel bed.

1.3.2 Landslides and outcrops

In the study area we surveyed 18 shallow landslides and several outcrops, covering altogether 4.8% of the catchment area (Table 1.1). The sliding mechanism is translational and they involve usually the uppermost part of the soil profile, down to 40 cm. Landslides width ranges from 5 to 20 m and their length ranges from 20 to 40 m, made exception for the western most landslide, whose length exceeds 100 m. Eleven landslides are located just upside

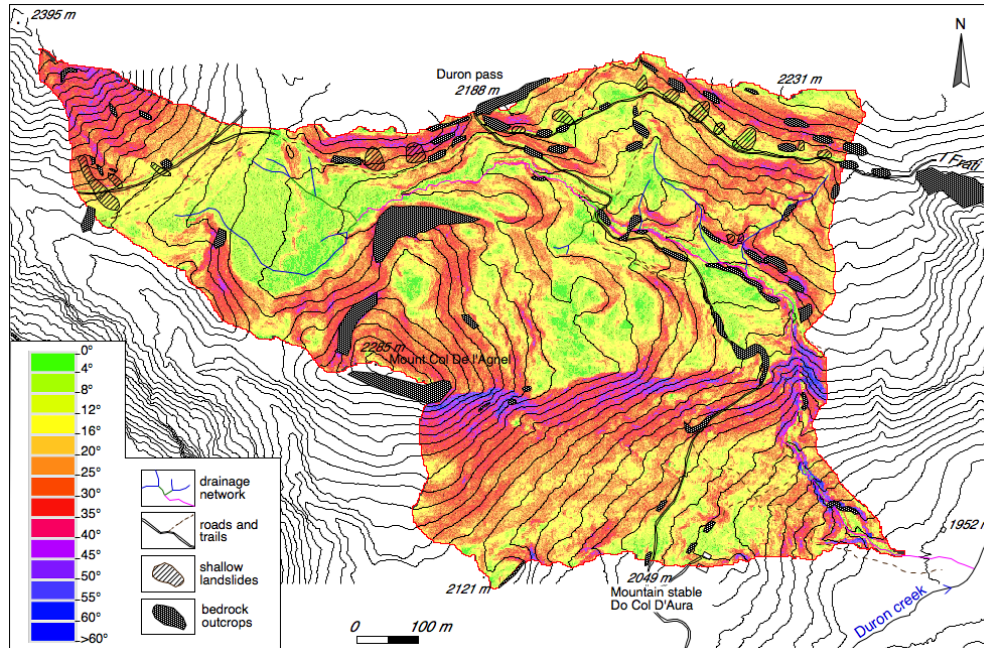


Figure 1.7: Slope map obtained from the Digital Terrain Model (2x2 m cell resolution).

the trail which crosses the northern part of the catchment in East-West direction (Fig.1.6). Their alignment to the trail suggests that their occurrence is related to the road cut. This trail was enlarged during WWI, to permit the transit of panzers, therefore the age of these mass movements is likely comprised in a 90 years time span. In the four years of surveys in this portion of the Duron valley, no landslide was observed. Contrarily, several debris flow occurred on both flanks of the Duron valley, outside the study area.

The landslide inventory, edited by the Trient province, reports only five shallow landslides in the eastern part of the study area, which doesn't match with the surveyed instability.

Outcrops cover 3.7% of the catchment area: the largest is located in the northeastern side of the Col de l'Agnel and is the sum of many small outcrops separated by thin stripes of soil. Most of the landslides and some bedrock outcrops are located along the northern side of the catchment, in correspondence of the volcanic-torbidites bedrock sloping 30°- 45°. The only exception is the big landslide scar on the southern side of the Col de L'Agnel (Fig.1.6). Here, at the end of February 2009, a thick cornice of snow, toppled and slid downward over

the steep slope ($>50^\circ$). The mass of compacted snow hit the grazed *Nardetum* at the slope break, in correspondence of the electrified fence. It tore and dragged the soil 1 m down slope along a composite front approx. 35 m wide.

The snow-avalanche uprooted some dozens of 10-30 years old swiss stone pines. Local witnesses claim that in the fifties a similar but major snow avalanche, reached and destroyed the old mountain stable “Do Col d’Aura”, that at that time was located upslope the road, at the foot of the large debris fan (Fig.1.6). These events demonstrate how snow-avalanches might contribute significantly to the formation of mixed debris fan (Gortani, 1912; Rovereto, 1924), even in medium sloped ($15^\circ - 30^\circ$) mountain areas.

In the southern part of the Duron valley, outside the study area, there are few debris flows, triggered by severe rainfall precipitations which usually occur in spring/summer.

A huge paleo-landslide, called “Ciaresoles” occupies the right flank of the valley: this enormous mass movement has a 950 m long lobate front which deflected the river path (Fig.1.1).

| Geomorphological form | Area (%) | Land cover/Land use | Area (%) |
|----------------------------|----------|---------------------------------|----------|
| Glacial forms | 28.6 | Heavily grazed Nardetum | 18.5 |
| Mixed fans | 6.7 | Undamaged grass cover | 2.6 |
| Distal fans, colluvium | 6.1 | Landslides, hollows fans, talus | 9 |
| Peats | 5.5 | Peats | 5.5 |
| Outcrops | 3.7 | Alluvial terraces | 4.5 |
| Hollows | 1.8 | Shrubs | 3.7 |
| Shallow landslide deposits | 1.1 | Trees | 1.2 |
| Alluvial terraces | 0.7 | Outcrops | 3.7 |
| | | Road, trails and edifices | 0.9 |

Table 1.1: Geomorphological forms and Land cover/ Land use classes distribution

1.3.3 Soils

Soils in the study area are Eutric Podzols (Endoskeletal) according to the FAO protocol (FAO, 1998; IUSS Working Group WRB, 2006); soils moisture regime is udic (soil is not dry in any part for as long as 90 cumulative days per year) and soil temperature regime is cryic (mean annual temperature $< 8^{\circ}\text{C}$ with no permafrost). Recent studies of soil profiles in the Fassa valley (Egli et al., 2010a, b) revealed that soils started to form 7000-5000 y.b.p. during the Atlantic stage. Geophysical surveys (described in details in chapter IV) indicate that the soil depth ranges from 0 to 200 cm and is on average 50 cm.

1.4 Vegetation

The Duron valley is located at the transition between two altitude belts: (1) the Subalpine belt (from 1500 to 2000 m a.s.l.) and (2) the Alpine belt (from 2000 to 2500 m a.s.l.). The vegetation distribution is mostly controlled by altitude, although several other factors influence the occurrence of specific species (sun exposition, wind, slope inclination, nature of bedrock, pedologic structure). Almost the entire study area is covered by grass (*Nardetum*), with sparse shrubs (junipers and rhododendron) and trees (firs, larches and pines). All these arctic-alpine species took roots here after the Quaternary glaciations and adjusted since then to the evolving alpine environment. *Nardetum* is a secondary grassland composed of few species of the *Familia Graminaceae*: *Nardus stricta*, *Agrostis tenuis*, *Anthoxanthum odoratum*, *Avenella flexuosa* and *Festuca nigrescens*. This vegetative association is not a nourishing pasture and is resistant to frost and partly to animal grazing, although intensive browsing causes the disappearance of the most sensitive species. *Nardus stricta*, the most frequent grass in the *Nardetum* vegetative association, is edible by cows and horses only in its juvenile stage: when becomes mature, it constitutes a very dense tuft which tends to

expand, overcoming the surrounding species. Usually, the *Nardetum*'s turf has an extremely dense, nearly impenetrable network of roots 10-15 cm long. Juniper (*Juniperus nana*) is widespread and represents the only species of shrubby grassland remained due to its scarce edibility. Rhododendron (*Rhododendron hyrsutum*), a toxic species for domestic animals, is almost absent, because in the last decades, shepherds have systematically uprooted it and rare specimens live protected into juniper shrubs. With the aid of high-resolution aerophotographs (60 cm), we mapped 2662 shrubs and 722 trees (respectively 3.7% and 1.2% of the total area), mostly swiss stone pines (*Pinus cembra*), few larches (*Larix decidua*) and spruce firs (*Picea abies*). On the map (Fig. 1.8), each plant is represented by a circle which diameter corresponds to the tree crown or shrub dimension.

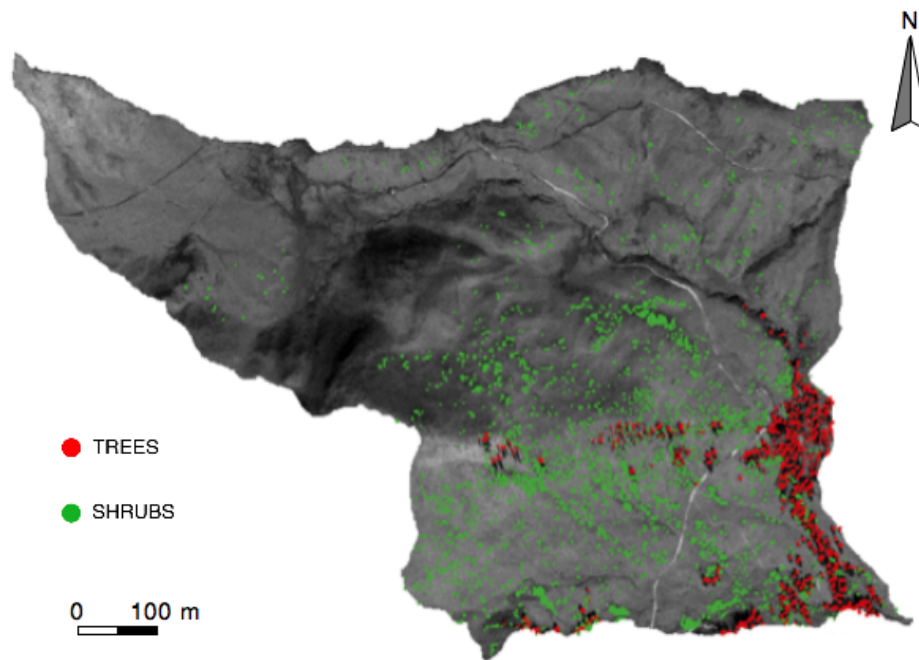


Figure 1.8: Distribution of trees and shrubs in the study area

1.5 Discussion

The alpine context of the study area represent one of the few pastureland where the land use hasn't changed in the last centuries. Many of the neighboring valleys indeed have been exploited for ski resorts: the touristic activity changed deeply the geomorphology of the slopes and modified the hydrologic network, which has to be controlled in order to provide artificial snow for the ski runs.

In the entire Duron area there are only 25 edifices, mostly made of wood, and there are very strict laws that forbid new constructions; as a result, the alpine landscape hasn't changed substantially in the past centuries. The upper part of the valley exhibits still the scars of WWI, when the austrian front was running along the northern watershed divide. Deep trenches and military roads are still visible throughout the catchment area and can also be easily noticed from the satellite images.

The only sign of natural landscape evolution is given by the landslides.

In the study area, the landslides can be referred to as translational shallow landslides, which involve only the upper part of the soil. The vast majority are related to road cuts and their surfaces rarely exceed 40 m². The volumes involved in the shallow landsliding process are limited, and dictated by the shallow depth of the soil.

The Duron valley represents a very good example of the influence of altitude and exposition on the distribution of the vegetative species.

The tree line is set at ca 2100 m a.s.l., above there are only shrubs (junipers and rhododendron) and grasslands (*Nardetum*). The wood forest is limited by the narrow gorge in the south-western part of the basin (2050-2100 m a.s.l.): here the tall trees (firs, larches and pines) live protected from the northern icy winds. Only few swiss stone pines sprout in the middle of the basin, at altitude of 2200 m a.s.l. (Fig.1.9).

The entire study area is mostly south-facing; this exposition of the valley's flanks exerts a

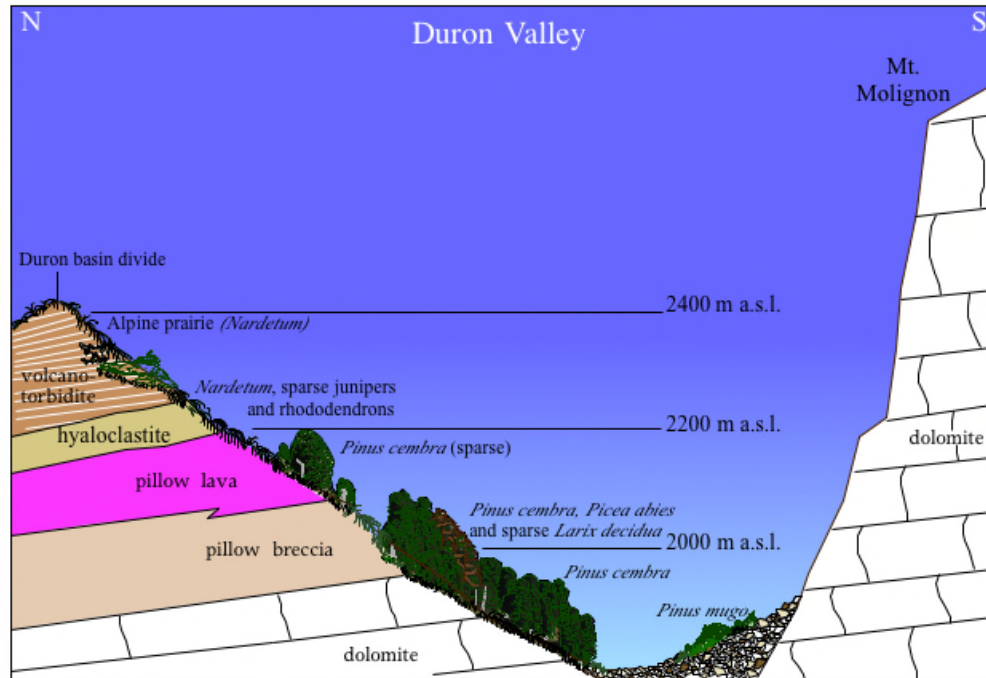


Figure 1.9: Distribution of the vegetation in the Duron valley (Modified from Reisigl and Keller, 1994).

strong control on the occurrence of vegetative species. For instance, the swiss stone pine (*Pinus mugo*) is present only on north-facing slopes, below the altitude of 2000 m a.s.l., just outside the borders of the study area.

In the north-eastern part of the basin we observed an ongoing phase of natural reforestation. Here, few young swiss stone pines (less than 1.5 m high) are present in the altitude belt of 2200 - 2250 m a.s.l., between the north-eastern grasslands and “*I Frati*” (“The friars”: a local and spectacular geofom developed into brown massive hyaloclastites composed of sub-rounded, 20-30 m high pinnacles).

1.6 Conclusions

This study area represents one of the few undamaged alpine environment in the entire Dolomites area, since the slopes haven't been jet exploited as ski resort. Therefore the influence of the geology of the bedrock on geomorphology, the effect of the last ice age on the landscape, and the natural degradation processes acting on the slopes can still be traced. In order to describe the setting of the study area, we produced a very detailed geological and a geomorphological map, as well as a map of the vegetation distribution. These products are the key components of this thesis: the maps can be used as "ground truth data" while dealing with satellite images interpretation and also as physical constrains while analyzing the landslide susceptibility across the landscape.

References

- Bosellini, A., 1991. Geology of the Dolomites, an introduction., Dolomieu Conference on carbonate platforms and dolomitization, Ortisei pp. 43.
- Bosellini, A., Gianolla, P., Stefani, M., 2003. Geology of the dolomites. Episodes 26, 181–185.
- Bottoli, S., Trombetta, G.L., 1998. Analisi di facies ed ambiente deposizionale del Conglomerato della Marmolada: un sistema torbido dominato da flussi ad alta densità (Gruppo Col Rossi- Porta Vescovo, Dolomiti occidentali). Mem. Soc. Geol. It., 53: 341-357.
- Brandner, R., 1991. Geological setting and Stratigraphy of the schlern-Rosengarten buildup and Seiser Alm basin. In: F.E. Brandner R., Koch R., Yose L.A. (Editor), Dolomieu Conference on Carbonate Platforms and Dolomitization. Guidebook excursion A, Ortisei, pp. 61.
- Brandner, R., Burger, U., Gögl, M.L., Gruber, A., Gruber, J., Jesacher, M., Keim, L., Pirchl, T., Prager, C., Psenner, A., Schmidt, M., 2007. Carta Geol. d'Italia F° 27 "Bolzano" scala 1: 50.000. Litografia artistica cartografica, Firenze.
- Castellarin, A., Selli, L., Picotti, V. and Cantelli, L., 1998. La tettonica delle Dolomiti nel quadro delle Alpi Meridionali orientali. Mem. Soc. Geol. It., 53: 133-143.
- Castellarin, A., Cantelli, L., Picotti, V., Selli, L., Fantoni, R., Nicolich, R., Dal Piaz, G.V., 2004. Structure of the Italian Dolomites, partially along the southern sector of the Transalp seismic profile, 32nd International Geological Congress. Guidebook Excursion, Firenze, 20-24 August 2004, pp. 54.

Castiglioni, B., Cornelious-Furlani, M., Vardabasso, S., 1930. C.G.I. F° 011- Carta Geologica delle Tre Venezie, Monte Marmolada, scala 1:100.000, Ufficio idrografico del R. magistrato alle Acque, Venezia. Studio Cartografico G. Giardi, Firenze.

Dogliani, C., 1984. Tettonica triassica transpressiva nelle Dolomiti. *Giornale di Geologia*, 3(46): 47-60.

Dogliani C., 1987. Tectonics of the Dolomites (Southern Alps, Northern Italy). *Journal of Structural Geology*, Vol. 9, No, 2. pp. 181-193.

Egli, M., Sartori, G., Mirabella, A., Giaccai, D., Favilli, F., Scherrer, D., Krebs, R., Delbos, E., 2010. The influence of weathering and organic matter on heavy metals lability in silicatic, Alpine soils. *Science of the Total Environment*, 408(4): 931-946.

Egli, M., Sartori, G., Mirabella, A. and Giaccai, D., 2010. The effects of exposure and climate on the weathering of late Pleistocene and Holocene Alpine soils. *Geomorphology*, 114(3): 466-482.

FAO (Food and Agriculture Organization of the United Nations), 1998. World Reference Base for Soil Resources. World Soil Resources Reports 84, FAO, Rome.

Gortani, M., 1912. Falde di detrito e coni di deiezione nella valle del Tagliamento. *Mem. Geogr.*, 20: 95.

IUSS Working Group WRB, 2006. World Reference Base for Soil Resources 2006, World

Soil Resources Reports No. 103 2nd edition. FAO (Food and Agriculture Organisation of the United Nations), Rome.

Leonardi P. et al., 1967. Le Dolomiti. Geologia dei monti tra Isarco e Piave. Rovereto: Manfrini Editore. 1019 pp.

Leonardi, P., Rossi, D., Somnavilla, E., Bosellini, A., Semenza, E., 1970. Carta Geologica Italiana F° 011- Marmolada, scala 1:100.000. Poligrafiche Bolis, Bergamo.

Masetti, D., Neri, C., 1980. L'Anisico della Val di Fassa (Dolomiti Occidentali): sedimentologia e paleogeografia. Ann. Univ. di Ferrara 9, Scienze Terra(7): 1-19.

Neri, C., Stefani, M., 1998. Sintesi cronostratigrafica e sequenziale dell'evoluzione permiana superiore e triassica delle Dolomiti. Mem. Soc. Geol. It., 53: 417-473.

Reisigl, H., Keller, R. , 1995. Guida al bosco di montagna. Alberi, arbusti e vegetazione del sottobosco. Zanichelli, Bologna.

Rovereto, G., 1924. Trattato di Geologia Morfologica (Geomorfologia), 1. Hoepli, Milano, 1-641 pp.

Stefani, M., Caputo, R., 1998. Synvolcanic carbonate production at scalloped platform margins: examples from the Middle Triassic Catinaccio Buildups (Dolomites, Italy). Mem. Soc. Geol. It., 54: 143-146.

Trombetta, G., Bottoli, S., 1998. Tettonica e stratigrafia medio-triassica nel gruppo Col

Rossi e Porta Vescovo (Dolomiti Occidentali). Mem. Soc. Geol. It., 53: 325-339.

Viel, G., 1979. Litostratigrafia ladinica: una revisione. Ricostruzione paleogeografica e paleostrutturale dell'area Dolomitica-Cadorina (Alpi Meridionali). Riv. It. Paleont. Strat., 85: 85-125, 297-352.

CHAPTER 2

The cattle grazing effect on the landscape: automatic land cover classification using high-resolution remote sensing data

2.1 Introduction

1

Remote sensing is aimed at map and monitor terrestrial, oceanic and atmospheric surfaces; it is therefore implicit that this subject covers a multidisciplinary field of studies. Its applications and techniques represent an important tool in environmental management, providing up-to-date detailed information about land condition and use. With remote sensed data it is possible to acquire information on hardly accessible areas, such as deserts and extreme mountainous environments; moreover the satellite sensors detect features at electromagnetic wavelengths, which are not visible to the human eye.

In the last decades the spectral and spatial resolution of satellite images has rapidly improved, widening the application of remote sensing techniques to more specific areas. Nowadays, commercial satellites provide images with 0.5 meters of spatial resolution in the panchromatic band, which in natural environments, such the alpine one, allows to identify a single animal

¹*M. C. Morandi, G. Onorevoli, G. Pasquariello* and E. Farabegoli.
Manuscript in preparation
CNR-ISSIA Bari, Italy.*

as big as a sheep.

Remote sensing data are commonly used to create land cover maps, in which the scene is automatically divided in themes or regions, characterized by a similar spectral signature. These regions gain an additional value if they also discriminate portions of the scene with specific geomechanical behavior. In this case, the land cover map becomes an useful tool for distributing the geomechanical parameters across the territory. In the study area indeed (Duron valley), a considerable portion of the terrain exhibits the scars of intense grazing activity; here the grass mantle is damaged and the shear strength contribution of the vegetation, in the slope stability, is lowered. This chapter aims therefore to detect the distribution of heavily grazed areas in an alpine environment, by means of Maximum Likelihood classification on high- resolution satellite images.

2.2 The cattle grazing effect on the landscape

Pasturelands with long evolutionary grazing systems have been the subject of many studies in different physiographic environments; their common goal is to investigate and monitor the effects of the pastoral activity on the landscape (Fisher et al., 2002; Cingolani et al., 2008; Parolo et al., 2011 and references therein).

Most of the recent works focus on the effects of intensive grazing on the vegetation structure (Acutis et al., 1989; Cingolani et al., 2003; Sebastià et al., 2008; Mayer et al., 2009; Bugalho et al., 2011) and the nutrient availability of the soil (Güsewell et al., 2005), but relatively less attention has been paid to the mechanical effect of grazing on the grass cover. Nevertheless, overgrazing in the alpine regions represents one of the most important erosion factor (Descroix et al., 2008) and pastoral activity has been documented since the Neolithic Age. Previous studies conducted in California and Mexico, revealed that soil erosion in grazed areas reaches 1.85 mm/year (Trimble and Mendel, 1995; Decroix et al., 2008). Cattle

trampling acts on the hillslope micromorphology, modifies the local hydrogeology and alters the geomechanical resistances of both the soil and the vegetation cover. Although soil compaction, caused by the hooves of heavy animals, increases the soil geomechanical resistances (Stephenson and Veigel, 1987; Krzic et al., 2006), it decreases the shear resistances of the turf mantle. Closely spaced terracettes made of treads and risers mark the hillslope morphology, increasing the overall surface roughness. These terracettes follow generally the contour lines and locally are connected by shorter angular paths, which traverse the near vertical risers (Fig. 2.1).



Figure 2.1: Lenticular shaped sods isolated by cattle trails.

Cattle grazing acts also on the hillslope hydrology: the effect of soil compaction exerted by the animal's hooves increases the overland flow and during heavy rainfalls, the compacted trails act indeed as drainage paths. The grazing effects that more closely influence the hillslope stability is the shear resistances degradation of the grass mantle. The erosive trails break the grass mantle continuity isolating, in extreme cases, single sods of elongated shape (Fig. 2.2). Along these paths, the dense and intricate root's network might be partially or completely sheared and the pseudo-cohesion of the turf's roots is therefore diminished. The spatial distribution of heavily grazed pasture and its effect on pasture biomass production

may be monitored with the aid of remotely sensed data; in humid environments, vegetation and soil indices (Normalized Difference Vegetation Index, Soil Adjusted Vegetation Index, Moving Standard Deviation Index) have been successfully used to monitor pasture degradation (Boschetti et al., 2007; Numata et al., 2007; Paudel and Andersen, 2010), whereas in arid rangelands, grazing intensity may be related to the distance from the watering points (Pickup et al., 1998; Harris and Asner, 2003; Kawamura et al., 2005; Blanco et al., 2008).



Figure 2.2: Terracettes almost parallel to the contour lines.

2.3 Grazing in the Duron valley

Since the past century the study area has been exploited as pasture land for the cows and horses summer grazing of the Fassa and Gardena valley. The cattle reside here only in the summer months (end of May until the end of September) because the remaining of the year the area becomes an inhospitable environment due to the low temperatures, the snow cover and the limited daylight illumination. The study area is divided into three pastures (Fig.2.3): lower, upper and eastern. The lower pastureland is grazed by only cows (30); in the upper and the eastern one the cows (40 and 20, respectively) are mixed with semi-feral horses: 13 in the upper zone and 5 in the eastern one. Only the eastern pasture, owned by a different shepherd, is further divided into 4 zones, and it is grazed on a rotational base every 14 days.

The shepherd undertook this interchange of the pastureland because he realized that the livestock trampling was causing severe damages to the grass cover. The steepest areas of the basin, located in the upper pasture (Col de l'Agnel) are excluded from grazing and fenced. The number of animals hasn't changed substantially in the past 5 years; the only exception occurred in the year 2011, when they introduced approximately 15 mountain goats in the eastern pasture.

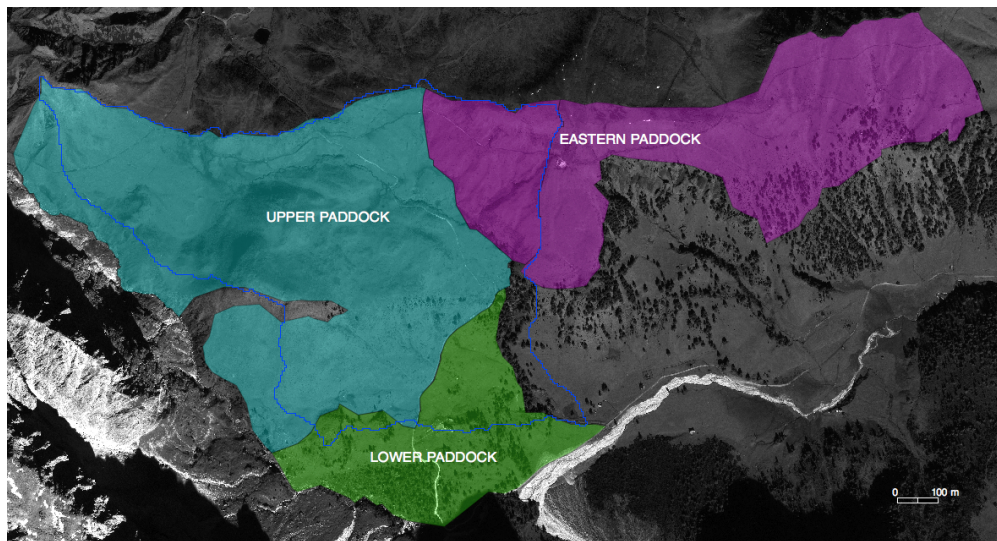


Figure 2.3: Pastures distribution in the study area.

2.4 Image processing

Once the image has been registered by the satellite's sensors, multiple computer algorithms must be used to create useful images from the raw data. These algorithms correct the images for the interferences caused by the atmosphere and align them to standard map grids (registration and orthorectification processes). Digital image processing represents the only practical technology to prepare images for further operations such as classification, feature extraction, pattern recognition and multi scale signal analysis. Among these operations, land cover and land use maps are produced taking advantage of the classification techniques.

2.4.1 Image classification

The objective of image classification is to produce thematic maps of the earth surface in which all pixels are automatically categorized into land cover classes or themes. Multispectral data are normally used for classification and indeed the spectral pattern present within the data for each pixel is used as the numerical basis for categorization (Lillesand et al., 2006). The classification algorithms utilize the pixel-by-pixel information to extract patterns, which can be based on the spectral information (as in the case of automated land cover classification) or on the spatial relationship between adjacent pixels. Image classifiers may also be used in a hybrid mode, combining the spatial and spectral pattern recognition (object-oriented classification). Traditional classification techniques are divided into two categories: unsupervised and supervised. In the unsupervised approach the image data are classified by aggregating them into the natural spectral groupings or clusters. This technique doesn't require a strict control of the ground truth, as the clusters are automatically generated by the algorithm. In a second step the image analyst determines the land cover identity of these spectral groups. In the supervised approach the image analyst "supervises" the classification process by defining a priori the classes in which he wants the images to be divided. These classes, called also training areas or region of interest, represent sample sites of known cover type. An additional classification procedure is the hybrid classification, which involves aspects of both the supervised and the unsupervised classification. For this work I used a supervised classification procedure: the maximum likelihood algorithm.

2.4.2 Maximum likelihood classification

The maximum likelihood classifier is one of the most popular methods of classification in remote sensing image analysis (Richards, 1999). The algorithm calculates the probability that a certain pixel x belongs to a class C_i given the *a priori* probability that is calculated

on the ground truth data (regions of interest). All the data points for each class are assumed to follow a unimodal distribution (Gaussian) and a Bayesian weight is applied to calculate the *a posteriori* probability.

The *a posteriori* probability can be written as:

$$P(C_i|x) = \frac{P(x|C_i)P(C_i)}{\sum_{k=1}^n (P(x|C_k)P(C_k))} \quad (2.1)$$

where

$P(C_i)$ represents the *a priori* probability of class C_i and

$P(x|C_i)$ is the conditional probability derived from the training data. In the case of a single dimension, the conditional probability that the data point x_i is observed for the given class C_i , can be written as:

$$P(x|C_i) = \left(\frac{1}{\sqrt{2\pi}\sigma}\right)e^{-\frac{1}{2}\left[\frac{x-\mu}{\sigma}\right]^2} \quad (2.2)$$

given

$$\mu = \frac{1}{p} \sum_{k=1}^p x_k \quad (\text{sample mean}) \quad (2.3)$$

$$\sigma^2 = \frac{1}{p} \sum_{k=1}^p (x_k - \mu)^2 \quad (\text{sample variance}) \quad (2.4)$$

where p is the number of pixels belonging to class C_i .

In the multivariate Gaussian distribution, the mean and the variance are replaced by the

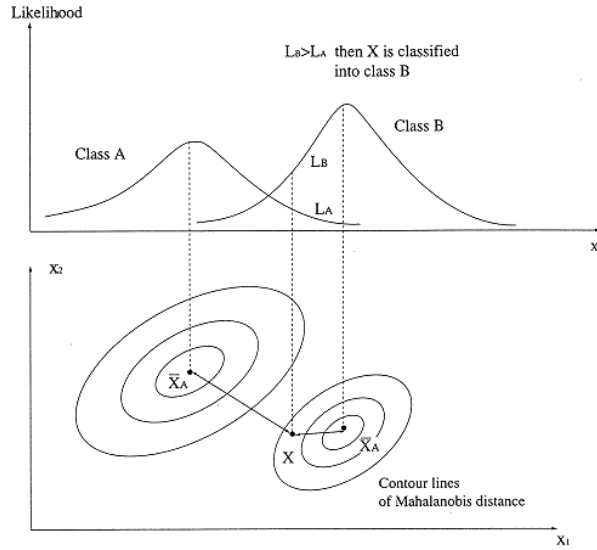
mean vector μ_k and the covariance matrix Σ_k and the probability is given by:

$$P(\vec{x}|C_i) = \left(\frac{1}{(2\pi)^{\frac{n}{2}} |\vec{\Sigma}|^{\frac{1}{2}}} \right) e^{-\frac{1}{2}(\vec{x}-\vec{\mu})^T \Sigma^{-1}(\vec{x}-\vec{\mu})} \quad (2.5)$$

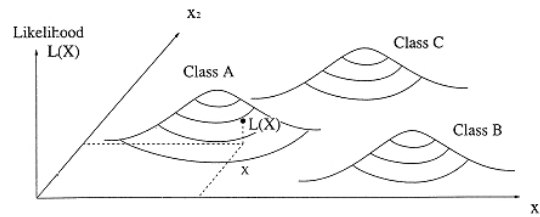
The probability values can be visualized in a three-dimensional graph, in which the vertical axis represents the probability of a pixel value being a member of one of the classes. The resulting bell-shaped surfaces are called Probability Density Functions (PDFs) and there is a function for each class. In fig.2.4 the PDF (b) of two selected bands (x_1 and x_2) are represented for the classes A, B and C; while in (a) are shown the ellipsoidal “equiprobability contours”.

2.5 Vegetation indices

Vegetation indices are simple and effective techniques to extract quantitative information on the amount of vegetation biomass, or greenness, for every pixel in an image (Chuvieco, 1998). The spectral bands typically involved are the red (0.6-0.7 μm) and the near infrared (0.7-1.1 μm), which represent respectively the best chlorophyll-absorbing region and the non-absorbing region, where there is significant leaf scattering. In the green region (0.52-0.6 μm) the soil-vegetation reflectance has a low contrast (chlorophyll is slightly absorptive), therefore it is not suitable for detecting biomass. Among the long list of vegetation indices, the most common are the Normalized Difference Vegetation Index (NDVI) and the Soil Adjusted Vegetation index (SAVI). The NDVI is expressed by the formula:



(a) Schematic Concept of Maximum Likelihood Classifier



(b) Likelihood Functions in 3D Expression

Figure 2.4: Schematic concept of Maximum likelihood classification.

$$NDVI = \frac{I - R}{I + R} \quad (2.6)$$

Where I is the radiance in the infrared band and R is the radiance in the red band (Tucker, 1979). Vegetated areas will generally yield high values of NDVI, whereas water, clouds, snow, rocks, bare soil and urbanized areas have values close to zero. The SAVI (Huete, 1988) is very similar to the NDVI formula, but it takes into account also the effect of soil brightness in the scene.

Grazed areas have a relatively low NDVI values than undamaged grass. Given the fact that the studied alpine terrain rarely experience dry conditions (soil water content $\ll 20\%$), where

the grass mantle is grazed, the greenness of the land cover is lower, because in between the terracettes the soil outcrops.

2.6 Land cover classification

Most of the land cover classification studies based on remote sensed data have been performed on Landsat (Cingolani et al., 2003; Keuchel et al., 2003) or Ikonos images (Giannetti and Grignetti, 2009), which assure a high spectral resolution but have a limited spatial resolution. Given the small size of the study area (0.76 km²) we needed very high spatial resolution images. At the time of writing this manuscript, the GeoEye-1 satellite provided the highest resolution and most advanced commercial imaging (Fig. 2.5). This satellite acquires simultaneously 0.5 m panchromatic and 2 m multispectral imagery. Satellite images collection and specification are give in table 2.1. All the images were preprocessed with radiometric correction and orthorectified using a 2 m cell size DTM (Digital Terrain Model).

| SATELLITE | | | |
|----------------------------|---------------------|----------------------|-----------------------|
| Swath Width | 15.2 km | Band | Wavelength(mm) |
| Off-Nadir imaging | Up to 60 degrees | Blue | 0.45 – 0.9 |
| = Dynamic range | 11bits per pixel | Green | 0.51 – 0.6 |
| Mission Life | Expected > 10 years | Red | 0.63 – 0.7 |
| Revisit Time | Less than 3 days | Near IR | 0.73 – 0.85 |
| Orbital Altitude | 681 km | | |
| Nodal Crossing | 10:30 AM | | |
| IMAGERY | | | |
| | Panchromatic | Multispectral | |
| Spatial resolution | 0.5 meter | 2 meters | |
| Positional accuracy | 5 m CE90 (specif.) | | |
| | 5 m CE90 (meas.) | | |
| Collection capacity | 350,000 sqkm/day | | |

Table 2.1: GeoEye imagery and satellite specifications.



Figure 2.5: GeoEye satellite image in the RGB bands.

2.6.1 Land cover classes

The study area is located on an alpine terrain; the soil is almost completely vegetated, made exception for two mountain stables and a short track of paved road, which is located on a very steep hairpin bend to facilitate the jeeps transit. These artificial features occupy altogether less than 1% of the total catchment area. Given the high resolution of the satellite images, we divided the area in 5 classes of land cover: bare soil, outcrops, trees and shadows, grazed grass and undamaged grass. The classes were chosen on the base of their geomechanical implications in slope stability.

Among these five classes we focused on the distribution of the grass cover classes (grazed and ungrazed) because we coupled this satellite image classification with geomechanical field data, collected on these types of grass cover. The grazed turf offers indeed lower shear resistances because the dense and intricate network of roots, which forms the turf, has been partially or totally sheared by the animal's hooves.

Ground truth data was collected on the catchment area and their sample data points and number of training areas are given in table 2.2. Trees and shadows were included in the same class because the separability between these two features was too low. This fusion doesn't lead to relevant misclassification errors, as the shadowed spots in the study area are mostly located in between the trees.

The outcrop class embodies both the carbonate rocks, which outcrop in the southern part of the valley just outside the catchment area, and the alluvial bed of the Duron creek. The separability analysis was performed measuring the Jeffrey-Matusita parameter: these values range from 0 to 2.0 and indicate how well the selected pairs are statistically separate (Richards, 1999). Generally, values greater than 1.7 indicate that pairs have adequate separability to be discriminated by classification algorithm. The separability report indicates that all the classes are quite separable, made exception for the tree/shadows and the grazed turf ones (Fig. 2.6); for this pair the Jeffrey-Matusita value is only 1.55. The grazed turf class comprehends indeed the narrow shadows, which form between adjacent terracettes; it is therefore expected that the spectral signature of these two classes might be partially overlapping.

| Class name | Data point | Number of training areas |
|-------------------|-------------------|---------------------------------|
| Trees/shadows | 23577 | 5 |
| Outcrops | 16458 | 5 |
| Bare soil | 473 | 8 |
| Grazed areas | 7190 | 6 |
| Undamaged grass | 10421 | 5 |

Table 2.2: Sizes and numbers of data points of the 5 classes.

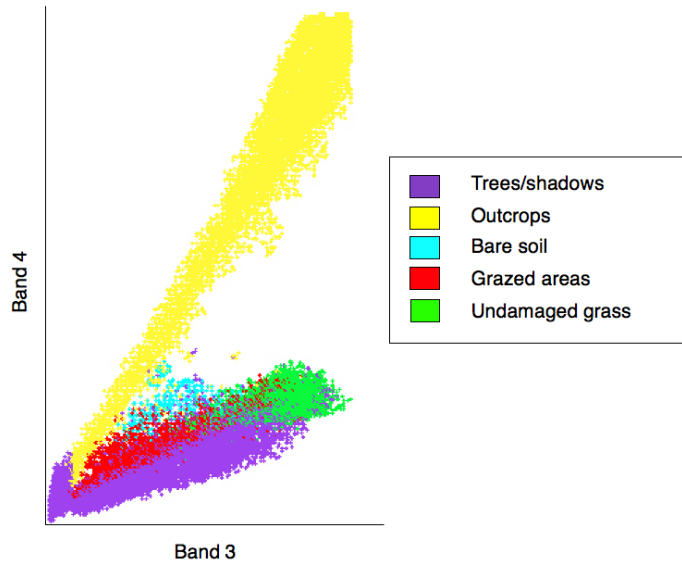


Figure 2.6: Projection of the training data on the Near Infra Red band (x -axis) and Green band (y -axis).

2.6.2 Maximum likelihood classification

The satellite images were classified using the maximum likelihood algorithm (Richards, 1999). This classification method assumes that the statistics in each band follow an unimodal Gaussian distribution and calculates the probability that a given pixel belongs to a specific class. Each pixel is assigned to the class that has the highest probability. For the classification process we tested different bands, and chose the ones that provided the best cross-validation accuracy. The maximum likelihood supervised classification was applied to a data set that comprehends the four multispectral bands (red, green, blue and near infrared), a texture co-occurrence measure (variance) and the NDVI map. The variance map was calculated on a 3x3 kernel of the panchromatic image, and later resampled to 2 m in order to match the resolution of the other images. Using this texture filter we were able to classify the grazed areas, which are characterized by a high values of variance, due to the micro-morphological disturb of the terracettes. The NDVI map (see paragraph 1.5) was calculated using the reflectance of the red and near infra red bands.

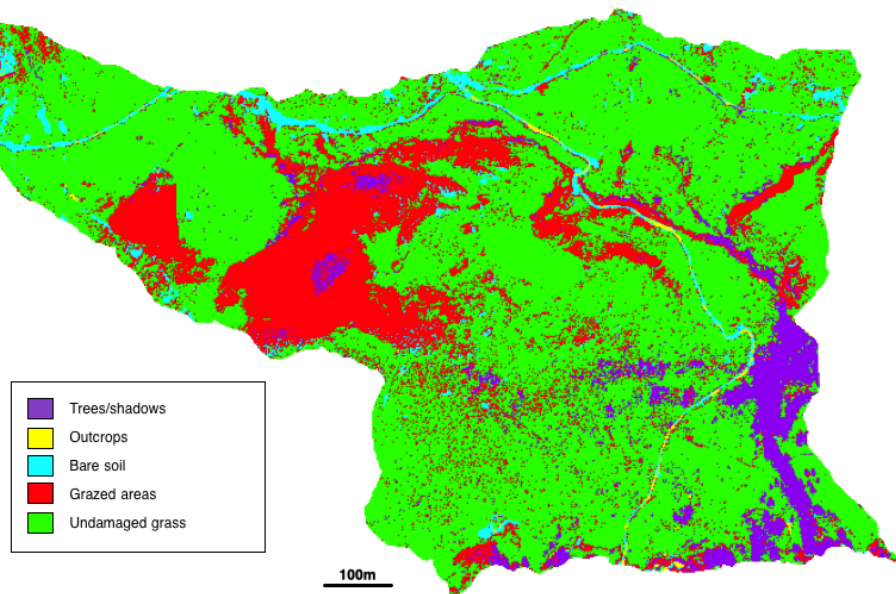


Figure 2.7: Classified map of the study area using the five classes on six bands (RGBNir, variance and NDVI).

2.7 Results and discussion

The classification performed using six bands, returned a highly reliable map of the distribution of the different cover classes in this mountainous area (Fig.2.7). The heavily grazed areas are located at the center of the catchment area, in correspondence of the upper paddock (Fig.2.3). Among the three pasture lands, the upper one has indeed the highest pastoral value. The use of the co-occurrence parameter (variance) and the NDVI maps, proved to be fundamental in classifying the grazed area. From this classification we derived that the total catchment area, which suffers from intensive grazing is 20%. The accuracy of the classification was assessed using the confusion matrix (Foody, 2002), which defines the number of correctly classified pixel in each class, on the base of the ground truth data (Table 2.3); the overall cross-validation accuracy using this method resulted 92.17%, with all the pixels classified in the five classes.

| Class | Ungrazed | Bare | Grazed | Trees/shadows | Outcrops |
|---------------|----------|------|--------|---------------|----------|
| Unclassified | 0 | 0 | 0 | 0 | 0 |
| Ungrazed | 9808 | 20 | 825 | 533 | 1 |
| Bare soil | 53 | 448 | 206 | 98 | 67 |
| Grazed | 499 | 3 | 5803 | 1448 | 28 |
| Trees/shadows | 61 | 0 | 346 | 21415 | 266 |
| Outcrops | 0 | 2 | 10 | 83 | 16096 |
| Total | 10421 | 473 | 7190 | 23577 | 16458 |

Table 2.3: Confusion matrix.

2.8 Conclusions

The goal of this chapter was to detect the distribution of heavily grazed areas in an alpine environment, by means of Maximum Likelihood classification. The satellite images used for this study have very high spatial resolution (2 m in the multispectral bands and 0.5 m in the panchromatic one); this allowed us to perform a very detailed classification of the study area, using five land cover classes. The number of the classes was dictated by their "quality" (spectral separability) and their geotechnical implications. Each of these land units contributes indeed with different weights to the land cover shear resistances.

During the error-and-trial process of selecting the best bands for classification, the variance and the NDVI resulted the most appropriate, increasing the overall accuracy to 92.17% (Table 2.3).

Using these two bands, on top of the four multispectral ones (R, G, B, Nir), the grazing effect of cattle on the hillslopes can be successfully mapped.

References

- Acutis, M., Pascal, G., Reyneri, A., Siniscalco, C., 1989. Evolution of Vegetation Under Intensive Grazing: Two Examples in North-western Italian Mountains. *Agriculture Ecosystems & Environment*, 27: 347-359.
- Blanco, L.J., Aguilera, M.O., Paruelo, J.M., Biurrun, F.N., 2008. Grazing effect on NDVI across an aridity gradient in Argentina. *Journal of Arid Environments*, 72: 764-776.
- Boschetti, M., Bocchi, S., Brivio, A., 2007. Assessment of pasture production in the Italian Alps using spectrometric and remote sensing information. *Agriculture Ecosystems & Environment*, 118: 267-272.
- Bugalho, M., Lecomte, X., Goncalves, M., Caldeira, M.C., Branco, M., 2011. Establishing grazing and grazing-excluded patches increases plant and invertebrate diversity in a Mediterranean oak woodland. *Forest Ecology and Management*, 261: 2133-2139.
- Chuvieco, E. and Huete, A., 2009. *Fundamentals of satellite remote sensing*. CRC Press.
- Cingolani, A.M., Cabido, M.R., Renison, D. and Solis, V.N., 2003. Combined effects of environment and grazing on vegetation structure in Argentine granite grasslands. *Journal of Vegetation Science*, 14(2): 223-232.
- Cingolani, A.M., Renison, D., Tecco, P.A., Gurvich, D.E. and Cabido, M., 2008. Predicting cover types in a mountain range with long evolutionary grazing history: a GIS approach. *Journal of Biogeography*, 35(3): 538-551.

Compton J, T., 1979. Red and photographic infrared linear combinations for monitoring vegetation. *Remote Sensing of Environment*, 8(2): 127-150.

Descroix, L., Barrios, J.L.G., Viramontes, D., Poulenard, J., Anaya, E., Esteves, M., and Estrada, J., 2008. Gully and sheet erosion on subtropical mountain slopes: their respective roles and the scale effect. *Catena*, 72(3): 325-339.

Fischer, M. and Wipf, S., 2002. Effect of low-intensity grazing on the species-rich vegetation of traditionally mown subalpine meadows. *Biological Conservation*, 104(1): 1-11.

Foody, G.M., 2002. Status of land cover classification accuracy assessment. *Remote Sensing of Environment*, 80(1): 185-201.

Giannetti, F. and Grignetti, A., 2009. Analysis of forest health at landscape level through very high resolution satellite images. *Remote sensing for a changing Europe. Proceedings of the 28th Symposium of the European Association of Remote Sensing Laboratories, Istanbul, Turkey, 2-5 June 2008 2009 pp. 270-275.*

Gusewell, S., Jewell, P.L. and Edwards, P.J., 2005. Effects of heterogeneous habitat use by cattle on nutrient availability and litter decomposition in soils of an Alpine pasture. *Plant and Soil*, 268(1-2): 135-149.

Harris, A.T. and Asner, G.P., 2003. Grazing gradient detection with airborne imaging spectroscopy on a semi-arid rangeland. *Journal of Arid Environments*, 55(3): 391-404.

- Huete, A.R., 1988. A soil-adjusted vegetation index (SAVI). *Remote Sens. Env.* 25, 295–309.
- Kawamura, K., Akiyama, T., Yokota, H., Tsutsumi, M., Yasuda, T., Watanabe, O., Wang, O., 2005. Quantifying grazing intensities using geographic information systems and satellite remote sensing in the Xilingol steppe region, Inner Mongolia, China. *Agriculture Ecosystems & Environment*, 107: 83-93.
- Keuchel, J., Naumann, S., Heiler, M. and Siegmund, A., 2003. Automatic land cover analysis for Tenerife by supervised classification using remotely sensed data. *Remote Sensing of Environment*, 86(4): 530-541.
- Krzic, M., Newman, R.F., Trethewey, C., Bulmer, C.E. and Chapman, B.K., 2006. Cattle grazing effects on plant species composition and soil compaction on rehabilitated forest landings in central interior British Columbia. *Journal of Soil and Water Conservation*, 61(3): 137-144.
- Lillesand, T.M., Kiefer, R.W., and Chipman, J.W., 2007. *Remote Sensing and Image Interpretation*. John Wiley & Sons, Inc. Sixth Ed.
- Mayer, R., Kaufmann, R., Vorhauser, K., Erschbamer, B., 2009. Effects of grazing exclusion on species composition in high-altitude grasslands of the Central Alps. *Basic and Applied Ecology*, 10: 447-445.
- Numata, I., Roberts, D.A., Chadwick, O.A., Schimel, J., Sampaio, F.R., Leonidas, F.C., Soares, J., 2007. Characterization of pasture biophysical properties and the impact of grazing intensity using remotely sensed data. *Remote Sensing of Environment*, 109: 314-327.

- Parolo, G., Abeli, T., Gusmeroli, F. and Rossi, G., 2011. Large-scale heterogeneous cattle grazing affects plant diversity and forage value of Alpine species-rich *Nardus* pastures. *Grass and Forage Science*, 66(4): 541-550.
- Pickup, G., Bastin, G.N. and Chewings, V.H., 1998. Identifying trends in land degradation in non-equilibrium rangelands. *Journal of Applied Ecology*, 35(3): 365-377.
- Prasad Paudel, K., Andersen, P., 2010. Assessing rangeland degradation using multi temporal satellite images and grazing pressure surface model in Upper Mustang, Trans Himalaya, Nepal. *Remote Sensing of Environment*, 114: 1845-1855.
- Richards, J.A., 1999. *Remote Sensing Digital Images Analysis*, Springer-Verlag, Berlin, p.340.
- Sebastia, M.T., de Bello, F., Puig, L. and Taull, M., 2008. Grazing as a factor structuring grasslands in the Pyrenees. *Applied Vegetation Science*, 11(2): 215-223.
- Stephenson, G.R. and Veigel, A., 1987. Recovery of compacted soil on pastures used for winter cattle feeding. *Journal of Range Management*, 40(1): 46-49.
- Trimble, S.W. and Mendel, A.C., 1995. The cow as a geomorphic agent - A critical review *Geomorphology*, 13(1-4): 233-253.
- Tucker, C.J., 1979. Red and photographic infrared linear combinations for monitoring vegetation. *Remote Sensing of Environment*, 8(2): 127-150.

CHAPTER 3

Geomechanical and hydrological soil properties of the Duron valley

3.1 Introduction

¹ In order to retrieve the geomechanical properties of soil and sub-soil, we combined traditional techniques with innovative methods. Grain sizes, bulk properties and friction angles were retrieved through standard laboratory analyses, while the soil depth was measured using Ground Penetrating Radar surveys. We also performed an extensive field test campaign to measure the shear strength of the soil, using a field Torvane scissometer. The collected data were used both as input in shallow landsliding susceptibility models and to test the reliability of the shear resistances measured with the Turf's comb instrument (described in the following chapter).

Field and laboratory data confirmed the excellent geomechanical properties of the soil&root system (peak shear strength measured with the Vane scissometer reached 85 kPa) and the sandy nature of the soils (high permeability and friction angles).

¹ *This chapter constitutes part of the article by E. Farabegoli, M. C. Morandi, G. Onorevoli and D. Tonidandel: "Geotechnical properties and root reinforcement of soil in a grass mantled Alpine test catchment (Duron valley, Dolomites, Italy)." Submitted to Geomorphology, Elsevier.*

3.2 Soil depth

Measure the soil thickness is a time-consuming task, which is difficult to perform in large and/or very steep mountainous areas. The use of indirect methods, such as geophysical techniques, to investigate the subsurface structures, has gained increasing attention in geological and geomorphological studies (Mellett, 1995; Van Dam, 2012). Ground Penetrating Radar surveys represent indeed an effective tool for soil depth investigation in terrains which have a low clay and silt content. Schrott and Sass (2008) suggest that geophysical data should be coupled with geomorphological/geological data, in order to produce a reliable interpretation of the subsurface architecture. Here, given the limited size of the study area, and limiting the uncertainty of the data, we used direct and indirect methods to systematically collect soil-thickness measurements. Soil thickness was investigated driving a 105 cm long, 1.4 cm diameter steel rod into the ground until refusal. Although this method is time consuming and laborious, it provides a direct, simple and inexpensive measurements of the soil depth (Tesfa et al., 2009). Indirect measurements of soil depth were recorded with GPR (Ground Penetrating Radar) surveys. With the 500 MHz antenna we covered a 9 km track throughout the catchment basin while 3 km were covered using the 250 MHz antenna (Fig.3.1). The GPR profiles have been filtered and the data were calibrated using 265 direct soil depth measurements. In the GPR profiles, the interface soil-bedrock is recognizable by the change in sharpness of the reflectors; the GPR track was sampled at constant intervals (15 m) and the depth of the soil was entered in the map as a 3D locus (geographic coordinates and the soil depth).

From the soil depth model based on GPR data (Fig. 3.3) we attained that soil thickness is on average 50 cm; it reaches the highest values (ca. 2 m) on the northern part of the basin, at the hollow axes. Areas of moderate slope have thick soil, whereas areas of no soil often correspond to outcrops or shallow landslide scars.

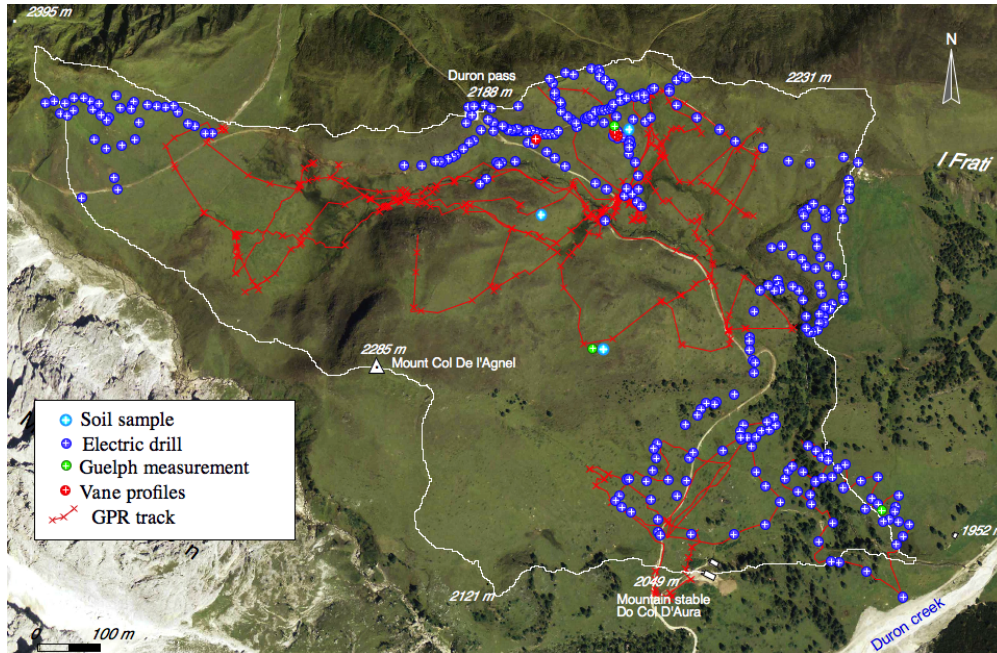


Figure 3.1: GPR traces and location of the Vane and Guelph permeameter measurements

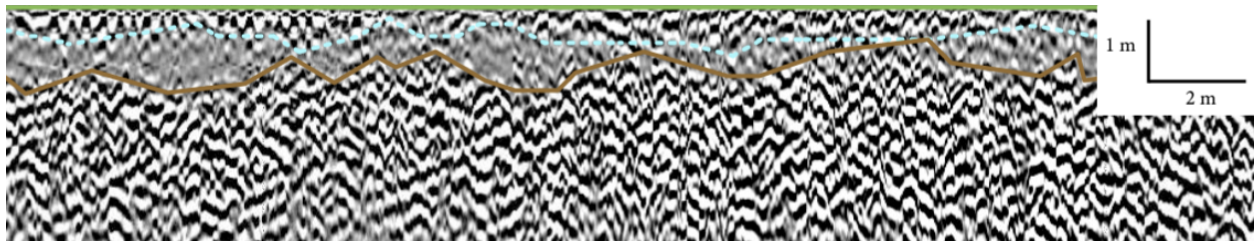


Figure 3.2: GPR profile interpretation: the green line is the soil-air interface, the brown line is the bedrock-soil contact and the dashed blue line represents the upper boundary of the water table. The reflectors lose their sharpness where the investigated medium has a high water content.

3.3 Laboratory analyses

We performed laboratory analyses on 5 soil samples (partially published in Morandi, 2009), including grain sizes distribution, bulk composition, Atterberg's limits, organic content and Consolidated Drained direct shear stress (Table 3.1). Two samples (MN2 and MN2-1) were

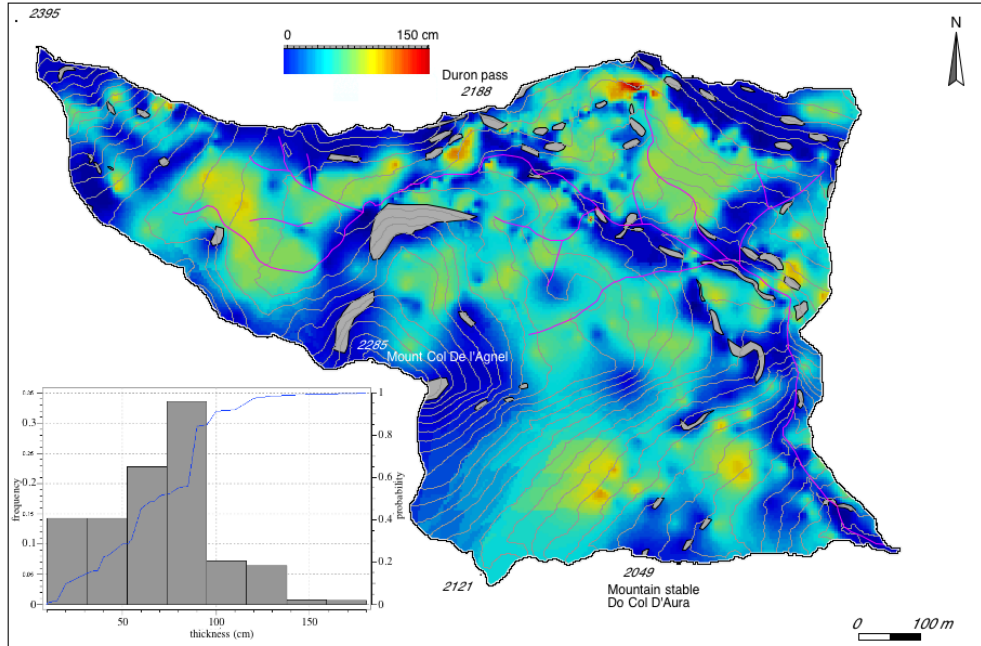


Figure 3.3: Soil depth distribution derived from GPR surveys and electric drill measurements. All the data were interpolated using the ordinary kriging method.

collected on a gently sloped (approx. 13°) and south-facing side of the Col de l'Agnel mound; here soil depth doesn't exceed 50-60 cm and the bedrock consists in pillow breccias. Samples PD1 and PD2 were collected in the northern part of the catchment area, at the hollow axis: here soil is thick (up to 2m) and consists in stacked, channelized debris flow and traction current deposits. Bedrock consists of volcanic micro-breccias and volcanic sandstones. The last sample, RC was collected near the toe of a small alluvial fan in the northwestern part of the basin.

According to the A.S.T.M. classification, all samples belong to the silty-sand class and have high organic content, particularly in those samples close to the surface (MN2, MN2-1 and PD1). Average bulk density is 1.11 g/cm^3 , increasing, with depth from 0.86 to 1.36 g/cm^3 . Effective friction angle and effective cohesion were measured in laboratory, using a Casagrande shear box (Consolidated Drained direct shear tests). The soil samples were sieved (20 mesh) and pre-consolidated at three different rates: 25, 50 and 100 kPa. Friction

| Sample | Depth (cm) | Bulk density (g/cm ³) | Liquid limit | Organic content (%) | Friction angle (o) | Cohesion (kPa) |
|--------|------------|-----------------------------------|--------------|---------------------|--------------------|----------------|
| MN2 | 0 | 0.86 | 108.98 | 37.46 | 30.11 | 7.19 |
| MN2-1 | 30 | 1.29 | 117.47 | 21.43 | 28.65 | 11.74 |
| PD1 | 20-30 | 1.13 | 111.44 | 20.46 | 28 | 10.72 |
| PD2 | 50-60 | 1.36 | 46.43 | 9.66 | 34.24 | 7.77 |
| RC | 30-40 | 0.82 | 97.85 | 4.6 | 27.2 | 8.2 |

Table 3.1: Laboratory analyses results.

angle values (27°- 34°, Table 3.1) are typical of sandy soils while the effective cohesion resulted high (7-11 kPa. 3.1). This last result is probably caused by some limitations of the testing procedure. During the measure, it is not possible to monitor or control the drainage condition of the shear box apparatus, moreover, the sample preparation and the imposed pre-consolidation loads, influence the results of the test; it is well known that with this test, the effective cohesion is generally overestimated (Lancellotta, 1987).

3.4 Vane measurements

The undrained shear resistances of the saturated soil were also measured in the field using a Field Vane scissometer (Fig. 3.5). The test consists in forcing the scissometer, equipped with two orthogonal blades, into the soil and then rotating the instrument until the soil fails. This produces a cylindrical shear surface on the soil: the maximum torque registered is related to the undrained shear strength of the material. The operator records the maximum torque value and, after several turns, the remolded strength of the soil.

In 83 locations we measured the shear resistances of the soil at the depths of 12.5, 20 and 30 cm, while in further 15 locations we applied an extension rod to the instrument (100 cm long) and measured the resistances down to 78 cm of depth (Table 3.2). The Vane tests were coupled with soil water content measurements collected by a Water Content Reflectometer, at the depth of 30 cm. Soil moisture content during the summer varies from 26% to 50%.

The highest shear resistances in the upper part of the soil profile (30 cm) are located close to the surface (12.5 cm), where the turf's roots exert their influence and the soil is compacted by previous overburden loads (pastoral activity) (Fig. 3.4). Field observations revealed that the intricate and dense root network of the grass penetrates only into the first 15-20 cm of soil. The shear resistances decrease until 30 cm and increase slightly downward by effect of soil compaction. At several locations the Vane measurements were out of the instrument scale indicating that during the torsion, the blades encountered a pebble; we decided to neglect these measurements. Maximum shear strength values were recorded at the depth of 80 cm (85 kPa), while in the first 20 cm of soil the average strength is 65 kPa.

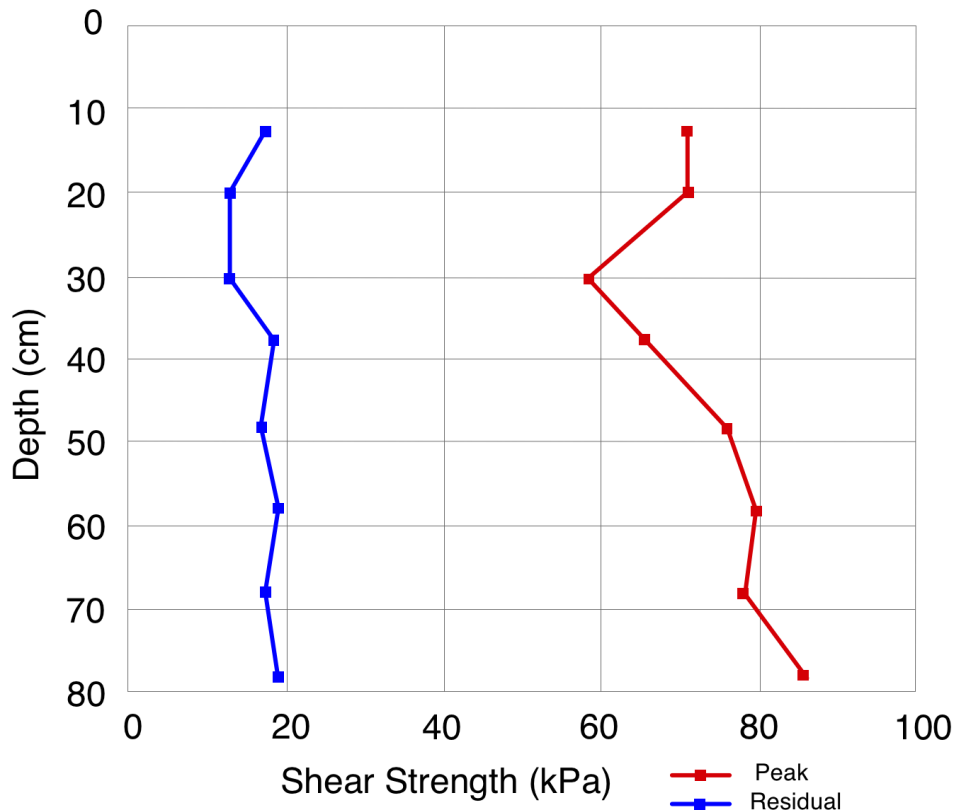


Figure 3.4: Soil strength profile measured with the Vane Scissometer (each symbol represents the mean of all data measured at the specific soil depth). Both peak (red) and residual (blue) values are plotted.

| Depth (cm) | Type | Mean(kPa) | Samples |
|------------|----------|-----------|---------|
| 12.5 | Peak | 70.96 | 83 |
| | Residual | 17.59 | 83 |
| 20 | Peak | 62.54 | 82 |
| | Residual | 13.33 | 83 |
| 30 | Peak | 58.12 | 71 |
| | Residual | 13.09 | 75 |
| 38 | Peak | 65.59 | 15 |
| | Residual | 18.07 | 15 |
| 48 | Peak | 76.51 | 15 |
| | Residual | 16.85 | 15 |
| 58 | Peak | 79.88 | 14 |
| | Residual | 18.99 | 14 |
| 68 | Peak | 78.11 | 12 |
| | Residual | 17.02 | 12 |
| 78 | Peak | 85.74 | 10 |
| | Residual | 18.54 | 9 |

Table 3.2: Field Vane measurements

3.4.1 Water content and Guelph permeameter

Soil water content measurements were conducted using a Water Content Reflectometer (CS616, Campbell Scientific INC), which measures the volumetric water content of a porous media (such as soil) using the time-domain measurement method. This method consists of the CS616 generating an electromagnetic pulse; the elapsed travel time and pulse reflection are then measured and used to calculate soil volumetric water content.

Several measurements were taken along the vane transects: in the summer, the soil water content varies from 26% to 50%. For this measurement, mean values are meaningless because the soil water content was measured at different time of the year and in different topographic positions (ridges and hollows).

The soil hydraulic field saturated conductivity (k_s) was measured using a Guelph permeameter (Reynolds and Elrick, 1985) at five locations (Fig. 3.1). This instrument measures the steady-state rate of water recharge into unsaturated soil from a 0.8 cm cylindrical hole, in

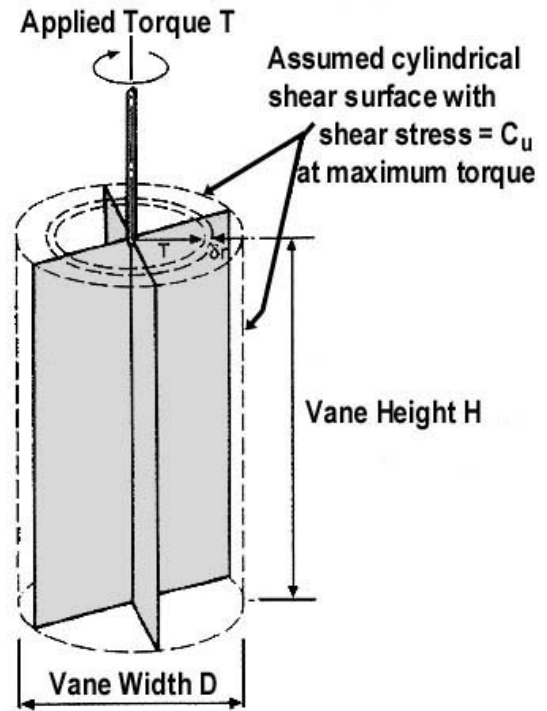


Figure 3.5: The Vane scissometer: the instrument and schematic drawing that shows the operation mode.

which a constant head of water is maintained (Fig. 3.6). The average hydraulic conductivity for the soil in the five test locations of the Duron valley resulted $4.1 \times 10^{-6} \text{m/s}$.

3.5 Results and discussion

The investigation methods here proposed to retrieve the geomechanical properties of soils and sub-soils, combine both innovative techniques and traditional ones. The use of GPR data



Figure 3.6: The Guelph permeameter.

to collect soil depth measures proved to be a simple methodology which couples efficiently an inexpensive testing procedures (the cost of the GPR instrument) with a large empirical data base. The resulting soil depth map (Fig. 3.3) indicates quite clearly which portions of the catchment have a thicker soil. Combining this information with the distribution of the slopes across the basin, it is possible to isolate the areas where soil thickness is not directly linked to the slope gradient. Generally, the distribution of soil thickness is inversely proportional to the slope, nevertheless, in this study area, the north-central part of the catchment, where all the hollows are located, have thick soil (up to 2 m) and a relatively high slope angle (approx.

30°). The real distribution of soil thickness embodies the effects of physical processes, which are not uniquely driven by gravity. The influence of glacial action and hydrological processes acting on the slopes, determined areas of accumulation and erosion, which are not directly linked with the topographic gradients. The relationship between slope and soil depth will be further analyzed in Chapter V, because the distribution of soil depth influences the slope stability analysis.

The geomechanical behavior of the soils was investigated using a field Vane scissometer. This instrument measures the *in situ* undrained shear strength of the soil, which is related to the torque applied on a cylindrical shear surface. The measured parameter combines the effect of the soil cohesion, soil matric suction and roots pseudo-cohesion (when roots are present). Although this test has been designed for cohesive soils, for the aim of this study we consider the Vane measurements to be reliable and to represent closely the undrained shear parameters of the studied porous media. In all the samples indeed the fine particles represent on average 38% of the grain sizes.

The advantages of using this technique are the simplicity of the test and the low cost and impact of the testing procedure. The instrument itself is light and can be easily carried in a small backpack. Nevertheless, in the past decades, the interpretation of the results has been the focus of many discussions. The critical issues of this type of measure are mainly related to the stress distribution on the failure surfaces, to the influence of time on the results (delay between the insertion and rotation of the blades) and to the excess of pore pressure originated by the insertion of the blades (Whittle et al., 1990). While the first two sources of errors can be fixed by introducing correcting coefficients, the last issue hasn't been addressed yet. Generally, the disturbance introduced by these factors doesn't exceed the 10% of the measured value (Perez-Foguet et al., 1999). The profiles (Fig. 3.4) indicate that the shear resistances are strong at the surface (70 kPa), decline rapidly down to 30 cm (58 kPa) and increase downward until the bottom of the profiles (80 cm, 85 kPa).

The strong resistances in the topsoil are related to the presence of thin grass roots, which add a remarkable contribution to the parameter measured by the Vane (see chapter IV) and to the compaction caused by pastoral use. The combined effect of these two factors is more effective in the upper most part of the soil, where the first measures were recorded (12.5 cm of depth). Downward the soil strength increases, as a function of increasing soil compaction: in this study area we haven't surveyed any grass roots below 30 cm. No test were performed in the first 10 cm of soil: we believe that the shear resistances of that portion of soil profile are ever higher, because the root system is denser (it reaches its maximum at 10 cm of depth) and soil compaction by animal grazing is stronger. A recent study, based on Vane measurements on soil with different grazing history (Bachmann et al., 2006) shows a similar shear strengths distribution with depth, but have generally higher values. These discrepancies can be explained by the different characteristics of the soil where the tests were carried out.

3.6 Conclusions

All the techniques adopted to measure the geomechanical and hydrogeological characteristics of the Duron valley soils, revealed that both soil and subsoil have excellent geomechanical parameters (shear strength and cohesion). Shear strength data, collected with the hand-driven instrument (Vane) were used to delineate the trend of resistances with depth. Nevertheless the standard deviation of these data is high (mainly driven by the high heterogeneity of these soils), the profiles show a similar trend: the resistances decrease from the topsoil to approx. 30 cm of depth and increase downward until the end of the profiles (80 cm).

The presence of grass roots in the upper most part of the soil profile exerts a strong influence on the bulk density of the near-surface sample and in the shear strength values. This strengthening effect has to be added to the high compaction state of the topsoil, due to the

intense grazing activity.

3.7 References

Bachmann, J., Contreras, K., Hartge, K.H. and MacDonald, R., 2006. Comparison of soil strength data obtained in situ with penetrometer and with vane shear test. *Soil & Tillage Research*, 87(1): 112-118.

Lancellotta, R., 1987. *Geotecnica*. Zanichelli Editore.

Mellett, J.S., 1995. Ground penetrating radar applications in engineering, environmental management, and geology. *Journal of Applied Geophysics*, 33(1-3): 157-166.

Morandi, M.C., 2009: “Caratterizzazione geologica-geotecnica del suolo e soprassuolo in alta val di Fassa (TN)”. Estratto della tesi di laurea specialistica in Geoscienze Applicate per il premio “ Gianfranco Bruzzi”. *Rivista dell’ordine dei Geologi dell’Emilia-Romagna* n 36, pp 29-37.

Perez-Foguet, A., Ledesma, A. and Huerta, A., 1999. Analysis of the vane test considering size and time effects. *International Journal for Numerical and Analytical Methods in Geomechanics*, 23(5): 383-412.

Reynolds, W.D., and Elrick, D.E., 1985. In situ measurement of field-saturated hydraulic conductivity, sorptivity and the alpha-parameter using the Guelph permeameter. *Soil science* 140(4): 292-302.

Schrott, L. and Sass, O., 2008. Application of field geophysics in geomorphology: Advances and limitations exemplified by case studies. *Geomorphology*, 93(1-2): 55-73.

Tesfa, T.K., Tarboton, D.G., Chandler, D.G. and McNamara, J.P., 2009. Modeling soil depth from topographic and land cover attributes. *Water Resources Research*, 45: 16.

Van Dam, R.M., 2012. Landform characterization using geophysics—Recent advances, applications, and emerging tools. *Geomorphology*, 137(1): 57-73.

Whittle, A.J., Aubeny C.P, Rafalovich A., Ladd C.C. and Baligh M.M., 1990. Interpretation of in-situ testing of cohesive soils using rational methods. Annual Technical Report, Constructed Facilities Division, Department of Civil Engineering, Massachusetts Institute of Technology, Boston USA.

CHAPTER 4

The “Turf’s comb”, a new *in situ* device to measure the shear resistance of the grass mantle: preliminary results and applications

4.1 Abstract

¹ The turf’s comb is a field device, which measures *in situ* the shear resistances of the grass mantle. It consists of a 20x20x0.8 cm metal plate holding several steel nails 10 cm long, connected to a calibrated electrical engine, which is controlled by an electronic control unit. At the test location, the plate with nails is nailed into the soil while the electrical engine, is allocated into a pre-excavated trench. After the soil volume between the comb and engine is removed, to allow the displacement of the soil-vegetation block, the engine exerts a pulling force, dragging the soil-vegetation block into the trench. During the experiment, a calibrated electronic control unit records the instant energy expenditure of the engine.

Turf’s comb allows to measure the shear strength applied on one or more of the facets of the soil-vegetation block, defining seven possible configurations of the experiments: a) over a single facet; b) over all of the 4 buried facets; and c) over different combinations of facets. The maximum available surface to measure the shear strength amounts to 1000 cm².

¹E. Farabegoli, G. Onorevoli and M.C. Morandi.
Submitted to Soil and Tillage Research, Elsevier

We present the preliminary results obtained in the experimental alpine site of the Duron valley (Dolomites, Italy), which document: 1) Turf's comb's ability to collect in the field the shear strength of the soil-grass complex, otherwise difficult to obtain with the currently available devices; 2) the peak shear strength mobilized along the facets of the soil-vegetation block is about 3000 N (30 kPa) where the grass mantle is undamaged; 3) in grazed areas, the shear strength of the grass mantle is reduced to 2000 N (20 kPa); 4) when the soil mantle is completely saturated the shear strength reaches low values 1700 N (17 kPa) ; 5) the shear resistance mobilized on the bottom side is very low.

The major contribution is supplied by lateral facets, and to a lesser extent by the backward facet. Moreover the time to mobilize the peak shear strength of different facets can differ significantly. Such data variability allows to draw hypotheses on the effects of local roots architecture, the integrity of the grass mantle, and water content on the overall shear strength of the soil-vegetation complex. The optimal shear strength properties of intact grass fields (*Nardetum*) are certainly the effect of natural selection operated over thousands of years by the severe climatic conditions acting in the alpine area. Grazing and/or water saturation of the soil mantle lead to a significant decrease of undrained shear strength properties of surface soil, favoring shallow soil slips.

4.2 Introduction

It is a widely accepted concept that vegetation cover, with its network of roots, plays a fundamental role in the stability of hillslopes (Bishop and Stevens, 1964; Schiechl 1991; Wu and Watson 1998; Schmidt et al. 2001; Casadei et al. 2003; Roering et al. 2003; Schmidt et al. 2001, Sakals and Sidle 2004; Bischetti 2009; Norris, 2005; Normaniza and Barakban 2006; Pollen 2007; Marston 2010). Vegetation reduces water infiltration and provides a significant contribution to the shear strength through the pseudo-cohesion of roots (Waldron 1977;

Waldron and Dakessian 1981; Greenway 1987). Attempts to quantify the root contribution to shear strength in forest-covered hillslopes have been carried out through specific experiments in the field (Endo and Tsuruta, 1969; Wu et al. 1979; Wu et al. 1988) and the laboratory (e.g. Waldron 1977; Waldron and Dakessian 1981). The Wu (1979) and Waldron (1977) model (W&W Model), is the most common, simple and efficient scheme adopted to estimate root behavior and root reinforcement along the soil profile during shearing (Bischetti et al. 2009). Moreover, due to a strong space variability of root density and size (Schmidt et al. 2003), the results are valid only for the specific test-sites. Roering et al. (2003) overcame these limitations, demonstrating that root strength can be predicted by mapping the distribution and characteristics of trees on potentially unstable slopes.

The shear strength mobilized by various shrub roots have been measured in the field and validated by back analysis (Tosi, 2007) but much less data are available for grass-covered soil mantle (cf. Lawrence et al. 1996). Comino and Druetta (2010) studied crops under controlled seeding in the Italian Alpine environment, but there is very little data for grass mantled hillslopes in natural conditions.

We run several experiments, located in the study area according to soil thickness, relative position within the hillslope (e.g. landslide toe), integrity of the grass mantle (undisturbed vs deteriorated by grazing), and soil water content. In this paper we present the preliminary results on the shear strength provided by the grass mantle, collected in a sample area in the Duron valley (Central Dolomites, Italy) using the Turf's comb device.

4.3 Materials and methods

The turf's comb device consists of 10 main components (Fig. 4.1):

- 1) A 20x20x0.8 cm steel plate, holding 89 steel nails (diameter 0.5 cm) evenly spaced along every row. Even and odd rows are staggered in order to cover optimally the entire soil-

vegetation block. The nails used in the tests presented here extend for 11 cm from the lower surface of the plate;

2) A 16 mm diameter steel hinge screwed at the center of the plate, extending 8 cm from the lower surface of the plate;

3) An electronic controlled brushless linear actuator, using Exlar's patented, inverted roller screw mechanism to transform the rotational motion to the translational movement (75 mm) required by the plate. The strength range of the device extends up to 3000 N;

4) A 12 mm diameter rod, 20 cm long, connecting the central hinge to the translational axis of the engine. The connection with the plate hinge is jointed (to facilitate the plate-engine alignment), whereas the other end of the rod is screwed to one end of the translational axis;

5) An L-shaped steel plate, fixed by means of 4 screws penetrating at least 20 cm below the clean ground surface. The engine is laid above the L-shape plate, and tightened firmly with screws;

6) Three hard wood stakes, driven into the soil for at least 30 cm, to contrast the horizontal motion of the complex formed by the electrical engine and the L-shaped plate. Two stakes are in front of the L-shaped plate, the third being located 20 cm behind the plate, and connected to it with a steel tie cable. In some cases it was necessary to improve the overall contrast to the motion of the engine-shape complex by adding a fourth stake behind the third, connected to the latter with a second steel tie cable;

7) Three TDR sensors (CS616 - Campbell Scientific) and a thermocouple to measure soil water content and temperature;

8) A control unit to monitor the status of the engine and record the main activity parameters (voltage, expenditure, displacement, velocity, etc);

9) Two Lithium-Polymer batteries (22.2 V and 5.35 Ah), either interchangeable or connectable to each other in parallel, which guarantee the electrical supply for at least a full day of measurements;

10) The cables to transfer data from the sensors to the control unit and receive electrical supply.

The overall weight of the device including the accessories to anchor it to the ground is

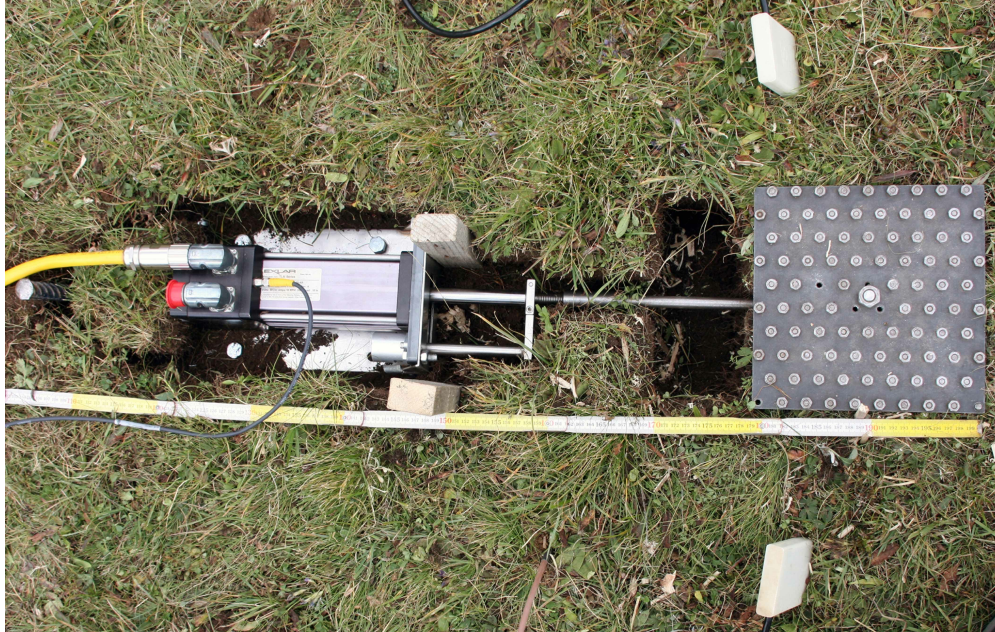


Figure 4.1: Top view of the turf's comb during a field test. From right to left: a steel plate with the heads of nails and, in the middle, the head of the steel hinge, which extends down by 8cm. A trench 20x8x10 cm. The rod, 20 cm long, connecting the central hinge to the translational axis of the engine. Exlar's linear actuator, mounted above the L-shape plate, firmly tightened with four screws. Two hard wood stakes are in front of the L-shaped plate, with a picket steel in traction behind the plate. Two TDR sensors (white) and a thermocouple (maroon cable) to measure soil water content and temperature. The cables to transfer data from the sensors to the control unit (grey) and receive electrical supply (yellow).

about 20 kg, and, even in mountain areas, a single operator can carry it on his shoulders for a short trip, install the device and run the test. If the distance or the steepness increases, two experienced operators shall be needed.

We ran laboratory tests to relate Turf's Comb energy expenditure (Ampere) to the applied shear strength (N). With no stress applied, energy expenditure is constant around 0.2 A, within a temperature ranging between - 40°C and + 65°C. As the applied stress increases to significant values (from 100 to 1000 N), we obtained a linear relationship allowing to calcu-

late its estimate from the energy expenditure measured by the device:

$$N = 260.691 \times A$$

In the shear velocity range of 0.02 - 0.5 mm/s, the laboratory tests showed no differences in energy expenditure. During field tests we kept shear velocity around 0.03 mm/s corresponding to 42 minutes to complete an entire tests (displacement: 75 mm). Prior to the field test, we measured soil thickness directly by drilling or indirectly using a georadar device. Then we prepared the test site by trimming the surface grass, to create an even surface, with a constant distance of 1 cm between the bottom of the steel plate and the underlying soil. Under these conditions, the nails can be driven into the soil for a depth of 10 cm, and the volume of the soil-roots block subjected to the test is 4000 cm³. The overall time needed to prepare the test and install the device ranges between 2 - 4 hours depending on: 1) local topographic difficulties (e.g. steepness), that determines the time needed to lay accurately the steel plate oriented according to steeper gradient, and to align accordingly the electrical engine and the connecting rod (avoiding other components in the movement generated by the device); 2) the architecture of the grass mantle, that determines the time needed to insert completely the nails into the soil (5-30 minutes) and to remove with a sieve the organic and inorganic matter trapped between the nails; 3) water content, that also influences the time to remove the organic and inorganic matter trapped between the nails.

The results of the test are discarded in case of: a) rainfall during the experiment (a common occurrence in the Dolomites during spring or fall) or b) upslope movement of the L-shaped plate-engine complex greater than 2 mm. On average, the test procedure is time-consuming, generally allowing no more than 3 tests per day.

During the test, three TDR (Time Domain Reflectometer) monitor the water content around the edges of the comb. Even if the water content doesn't change substantially, we have no

strict control on the drainage conditions, because different sensors shall be needed. Therefore, we should precautionary consider the test as partially drained.

In its fully operating mode, the Turf's Comb allows measuring the contribution to the shear strength of the four buried sides of the soil-vegetation block, (back, bottom, right, left); the front face, facing the engine and the hinge (Fig. 4.2), is free and does not contribute to the resistance. By cutting with a hand-saw one or more block facets, it is possible to measure separately the shear resistance mobilized along the remaining facets. The Turf's Comb allows 7 modes of shear strength measurements depending on the combination of sides contribution: 1) back side (200 cm^2); 2) bottom side (400 cm^2); 3) lateral sides (400 cm^2); 4) back and bottom sides (600 cm^2); 5) back and lateral sides (600 cm^2); 6) bottom and lateral sides (800 cm^2); 7) all sides (1000 cm^2). It should be noted that every single test is unique, as the experiment cannot be repeated; hence, the results should be considered independently from those collected with the same procedure, even at locations very close (1-2 m). Indeed, this might be due to the great spatial variability of thickness, composition and age of the soil mantle, as well as of the root network. However the preliminary results of tests taken at nearby locations with different configurations suggest that, it should be possible to obtain, by difference, an indirect broad estimate of the shear strength mobilized along specific sides. Overall, Turf's Comb is time-consuming and not fully- standardizable, e.g. there is no guarantee that the shear strength mobilized along a facet cut with a hand-saw is representative of a similar side in a nearby test. On the other hand, the chance to execute tests with different configurations allows a great flexibility and enables to collect valuable data, even from experiments carried out with a reduced number of configurations.

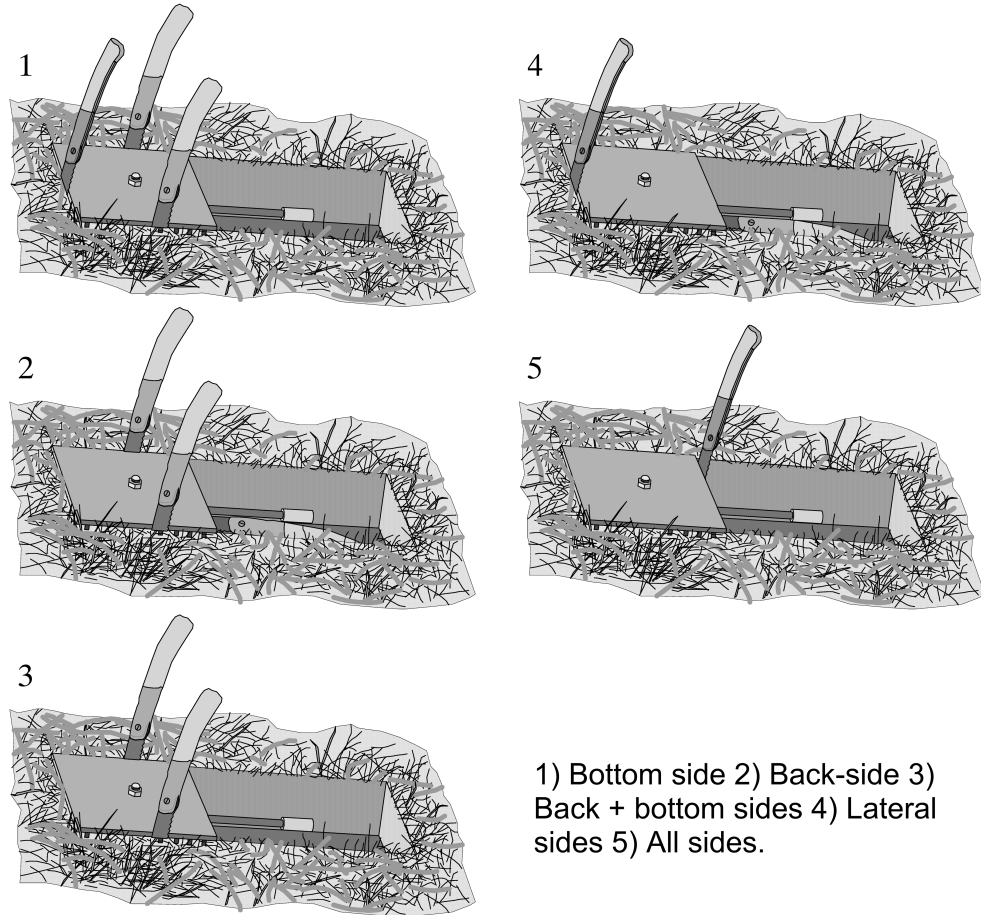


Figure 4.2: Five configurations of the Turf's comb, for cutting the soil-roots block.

4.4 Results

The shear strength (expressed in Newton on the right-hand ordinate axis) mobilized along the sides is calculated as a linear function of the energy expenditure (in Ampere on the left-hand ordinate axis) of the engine recorded during the experiment. The energy expenditure values are recorded right from the start of the test. Every graph also shows the engine's energy expenditure without any shear stress applied, corresponding to approximately 50 N. We considered this to be a negligible value, not affecting the validity of the inferences drawn from the following data analysis. An automated electronic device stops the recording after a 75 mm displacement of the steel plate.

According to the operating instructions of the electric engine Exlar used herein, between the measurements of the parameters available on the digital output of the control board, we have chosen to use the current consumption for the high linearity of the response proportional to the tensile strength. For the impulsive nature of the brushless control system, the data presented in the original form are difficult to read (Fig. 4.3). In order to extract the Root Mean Square (RMS) value of the current, an effective method is to use a low-pass filter to smooth noisy data. Recalling that sampled data consist of series of uniformly spaced in time values:

$$f_i = f(t_i) \tag{4.1}$$

where

$$t_1 = t_0 + \Delta_1 \tag{4.2}$$

with constant sample spacing Δ and $i = \dots -2, -1, 0, 1, 2, \dots$ we can apply a digital filtering technique.

Among the techniques available in the literature we have chosen the Savitzky-Golay Smoothing Filters (Press et al., 2007). The graphs presented are the result of applying a degree 3 and 161 points wide Savitzky-Golay filter to the data sets.

In Fig 4.3, the filtered curve shows clearly both the general trend, both some undulations produced by variations of the tensile strength mobilized for some tens of second by a single root or by a limited group of roots. These results should be seen as a preliminary processing, as the filter used is optimally broad for the resolution of the medium-sized features. Lower-order filters do more smoothing on broader features while higher-order filters do best

at preserving feature heights and widths, but do less smoothing on broader features.

The results of the test will be presented and discussed according to the different configurations.

1) Bottom side (400 cm², two tests, left graph in Fig. 4.4). At the end of most shear tests we observed the root area actually contributing to the resistance was less than 3% of the entire base area of the soil-roots block (Fig. 4.8). This suggests that root strength contribution is very small along the basal sliding surface. Indeed, at a depth of 10 cm, the maximum shear strength is mobilized some tens of seconds after the start of the test, and is very small, around 500 N (1.25 N/cm², i.e. 12.5 kPa). The tests conducted in the field with a Vane scissometer, at a depth ranging between 6 and 12 cm (see Chapter III) have provided high values of the peak resistance, between 80 and 100 kPa, while the residual resistance, which is much less affected by the presence of the roots, varies from 10 to 15 kPa. The value of peak resistance measured at a depth between 14 and 20 cm drops to 60-65 kPa, which is an expected result due to the almost complete disappearance of the roots at this depth; the residual resistance remains approximately stable. As the test proceeds, shear strength decreases to about 250 N (i.e. 0.65 N/cm² or 6.5 kPa) reached after complete displacement (75 mm). We argue that this value is the best estimate of undrained residual shear strength of the soil at the depth of 10 cm. The sloping linear portion of the curve reflects the shearing process; the small concavities and convexities might be ascribed to local irregularities along the sides of the block or to the presence of thicker roots.

2) Back-side (200 cm², three tests, left graph in Fig. 4.4). In this simple tensile strength test we considered the soil cohesion as negligible, root strength being the only source of shear strength. The measured range of variability of shear resistance is quite narrow, between 1100 and 1200 N (i.e. 5.5-6 N/cm², i.e. 55-60 kPa). In the various experiments, peak resistance values are reached after very different displacements (12.5 - 35 mm). According to Riestenberg (1994), first failure occurs in the roots of the trees oriented along the direc-

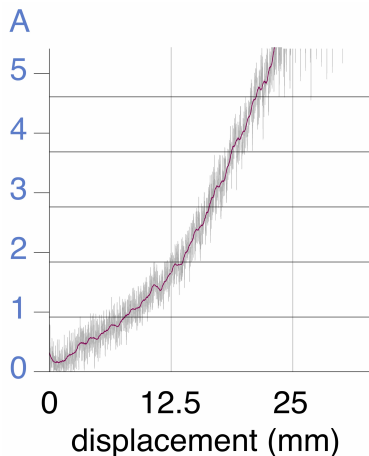


Figure 4.3: A tract of an original graph consisting of many data points (grey line), compared with the graph obtained by filtering the polygon with the Savitzky-Golay smoothing filters (black line).

tion of maximum tensile force, as they receive the largest load (cf. Schmidt et al. 2001). Our field observations seem to indicate that other factors affect the process of breaking the roots of the grass. In particular, it seems that a longer time is required to mobilize peak resistance of the longer and probably more convoluted roots. This interpretation could be confirmed by the shape of the stress-strain curve, divided in two distinct portions: the first, steeper portion, mobilizing the more abundant and shorter roots, and the second, where the longer and often thinner roots come into play; the latter are generally less prone to slipping and therefore display an elasto-plastic behavior. These graphs also show a different shape of the decreasing portion of the three curves (after peak strength): the first two curves are logarithmic, and the third is concave. These curves describe the expected drop in root area contributing to the overall shear strength of the soil-vegetation block.

3) Back + bottom sides (600 cm^2 , two tests, right graph in Fig. 4.5). The overall shape of the curves resembles that of the resistance measured on the backside, with peaks located respectively at 12 mm (1700 N, i.e. 2.8 N/cm^2 , i.e. 28 kPa) and 37 mm (2200 N, i.e. 3.7 N/cm^2 , i.e. 37 kPa). The shear resistance values, however, correspond approximately to the sum of the partial curves only for the curve with peak at 1700 N. The different values

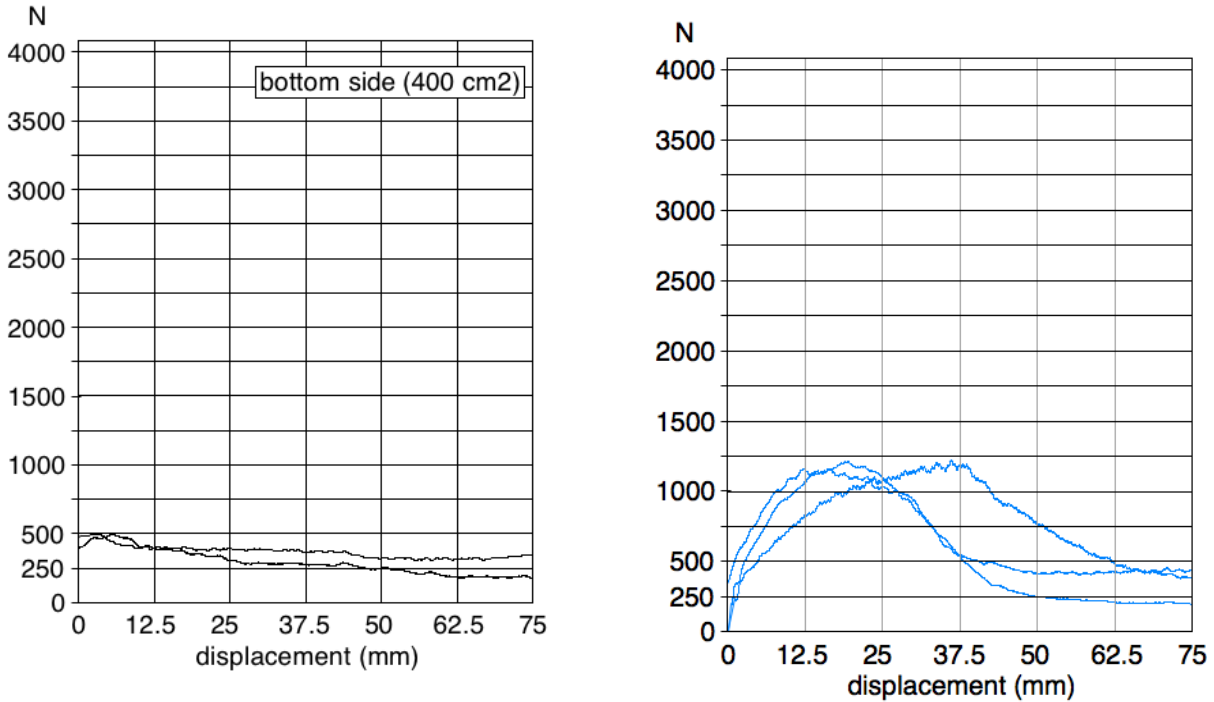


Figure 4.4: Shear strength curves obtained on ungrazed turf, according to different configurations: bottom side (left) and back side (right).

reported here highlight the current natural variability of the strength of the roots of these alpine meadows. This seems to be a realistic test, as it mimics the behavior of clod such as those that we observed in the Duron Valley frequently along the edges of shallow landslides (Fig. 4.9).

4) Lateral sides (400 cm², two tests, right graph in Fig. 4.5). During the early stage of the test, the variability of the lateral shear strength mobilized is quite high, ranging from 250 to 750 N (i.e. 0.6-1.9 N/cm², i.e. 6 - 19 kPa), similarly to the values observed in the bottom tests, and higher than those collected in the back-side tests. The peak strength values, mobilized after a 35 mm displacement are high (2000-2700 N, i.e. 5 - 6.75 N/cm², i.e. 50 - 67.5 kPa). Here too, the shear strength increases non-linearly before reaching its peak, with a steeper portion in the early phase mobilizing the shorter roots, followed by a gentler gradient where the longer and thinner roots are involved, with an elasto-plastic behavior.

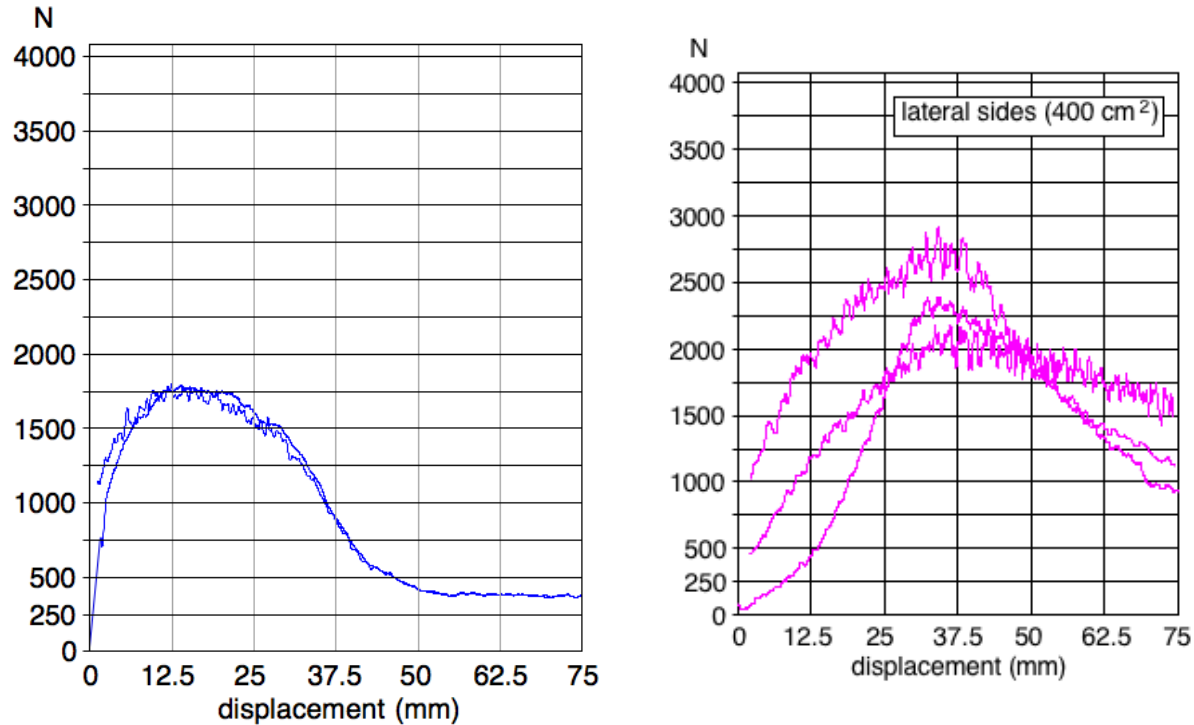


Figure 4.5: Shear strength curves obtained on ungrazed turf, according to different configurations: bottom and back sides (left) and lateral sides (right).

The post-peak portions of the stress-strain curves are different: the first is concave following the rapid drop in the mobilized root area; the second is quasi-linear with local irregularities. At the end of the tests, the recorded shear strength supplied by the lateral roots is still high (1200-1600 N, or 3 - 4 N/cm², i.e. 30 - 40 kPa), suggesting that lateral root strength plays a fundamental role in the stability of the sliding block, for two reasons: a) the area is twice that of the back facet; b) the spatial distribution of the roots allows these resistance to persist for a much longer time span.

5) All sides (1000 cm², six complete tests + one partial test, Fig. 4.6). During the early stage of the tests the shear strength mobilized along the 4 facets is relatively small (200-500 N or 0.2 - 0.5 N/cm² i.e. 2 - 5 kPa. Peak strength, ranging from high (2250 N, i.e. 2.25 N/cm², i.e. 22.5 kPa) to very high (3000 N, i.e. 3.0 N/cm², i.e. 30 kPa), is mobilized after a 5 mm displacement. The seven experiments showed a similar behavior in the pre-peak portion

of the curves, displaying a convex shape as in the lateral side tests. During the first interval (0-10 mm displacement) the rapid shear strength increase involves the contribution from both the soil and the large number of short roots; the latter are progressively broken and/or pulled as the displacement increases (10-35 mm); finally, after 35 mm of displacement, the longer and thinner roots' contribution prevails, determining an elasto-plastic behavior. Some curves show a narrow and well-defined peak, whereas others display a peak value approximately constant for a strain interval up to 15 mm. We interpret this feature as a range of equilibrium between the reduction of shear strength due to the broken and slid roots and the increase due to the mobilization of resistance from other (previously not contributing) roots. The decrease rate of shear strength after its peak value is very different in the seven experiments: from strongly concave with a final asymptotic portion, to linear, to concave-convex, to convex-concave. At the end of the tests, ultimate strength values showed a wide range, from 600 to 1300 N (i.e. 0.6 -1.3 N/ cm², i.e. 6 - 13 kPa), highest values being more frequent. Comparison with the previous graphs suggests that the high peak values and the variability of the curve shapes might be influenced by the behavior of lateral roots.

6) All sides (1000 cm², seven complete tests on undamaged grassland and two on grassland under specific conditions, Fig. 4.7). The results of the seven tests described above were compared to those collected in two tests taken on different portions of the grassland under extreme conditions. In the first case the green line shows the shear resistances of a heavily grazed turf. The mobilized shear strength at the start of the experiment is slightly greater than the values obtain in the other seven tests. This persists up to the peak strength, quite low (2200 N, i.e. 2.2 N/cm², i.e. 22 kPa), reached after a displacement of 15 mm only, during which the stress-strain curve displays a convex trend. After reaching the peak, the slightly concave curve lowers to about 900 N. We argue that peak strength is reached so early as a consequence of excessive soil compaction due to grazing, an hypothesis supported by the high values of shear strength at the start of the tests. Compaction reduces porosity and

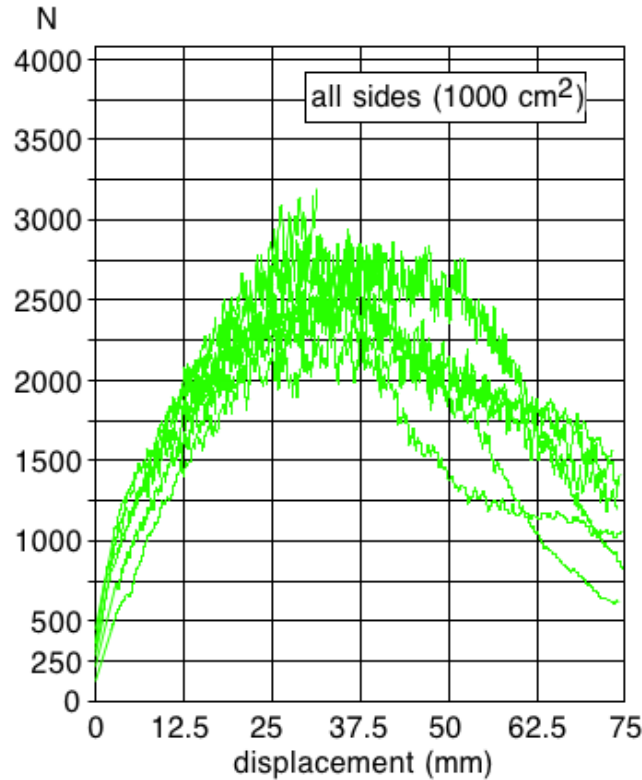


Figure 4.6: Shear strength curves obtained on ungrazed turf on all the sides of the soil-root volume.

infiltration, hindering the normal growth of the roots upslope of the backside. The anomalous low values of the peak strength and of the following descending curve suggest that even the normal development of lateral roots might have been damaged. The pink line shows the results obtained from the tests over a fully saturated soil-vegetation block, revealing a completely different pattern. Initial shear strength is close to zero, and the initial convex part of the curve increases slowly until reaching a low value of peak strength (1750 N, i.e. 1.7 N/cm^2 , i.e. 17.5 kPa) after a displacement of about 37 mm. The short descending portion of the curve is about linear with a few irregularities, reaching a lower value of 1300 N (1.3 N/cm^2 , i.e. 13 kPa).

As a whole, this figure shows quite clearly that the application of a given shear stress over undisturbed soil-vegetation blocks induces similar responses both in terms of magnitude and

timing of the mobilized resistances. Instead, if the block has been affected by external disturbing factors such as grazing or water saturation, the shear strength curve has a different shape and the shear strength is lower.

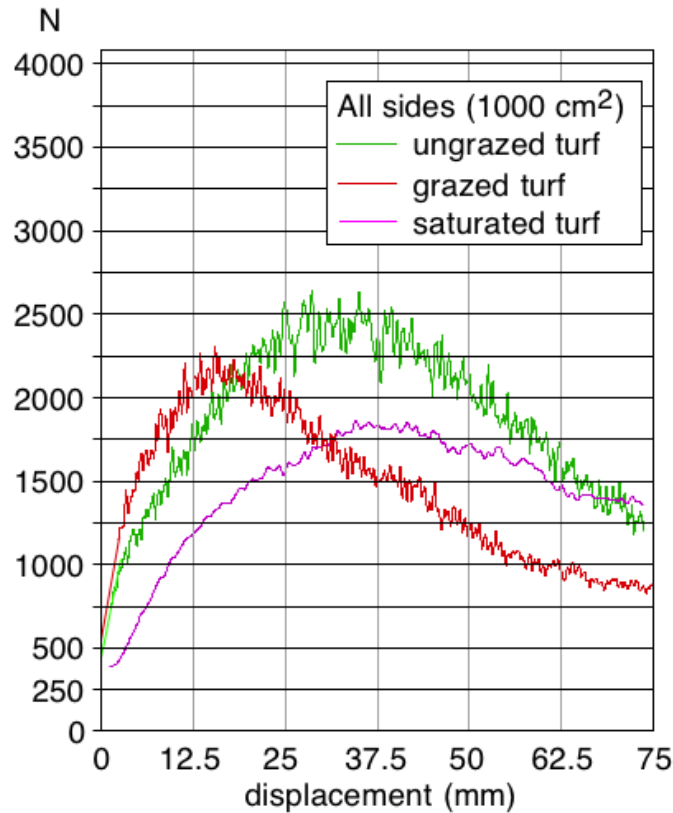


Figure 4.7: Shear strength curves obtained on ungrazed turf (green line), heavily grazed turf (red line) and saturated turf (pink line).

4.5 Discussion

The high shear strength values measured in our tests confirm that the severe alpine climate selected a grass mantle, whose extraordinary mechanical properties are particularly suitable to preserve the soil mantle, even on quite steep slopes.



Figure 4.8: Abundance of roots at the base of the soil-roots block under test; on the left, the corresponding trench obtained by extraction of the block after the test.

The results of the Turf's comb present interesting implications in the shallow landsliding triggering mechanism, because they quantify the amount of strength required to break the grass mantle covers. The setting of the test itself, reproduces the conditions occurring at the crown of a shallow landslide, where the sliding mass shears the grass cover and drags the soil and its roots downward.

However, the preliminary results presented in this work raise some critical issues:

- 1) Which displacement value is to be considered representative of complete block failure? The value at the inflection point, usually corresponding to a 10-20 mm wide tensile fracture located upslope? The peak strength value, creating a fracture about 30-40 mm wide, or even higher strength values associated to even wider fractures?
- 2) Under natural conditions (i.e. at the hillslope scale), how long should a constant shear stress be applied to generate the same shearing effect simulated in our field tests?
- 3) Which agents are responsible of the decay of the mechanical properties of the soil-vegetation blocks, thereby favoring the partial or complete failure?
- 4) In some cases we observed that the grass root apparatus of some partially failed soil

blocks was rapidly regenerating the root network connections with the adjacent soil blocks, improving the slope stability conditions by anchoring: which factor controls this process, how long did it take to develop, and which are the probabilities that this might happen at the hillslope scale triggering a shallow landslide?

More detailed data and new instruments are needed to answer such questions.



Figure 4.9: The soil slip located on the grazed slope at the mountain pass Duron (elevation 2280 m) shows a jagged crown from which are partially or fully detached decimetric clods and metric slices of the soil-grass mantle. Here, seasonal-annual phases of slipping alternates with periods during which the regrowth of the roots at the base of the clod, allows a temporary re-bonding of the clod to soil or bedrock. It should be noted that the volcanic bedrock outcrops at the toe of the slope, adjacent the road.

4.6 Conclusion

We designed and realized Turf's Comb, an innovative device suitable to measure in the field the shear strength of soil-vegetation blocks under various conditions. The device was calibrated in laboratory, but every single field test cannot be repeated, because of the spatial variability of the soil and grass mantle. However, the experiments allow collecting valuable

sets of qualitative and quantitative data on the geomechanical characteristics of the single soil-vegetation blocks. This first test lasted a few years in an alpine area located in the Central Dolomites (Italy), characterized by the *Nardetum* grass mantle (*Nardetum strictae* s.l.), with sparse shrubs (*Juniperus nana* and *Rhododendron hirsutum*). The device enabled to measure the shear strength mobilized under seven different combination of shearing surfaces: bottom surface only, back surface only, lateral surface only, back and bottom surfaces, lateral and bottom surfaces, back and lateral surfaces, and along all the four buried facets. The preliminary data of the most significant tests show that the peak shear strength of undisturbed soil-vegetation blocks is very high, and might exceed 3.0 N/cm^2 . These contributions strongly increases the stability of the soils covering the steep (35° - 40°) hillslopes of the Duron valley, whose anchoring can be effective up to a depth of 20 cm or more. The greater contribution to the shear strength comes from the lateral facets of the block, that can persist even after a 40 mm displacement (corresponding to the width of the upslope tensile fracture induced by the failure). We also observed that even after a few cm displacement, the root network could be regenerated even in partially failed soil blocks. Moreover, the field tests partially confirm the results obtained by Comino and Druetta (2010) on similar alpine grass associations (*Festuca pratensis*, *Lolium perenne* and *Poa pratensis*), obtained after controlled seeding. One of the future goals of our research is to produce new devices and establish new procedures to determine the ultimate failure conditions for the grass mantle, as well as the time and mode of loading necessary to reach them under different environmental conditions.

4.7 References

- Bischetti, G.B., Chiaradia, E.A., Simonato, T. Speziali, B., Vitali, B., Vullo, P., Zocco, A. 2005. Root strength and root area ratio of forest species in Lombardy (Northern Italy). *Plant and Soil*, 278,11-22.
- Bischetti, G.B., Chiaradia, E.A., Epis, T. and Morlotti, E., 2009. Root cohesion of forest species in the Italian Alps. *Plant and Soil*, 324(1-2), 71- 89.
- Bishop, D.M., Stevens, M.E., 1964. Landslides on logged areas in southeast Alaska. U.S. Forest Service, Northern Forest Experiment Station, Research Paper NOR-1.
- Casadei, M., Dietrich, W.E., Miller, N.L., 2003. Testing a model for predicting the timing and location of shallow landslide initiation in soil-mantled landscapes. *Earth Surface Processes and Landforms*, 28, 925–950.
- Comino E., Druetta A., 2010 The effect of Poaceae roots on the shear strength of soils in the Italian alpine environment. *Soil & Tillage Research* 106, 194–201.
- Endo, T., Tsuruta, T., 1969. Effect of trees' roots upon the shearing strength of soil. 18th Annual Rpt. of the Okkaido Branch. For. Exp. Stn. 1969, Tokio, Japan, 167-169.
- Greenway, D.R., 1987. Vegetation in slope stability. In: M.G. Anderson, Richards, K.S. (Eds) (Editor), *Slope stability*. John Wiley & Sons Ltd, New York, pp. 187-230.
- Lawrence, C.J., Rickson, R.J., Clark, J.E., 1996. The effect of grass roots on the shear

strength of colluvial soils in Nepal. *Advances in Hillslope Processes* 2, 857–868.

Marston, R.A., 2010. Geomorphology and vegetation on hillslopes: Interactions, dependencies, and feedback loops. *Geomorphology*, 116(3-4): 206-217.

Normaniza, O., Barakban, S.S., 2006. Parameters to predict slope stability – soil water and root profiles. *Ecological Engineering* 28, 90–95.

Norris, J.E. 2005. Root reinforcement by hawthorn and oak roots on a highway cut-slope in Southern England. *Plant Soil*, 278:43–53.

Pollen, N., 2007. Temporal and spatial variability in root reinforcement of streambanks: accounting for soil shear strength and moisture. *Catena* 69, 197–205.

Press W.H., Teukolsky S.A., Vetterling W.T., Flannery B.P. 2007. *Numerical recipes: the art of scientific computing* (third edition, 766-772, Cambridge University Press.

Riestenberg, M.M., 1994. Anchoring of thin colluvium by roots of sugar maple and white ash on hillslopes in Cincinnati. U.S. Geological Survey, Bulletin 2059-E.

Roering J. J., Schmidt K. M., Stock J. D., Dietrich W. E., Montgomery D. R., 2003 Shallow landsliding, root reinforcement, and the spatial distribution of trees in the Oregon Coast Range. *Can. Geotech. J.* 40: 237–253 (2003).

Sakals, M.E., Sidle, R.C., 2004. A spatial and temporal model of root cohesion in forest soils. *Can. J. For. Res.* 2004 34:950–958.

- Schmidt, K.M., Roering, J.J., Stock, J.D., Dietrich, W.E., Montgomery, D.R., Schaub, T., 2001. Root cohesion variability and shallow landslide susceptibility in the Oregon Coast Range. *Canadian Geotechnical Journal* 38 (1), 995-1024.
- Schiechl, H.M., 1991. Ground bioengineering systems. In: *Ground Bioengineering Techniques for Slope Protection and Erosion Control*. Blackwell Science Ltd., UK, pp. 16-17.
- Tosi, M., 2007. Root tensile strength relationships, their slope stability implications of three shrub species in the Northern Apennines (Italy). *Geomorphology* 57, 268-283.
- Waldron, L.J., 1977. The shear resistance of root-permeated homogeneous, stratified soil. *Soil Science Society of America Journal* 41 (3), 843-849.
- Waldron, L.J., Dakessian, S, 1981. Soil reinforcement by roots: calculation of increased soil shear resistance from root properties. *Soil Sci.*, 132, 427-435.
- Wu, T.H., McKinnell, W.P. III, Swanston, D.N., 1979. Strength of tree roots and landslides on Prince of Wales Island, Alaska. *Can. Geotech. J.*, 16:19-33.
- Wu, T.H., Beal, P.E., Lan, C., 1988. In-situ shear tests of soil-root system. *J. Geotech. Eng. ASCE* 1988, 114:1376-1394.
- Wu, T.H., Watson, A., 1998. In situ shear tests of soil blocks with roots. *Can. Geotech. J.* 35, 579-590.

CHAPTER 5

Hillslope stability analysis: merging EO (Earth Observation) and ground-based data

5.1 Introduction

¹ Physically based models have been successfully used to reproduce the physical processes that govern the landslides occurrence. Their formulation implies some limitations, mainly related to the spatial variability of the input data and the hydrological assumptions of the model itself.

Thanks to the extremely high density of the data available in the study area (Chapter III), we tried to reduce the uncertainty of geomechanical and geotechnical parameters that characterize the land covers. The aim of this chapter is indeed to merge into physically based slope stability models the Earth Observation and detailed ground-based data, both retrieved through innovative methods (Chapters II-III-IV). The analysis was performed at two different scales, using SHALSTAB (Montgomery & Dietrich, 1994), TRIGRS-unsaturated (Baum et al., 2008) and SLIDE (Rocscience). With SHALSTAB and TRIGRS we modeled the shallow landsliding susceptibility at the basin scale while we used SLIDE to analyze the vegetation effect on slope stability at the hillslope scale.

Geomechanical and geotechnical parameters exert a strong control in the stability analyses;

¹*Article in preparation*

in this work we gave particular attention to the cohesion of the soils, since we derived this parameter from different laboratory and field measurements. Cohesion is a key-component of the shear strength of a soil, it can be divided into two main parts: the “true cohesion”, which is caused by electrostatic forces, cements, roots (the so called root’s pseudo-cohesion) and the “apparent cohesion”, driven by the negative and capillary pressures in unsaturated porous media. In the SHALSTAB and TRIGRS analyses, which operate at the catchment scale, the cohesion value that must be entered comprehends both the components, whereas in SLIDE, the cohesion of soil doesn’t comprehend the pseudo-cohesion contribution of the roots (which is calculated in back-anaysis).

The prediction skills of the models were assessed comparing the simulation results with the observed instability phenomena in the Duron catchment. Potentials and limits of the three methods are discussed in this chapter.

Despite the models depict three different scenarios of hazard, they shall be considered as complementary tools for understanding the complex interaction between the land cover geomechanical properties and the landslides distribution.

5.2 SHALSTAB

SHALSTAB (SHALlow landsliding STABility model) (Dietrich et al., 1992; Dietrich et al., 1993; Montgomery and Dietrich, 1994) is a physically based stability model, which couples a steady state hydrologic model with the infinite slope stability analysis. This model assumes that the steady state rainfall and soil transmissivity control the slope-parallel fluctuations of the water table, whereas the failure plane is located at the interface between soil and bedrock, parallel to the ground surface.

5.2.1 The hydrological model

SHALSTAB uses a steady-state hydrological model, TOPOG (O’Loughlin, 1986), which predicts the degree of saturation in response to a steady state rainfall and captures the effects of surface topography on shallow runoff and overland flow. This model divides the surface in topographic elements defined by the contributing area (a), which drains across the contour length of the lower boundary to each element b (Fig.5.1). Given a steady-state rainfall, the degree of wetness (h/z) is expressed as:

$$\frac{h}{z} = \frac{a}{b \sin \theta} \frac{q}{T} \quad (5.1)$$

where h is the thickness of saturated soil,

z is the total soil thickness,

a is the catchment draining across a contour of length b ,

q is the net rainfall rate,

θ is the local slope, and

T is the soil transmissivity.

The hydrological parameters are assumed constant across the investigated area (transmissivity, hydraulic field saturated conductivity and ground resistance to runoff and erosion) and the boundary between the soil and bedrock is assumed abrupt.

5.2.2 The slope stability model

The slope stability is analyzed using the infinite slope model (Taylor, 1948), which assumes that the sliding surface is parallel to the topographic surface as well as the piezometric sur-

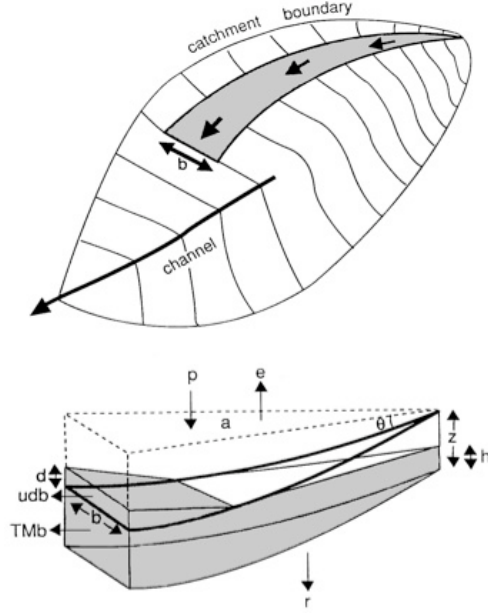


Figure 5.1: Plan view and cross section of area draining across the contour length, b , as defined by "flow lines" generated by the program TOPOG (O'Loughling, 1986). In the cross section, the heavy line depicts the ground surface. The stippled area is the shallow subsurface flow and saturation overland flow with discharge of Tmb and udb , respectively. Here q equals precipitation, p , minus evaporation, e and deep drainage, r ; a is drainage area, h, z , and d (measured normal to the ground surface) are the thickness of the potentially unstable mass, the thickness of the subsurface saturated flow, and thickness of the saturation overland flow; u is the mean overland flow velocity parallel to the ground surface. T is the transmissivity and M is $\sin\theta$ (Dietrich et al., 1992).

face (Fig.5.2).

According to the Mohr-Coulomb failure criterion:

$$\tau = c' + (\sigma - u) \tan \phi' \quad (5.2)$$

where τ is the shear strength of the soil,

σ is the normal stress acting on the slope,

c' is the effective cohesion,

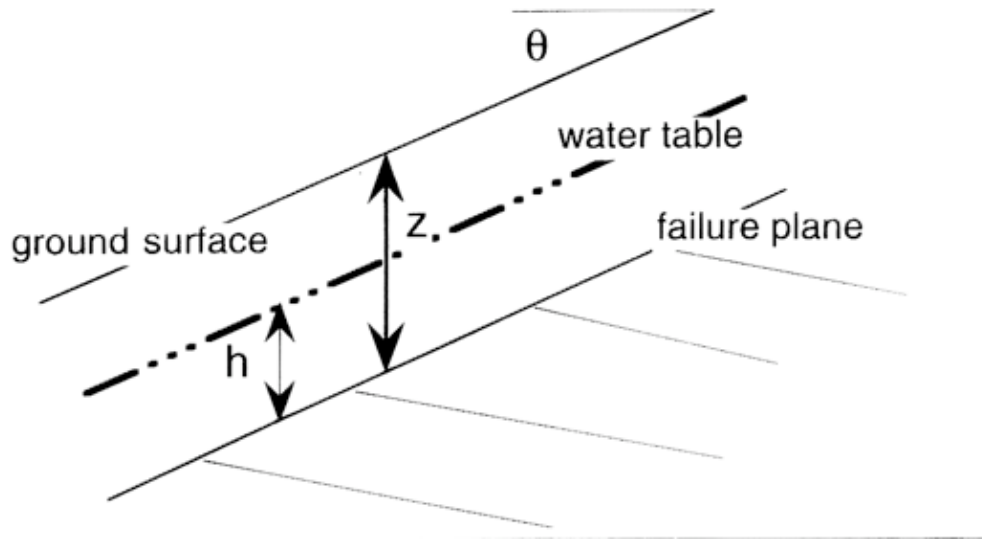


Figure 5.2: The infinite slope method: θ is the local slope, h is the thickness of the saturated soil and z is the total soil thickness

u is the pore water pressure, and

ϕ' is the effective friction angle.

Substituting in (5.2) the normal and tangential component and assuming a cohesionless soil, the equation becomes:

$$\rho_w g z \cos \theta \sin \theta = (\rho_s g z \cos^2 \theta - \rho_w g h \cos^2 \theta) \tan \phi' \quad (5.3)$$

where ρ_w and ρ_s are the water and soil density and g is the gravitational acceleration.

By solving this equation for the degree of wetness (h/z) and coupling this equation with the hydrological model we obtain:

$$\frac{a}{b \sin \theta} \frac{q}{T} = \frac{\rho_s}{\rho_w} \left[1 - \frac{\tan \theta}{\tan \phi'} \right] \quad (5.4)$$

Rearranging equation (5.4) we can express the shallow landsliding susceptibility as the ratio between the precipitation and the soil transmissivity:

$$\frac{q}{T} = \frac{\rho_s}{\rho_w} \left[1 - \frac{\tan \theta}{\tan \phi} \right] \frac{b}{a} \sin \theta \quad (5.5)$$

Four stability classes are defined: unconditionally stable, unconditionally unstable, stable and unstable (Fig.5.3). Unconditionally unstable cells have a slope angle greater than the friction angle; their stability is not influenced by the wetness condition (they're unstable even when completely dry). The slope stability threshold separates the stable/unstable field; topographic elements where:

$$\frac{a}{b} \geq \frac{T}{q} \sin \theta \left(\frac{\rho_s}{\rho_w} \right) \left[1 - \frac{\tan \theta}{\tan \phi} \right] \quad (5.6)$$

are predicted to be unstable (Fig.5.4).

The hydrological ratio (q/T) is used to assign the relative landslide hazard; the model results should then be validated with reliable and detailed field data. In the SHALSTAB analysis, unconditionally unstable cells are predicted to be unstable even when dry. Since this analysis is not time-dependent (due to the assumptions of the hydrological model), the unconditionally unstable cells have to be interpreted as sites of likely failure in the future. In reality, unconditionally unstable areas are often outcrops, where, even if there is no available material to fail (soil depth is zero), the slope exerts its maximum influence in the stability analysis. This approach is well suited to investigate the topographic control on shallow landsliding: the reliability of the analysis is therefore strictly related the quality of the topographic data. SHALSTAB was originally designed for soil-mantled hilly terrains with impermeable bedrock and colluvial deposits; its approach is not well suited for terrains dominated by deep seated

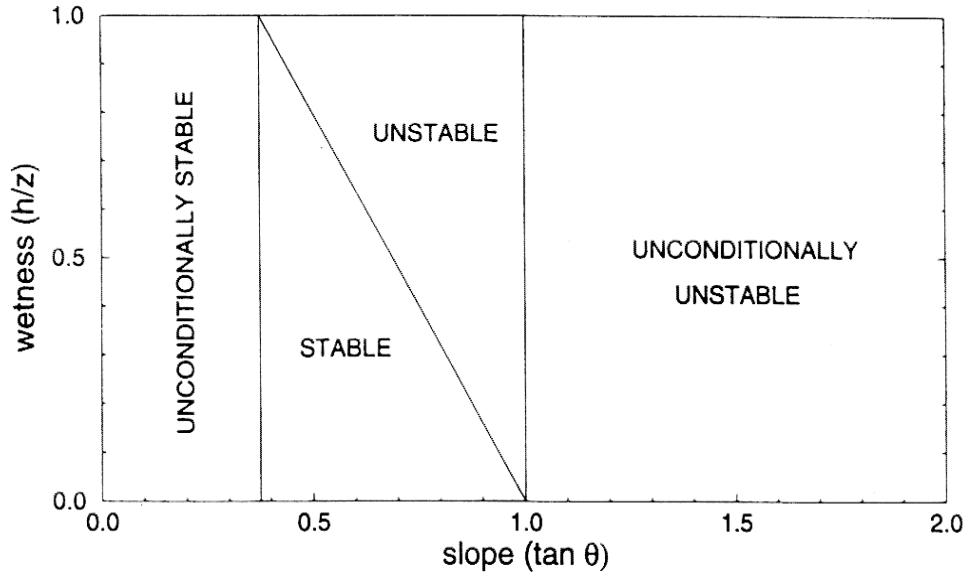


Figure 5.3: Definition of stability fields on plot of wetness (h/z) versus slope ($\tan \theta$) (Montgomery & Dietrich, 1994).

landslides and rocky terrains.

The simple mathematical formulation and the small number of input parameters ensure that this model is suitable for predicting shallow landsliding susceptibility at regional scales; however, at bigger scales, the model tends to overpredict the landslide distribution (Casadei et al., 2003).

5.2.3 Data set

We run SHALSTAB on a high-resolution DEM (Digital Elevation Model) derived from LiDAR data, acquired on November 2007 from an airborne sensor (ALTM 3100 OPTTECH). Mean flying speed was 250 km/h and the elevation ranged between 1000 -1800 m a.s.l. The maximum scan angle of the sensor was 25° and the mean point density is 8 pts per 6.25 m^2 , with an average distance of 0.9 m between each point and a vertical accuracy of 15 cm

| Property | Unit | Value | Source |
|---|-------------------|------------------------|---|
| Bulk density | g/cm ³ | 1.11 | Laboratory analyses |
| Friction angle | ° | 28/31 | Laboratory analyses and geological survey |
| Soil and root cohesion | Pa | 0-10000 | Back analysis and literature |
| Hydraulic field saturated conductivity (Ks) | m/s | 4.1 x 10 ⁻⁶ | Guelph permeameter measurements |
| Soil depth | m | 0.5 | GPR survey |

Table 5.1: List of input parameters for the SHALSTAB simulations

(LiDAR survey Technical Report). First and last returns were recorded to generate a DTM (Digital Terrain Model) and a DEM with 2x2 m cell size. The depression points present within a DEM were filled using the Tarboton algorithm (Tarboton, 1997) and to define the drainage direction we used the “pure D8” method (O’Callaghan and Mark, 1984).

The input parameters of the model were retrieved from laboratory and field data (Table 5.1). Neglecting in a first approximation the transport of sediment along the slope, we attributed $\Phi' = 28^\circ$ to the soil overlaying pillow lava - pillow breccia, and $\Phi' = 31^\circ$ to that overlaying hyaloclastites and volcanic turbidites (Fig.5.5). The daily effective precipitation was set to 100 mm/day, according to the closest meteorological station (Moena-T0096) that was active at the time of writing the manuscript. A new meteorological station has been recently activated inside the study area (Campitello-T0229) but the data are available only from February 2012 and no significant precipitation events occurred in the following months. The SHALSTAB simulations were run on JGrass, an open source GIS, dedicated mostly to hydrological and geomorphological analyses. The release we used (1.1.1) allows us to differentiate areas by friction angles (<http://code.google.com/p/jgrass/>).

5.2.4 Results

The output of each simulation is a shallow landslide susceptibility map, based on 2x2 m cell, divided into three classes: unconditionally stable, unconditionally unstable, and with conditioned stability.

We run SHALSTAB in back-analysis (Li and Zhao, 1984), searching for the best fit between simulation results and the inventory of surveyed landslides and outcrops.

During the trial-and-error process of the back-analysis we adjusted systematically the cohesion value of the soil-roots system within a reasonable range of values (0-5 kPa)(Carrara et al., 2008). Two types of simulation were compared: in the first set we assumed a constant cohesion throughout the basin, in the second one, the cohesion value was divided in classes, according to the EO-classified map (see Chapter II).

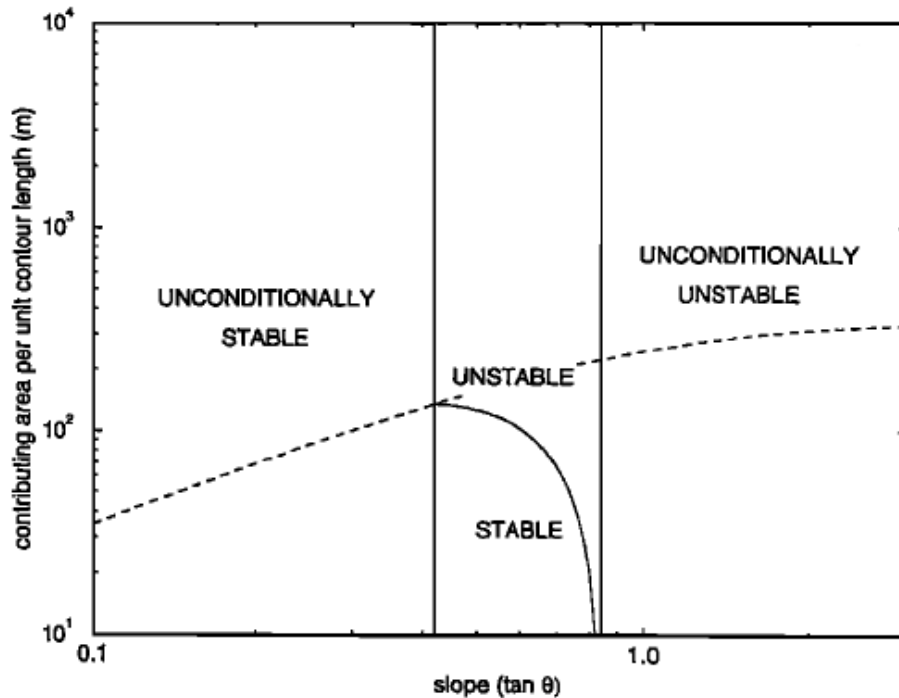


Figure 5.4: Definition of stability fields on plot of topographic ratio (a/b) versus slope ($\tan \theta$); the dashed line represents the threshold of ground saturation (Montgomery & Dietrich, 1994).

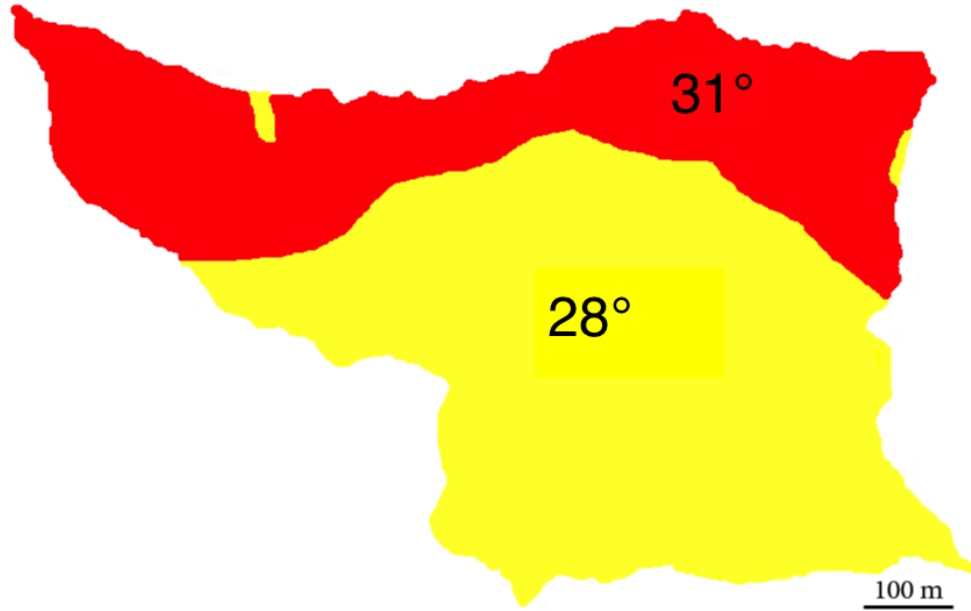


Figure 5.5: Map of the friction angle used for the SHALSTAB simulations.

| Case | 1 | 2 | 3 | 4 |
|-----------|-------|-------|-------|-------|
| Bare soil | 0 | 0 | 500 | 1000 |
| Grazed | 0 | 500 | 1000 | 1500 |
| Ungrazed | 500 | 1000 | 1500 | 2000 |
| Trees | 5000 | 5000 | 5000 | 5000 |
| Buildings | 10000 | 10000 | 10000 | 10000 |

Table 5.2: Cohesion values (Pa) attributed to each soil cover class, obtained by satellite image classification.

In the EO map, the basin has been divided into five classes of land cover: we attributed *a priori* 5000 Pa and 10000 Pa of cohesion to the Trees and Buildings classes respectively; only in the bare soil, grazed and ungrazed classes we varied the cohesion value (Table 5.2, cases 1-4). We kept the cohesion of the Trees and Buildings classes constant and high because those land covers offer a higher cohesion contribution in respect of the other three classes; trees and artificial objects are not involved in the shallow mass movements. In the remaining three classes (bare soil, grazed and ungrazed grass) we varied the cohesion by steps of 500

Pa, under the assumption that bare soil has less cohesion than grazed grass, which in turn has less cohesion than ungrazed grass. Through the distribution of the instability classes in the source areas, the results obtained using the EO map (Fig. 5.7) were compared with the results of the simulations that were run with constant cohesion throughout the catchment's area.

The predictive skills of the models have been evaluated using the ROC plots. This validation method has been appointed as a valid tool to evaluate the efficiency of mathematical models in natural hazard analysis (Begueria, 2006).

A ROC (receiver operating characteristics) curve is a graphical plot, which illustrates the performance of a model as its discrimination threshold is varied. The graph is created by plotting the true positive rate (TPR) against the false positive rate (FPR), at various threshold settings. TPR is also known as Sensitivity, which represents the proportion of positive cases correctly predicted while the FPR is the Specificity, which is the proportion of negative cases correctly predicted. The more separated the ROC curves appear in the relation to the diagonal straight line, the better the model discriminates between safe and unsafe locations. The results of the plots indicate that distributing the cohesion values on the EO-classified classes, the classification accuracy increases (Fig. 5.6). The AUC (area under curve), which represents the probability that the model will rank a randomly chosen positive instance higher than a randomly chosen negative one, is indeed slightly higher for the simulations that use a distributed cohesion map (0.76 Vs 0.73 of the constant cohesion map).

Since these curves are constructed using the back-analysis of the cohesion values, from the same plots it's also possible to determine the set which discriminate better the instability: it is represented by the point that is located the furthest from the 1:1 line. For this set of simulations, the best model accuracy is achieved attributing 500 Pa of cohesion in the bare soil class, 1000 Pa in the grazed class and 1500 in the ungrazed one (case 3 in Table 5.2).

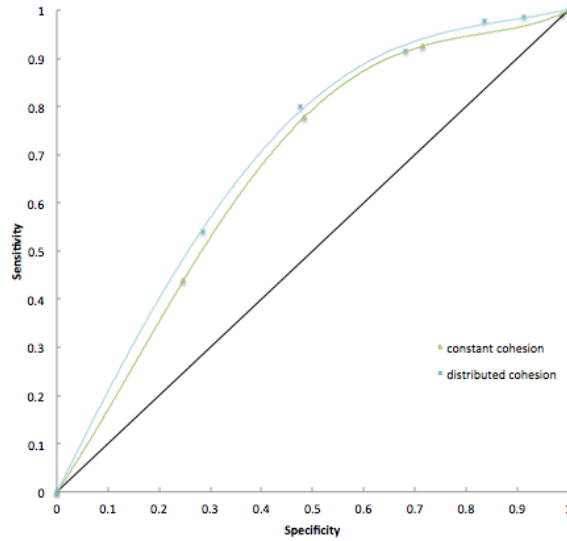


Figure 5.6: Receiver Operating Characteristics (ROC) curves used to assess the predictive performance of the model. The two curves are obtained considering a constant cohesion (green curve) and distributing the cohesion on the EO-classified map (blue curve).

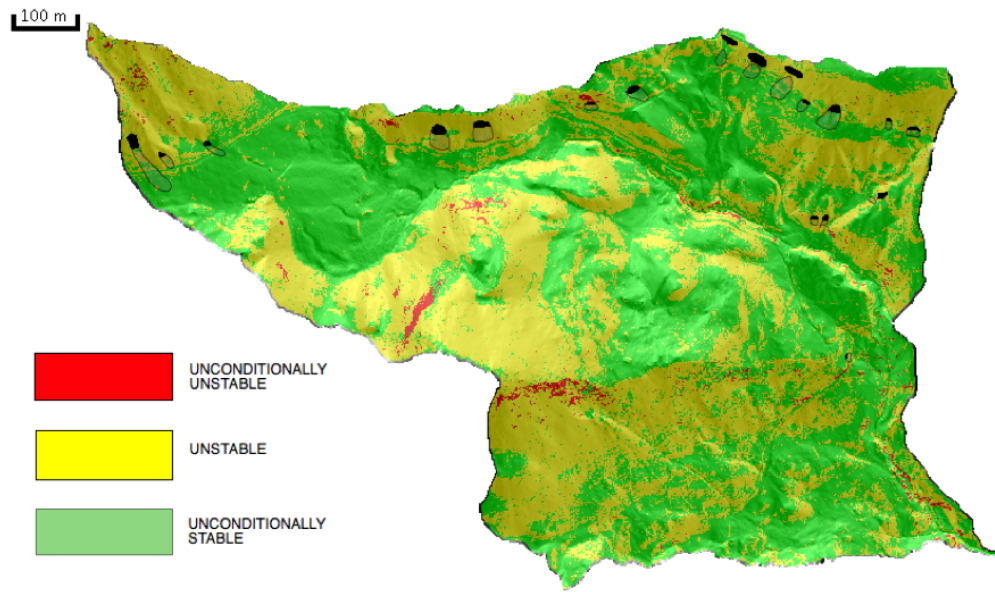


Figure 5.7: SHALSTAB susceptibility map of the Duron catchment with differentiated land cover classes (case 3, Table 5.2). The black pixels represent the source areas, while the landslide bodies are delimited by the black polylines.

5.2.5 Shalstab with the soil depth map

All the simulations we run using SHALSTAB have also been performed using the soil depth map, instead of a constant averaged value (0.5 m). The soil depth map has been constructed interpolating the data of the GPR surveys (Fig. 3.3), with the ordinary kriging method. The map we used for the SHALSTAB simulations has been modified from the original because the JGrass code attributes all the pixels, with soil depth less than 10 cm, to a class named "bedrock". Regardless of the hydrological, topographical and geomechanical conditions, the soil depth is the only criterium used to classify a pixel as "bedrock".

Using the original soil depth map, most of the pixels in the source areas, and generally in the north-eastern part of the basin (where most of the landslide are located), belonged to the "bedrock" class. To overcome this problem we modified the soil depth map, attributing 20 cm to all the pixels with soil depth less than that. Simulations were run using the same sets of geomechanical parameters (Table 5.1) and distributed cohesion (Table 5.2). In the soil map simulation we varied also the transmissivity (which is obtained by multiplying the soil depth and the hydraulic conductivity).

Given the same cohesion values, our results indicate that the percentage of stable cells, with the soil depth map is greater (Fig. 5.9). The difference of stable/unstable cells becomes more visible if we compare the cells inside the source areas, instead of the cells in the entire basin.

To test the accuracy of this method we constructed the ROC plot and compared it with the curve obtained considering a constant soil depth (green line in Fig. 5.6). The new plot has completely different trend (purple line in Fig. 5.10): the curve is markedly closer to the 1:1 line. Given the fact that the accuracy of the model increases if the curves are further from the diagonal, the simulations with the soil depth map appear less predictive than the constant soil depth ones. The AUC for the variable soil thickness is only 0.56.

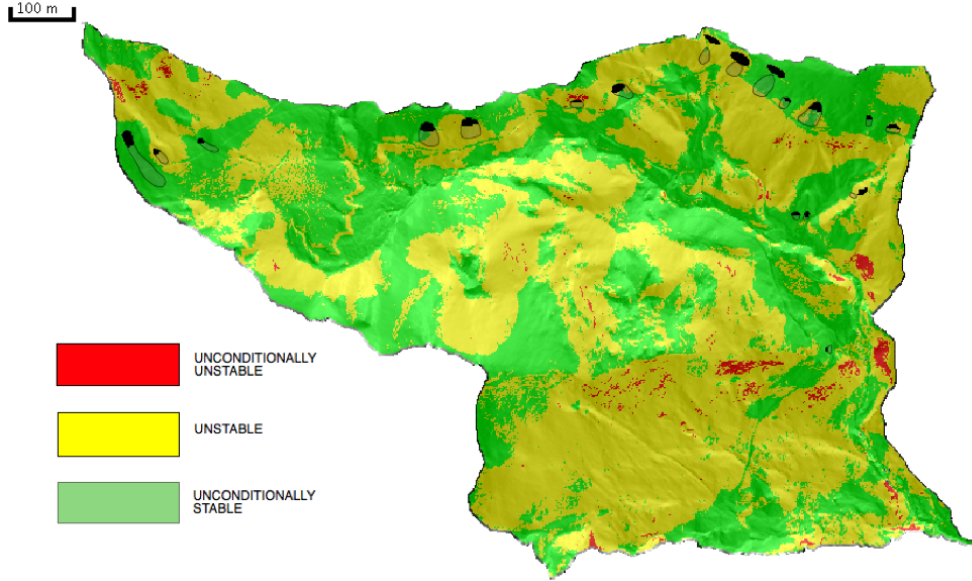


Figure 5.8: SHALSTAB susceptibility map of the Duron catchment with constant cohesion (1000 Pa) and variable soil depth. The black pixels represent the source areas, while the landslide bodies are delimited by the black polylines.

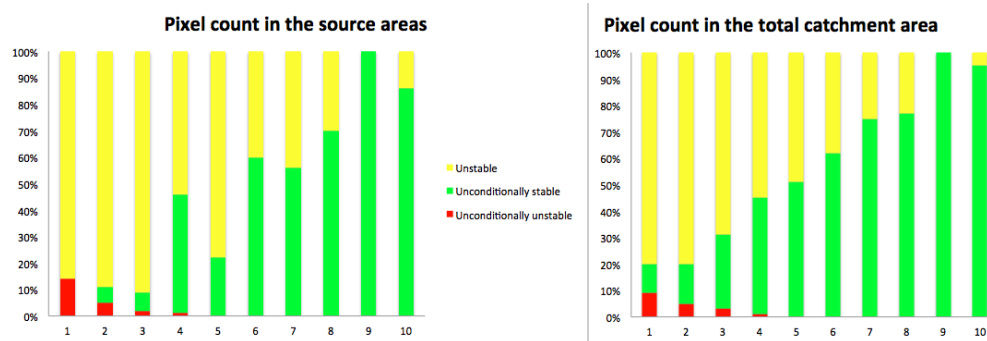


Figure 5.9: Pixel count in the source areas (left) and in the the entire basin (right). The odd columns represent the simulation with constant soil depth at increasing cohesion values of 500-1000-1500-2000-3000; the even columns represent the simulations with the soil depth map at the same cohesion intervals.

Several hypotheses have been formulated to explain this behavior:

- i) In the source areas, the thickness in the soil depth map is lower than the value used in the constant soil depth simulations (0.5 m). Given the same hydrological input parameters (transmissivity and precipitation), the water table that rises from the impermeable boundary is very low, both because of the high permeability of these soils, and because the contributing

areas, upslope the source areas, is small (the surveyed landslides are close to the watershed upper boundary). Hence, given the same water table height, a thicker soil will be more unstable. ii) The distribution of the soil thickness across the basin is not linked directly with the SHALSTAB instability distribution. While cohesion, slope, friction angles and other parameters have a clear relationship with the instability distribution (*e.g.* the higher the cohesion, the greater the number of stable cells), the soil depth doesn't hold this kind of constrain. The soil depth model is not directly linked with the topography, because the data derive from GPR surveys conducted in the field. The surveyed soil depth map represents the real distribution of the soil thickness across the basin, which reflects the effects of glaciations and hillslope's processes: its distribution across the basin is not strictly related to the topographic gradient. To test this hypothesis we correlated cell-by-cell the values of the soil depth and the slope. The plot that results (Fig. 5.11) shows clearly that these two variables have no correlation.

As a final remark, our results suggest that implementing a extremely detailed map (soil depth) into a rather simply mathematically-formulated model (SHALSTAB) doesn't lead to any improvement in the model performance. Contrarily, it generates a counter-effect randomizing the number of correctly predicted cells.

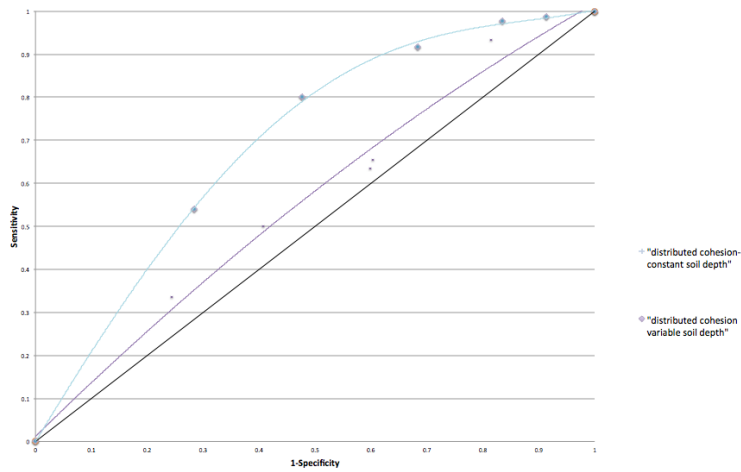


Figure 5.10: Receiver Operating Characteristics (ROC) curves used to assess the predictive performance of the model. The two curves are obtained considering a constant soil depth (blue curve) and using the soil depth map (purple curve).

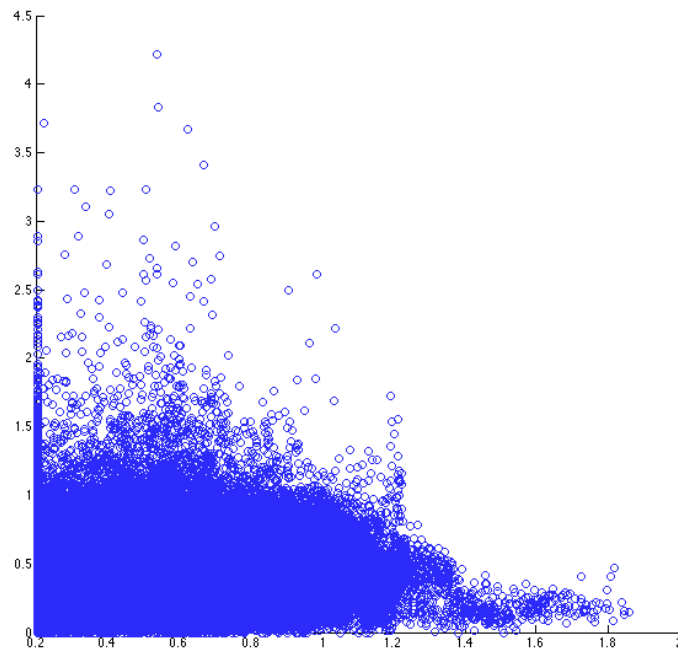


Figure 5.11: Scatterplot of the soil depth values (x -axis) and slope values (y -axis).

5.3 TRIGRS

TRIGRS-unsaturated (Transient Rainfall Infiltration and Grid-Based Regional Slope-Stability Model) is a USGS program designed for modeling the timing and distribution of shallow landslides (Baum et al., 2008). The model assumes that shallow landslides are tension-saturated: timing and location of landslides are predicted by modeling the pore-pressure changes. Slope stability is expressed by the factor of safety, computed using a simple infinite slope analysis on a cell-by-cell basis.

5.3.1 The hydrological model

TRIGRS-unsaturated uses the original infiltration model proposed by Iverson's (2000) and extended by Baum et al., (2002) in order to account for variable rainfall intensities and durations.

Iverson's solution consists of a steady component and a transient component. The steady seepage component is defined by the initial conditions of water table depth and a steady infiltration rate. The transient component assumes one-dimensional, vertical downward flow, with a simple specified time-varying flux of fixed duration and intensity. The generalized solution used in TRIGRS is given by:

$$\Psi(Z, t) = (Z - d)\beta + \tag{5.7}$$

$$+ 2 \sum_{n=1}^N \frac{I_n Z}{K_s} \left\{ H(t - t_n) [D_1(t - t_n)]^{\frac{1}{2}} \text{ierfc} \left[\frac{Z}{2[D_1(t - t_n)]^{\frac{1}{2}}} \right] \right\} + \tag{5.8}$$

$$- 2 \sum_{n=1}^N \frac{I_n Z}{K_s} \left\{ H(t - t_{n+1}) [D_1(t - t_{n+1})]^{\frac{1}{2}} \text{ierfc} \left[\frac{Z}{2[D_1(t - t_{n+1})]^{\frac{1}{2}}} \right] \right\} \tag{5.9}$$

where Ψ , is the ground water pressure head at time t and at depth Z , which is positive in the downward direction.

$Z=z/\cos\alpha$, where z is the slope-normal depth and α is the slope angle, d is the steady water table in the z -direction,

$$\beta = \cos^2\alpha - (I_{ZLT}/K_s),$$

K_s is the hydraulic field saturated conductivity,

I_{ZLT} is the steady (initial) surface flux,

I_{nZ} is the surface flux of a given intensity for the n^{th} time interval,

D_0 is the saturated hydraulic diffusivity and

$$D_1 = D_0\cos^2\alpha.$$

The function $ierfc(n)$ is:

$$ierfc(\eta) = \frac{1}{\sqrt{\pi}} \exp(-\eta^2) - \eta \operatorname{erfc}(\eta) \quad (5.10)$$

where $\operatorname{erfc}(\eta)$ is the complementary error function.

5.3.2 The slope stability model

The stability analysis is computed using the infinite-slope approach (Taylor, 1948) and expressed through the factor of safety F_s , defined by the ratio of resisting basal Coulomb friction the gravitationally induced downslope basal driving stress. At a depth Z , the factor of safety is expressed as:

$$FS(Z, t) = \frac{c}{\gamma_s Z \sin \alpha \cos \alpha} + \frac{\tan \phi}{\tan \alpha} + \frac{(-\Phi \gamma_w) \tan \phi}{\gamma_s Z \sin \alpha \cos \alpha} \quad (5.11)$$

A factor of safety equal or below the unity suggest that the slope is unstable and a landslide is predicted. The first term in Equation 5.11 is the soil cohesion, the second is the friction angle and the third term identifies the transient pressure due to surface fluxes, which decrease the FoS value as pressure increases.

5.3.3 Data set

Table 5.3 list all the parameters used for the TRIGRS analysis. Hydraulic parameters were computed using the software ROSETTA (Schaap et al., 2001), which implements hierarchical pedotransfer functions (PTFs) to estimate the water retention parameters (residual, saturated water contents, θ_r and θ_s respectively, and *alpha*).

We used the model in back-analysis considering two extreme cases of precipitation and varying the cohesion values across the land cover classes defined by the EO map (Table 5.4). The first rainfall event was recorded in June 2011 from the closest meteorological station (Moena T0026) in the neighbouring valley (Fassa): a cumulative precipitation of 150 mm in 8 days, of which 40 mm fell on the last day (peak event). This precipitation (afterwards referred as the "Moena" event) represents a normal-low intensity event for the Fassa valley climate. In the second test we considered an "extreme" precipitation event: 260 mm in 9 hours, 120 mm of which fell into the last two hours. These types of severe rainfalls are fairly common in the Duron basin, since the study area occupies a high-altitude range (1900 - 2400 m a.s.l.) and suffers a strong orographic effect caused by the surrounding peaks. Since January 2012 a new meteorological station (Campitello T0029), located in the study area

near the Do Col d’Aura mountain stable, started to record precipitation data. However, at the time of writing this manuscripts, no extreme precipitation event occurred.

| Property | Unit | Value/Range |
|---------------------------------------|----------------------|-----------------------|
| Cohesion | Pa | 0-50000 |
| Friction angle | (°) | 28 |
| Unit weight of soil | (g/cm ³) | 1.11 |
| Hydraulic diffusivity | (m ² /s) | 6×10 ⁻⁰⁵ |
| Hydraulic soil saturated conductivity | (m/s) | 4.2×10 ⁻⁰⁶ |
| Soil saturated volumetric content | – | 0.47 |
| Soil residual volumetric content | – | 0.05 |
| alpha | – | 5 |

Table 5.3: Parameters, units and values used for the TRIGRS analysis

| Land Cover Class | Case 1 (Pa) | Case 2 (Pa) | Field values (Pa) |
|-------------------------|--------------------|--------------------|--------------------------|
| Bare soil | 0 | 500 | 2000 |
| Grazed | 500 | 1500 | 20000 |
| Ungrazed | 1000 | 3500 | 30000 |
| Trees | 5000 | 5000 | 40000 |
| Buildings | 10000 | 10000 | 50000 |

Table 5.4: Cohesion values (Pa) attributed to the different land cover classes in the TRIGRS analyses.

5.3.4 Results

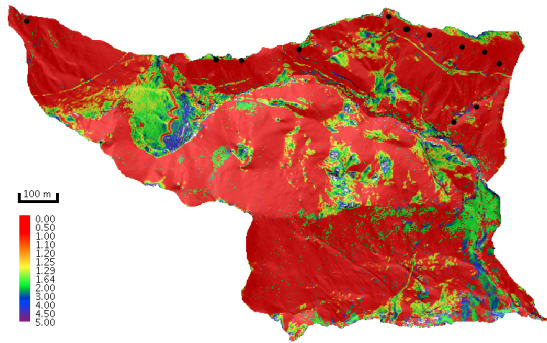
Figure 5.12 reports the simulation performed using the "Moena" event (left column figures) and the extreme one (right column figures), each row (*a-b*, *c-d* and *e-f*) has the same set of cohesion values (Table 5.4).

The instability scenario depicted by the model revealed that the longer rainfall event ("Moena"),

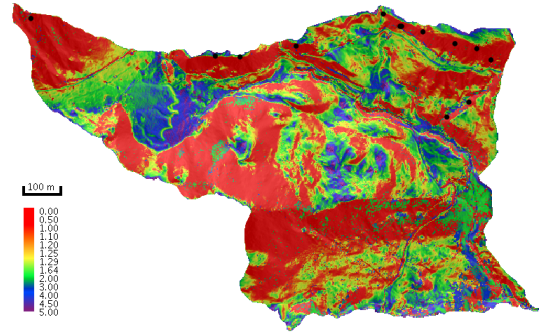
even if less intense, causes a more widespread distribution of unstable cells. In the "extreme" precipitation event, limiting the TRIGRS analysis to the pre-peak precipitation (i.e. shortening the precipitation time to 7 hours, neglecting the last intense interval), we obtain that the unstable cells are only 0.1% less (5.2% are the unstable cells in the entire catchment, with the "extreme" precipitation event and 5.1% for the "shortened" one). The process of soil saturation modeled by TRIGRS, as a function of time, acts as a stronger constrain than the pore-pressure induction of the extreme event.

The back-analysis on the cohesion of different soil cover, indicate that in order to find a good correspondence between the observed and simulated instability, cohesion values of grass mantle and bare soil must be in the range of 500-3500 Pa (cases *c* and *d* in Fig. 5.12). On the other hand, if we run the model with the cohesion values measured in the field with the "turf's comb", and in laboratory (2000 - 50000 Pa, cases *e* and *f* in Fig. 5.12), it becomes clear that the instability is extremely reduced (0.7% of the total catchment area). Here, cells with FoS close or less than 1 are limited to bare soil pixels, lying on a non-flat topography. The model pictures erroneously as unstable also the pixels on the trails that cross the basin in the E-W direction; this effect is caused by the resolution of the DTM. With a 2 x 2 m cell resolution, which is wider than the real width of the trails, the cell incorporates also the steepness of the trail's flank. As a result, pixels on the trail, classified in the EO map as bare soil, results unstable even if they're located on a flat surface.

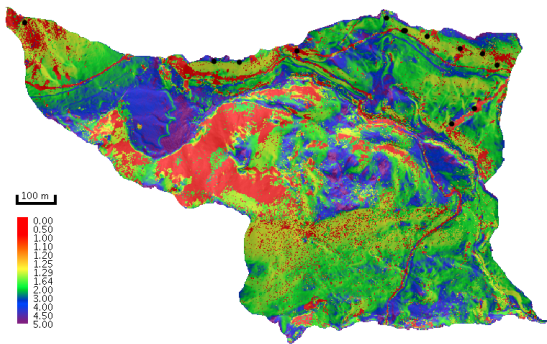
All the maps depict the central-west part of the basin on the northern side of the Col de l'Agnel mount as unstable, which does not match with the surveyed location of shallow landslides. Here, the grass mantle is heavily grazed (cohesion values are low, 500 - 1500 Pa, Table 5.4) but the shallow depth of the soil inhibits the landslide occurrence. TRIGRS (as well as SHALSTAB) indeed doesn't account for varying soil depth, which in this basin we proved to be a strong constrain in defining the potentially unstable soil volumes (see Chapter III).



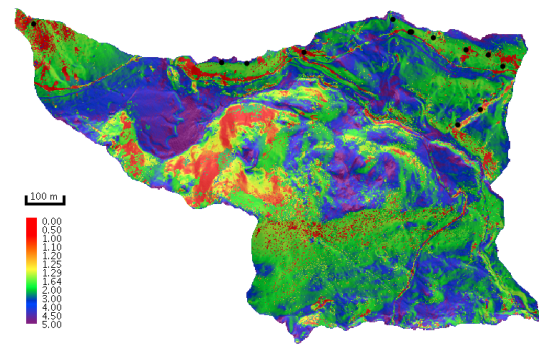
(a) Case 1



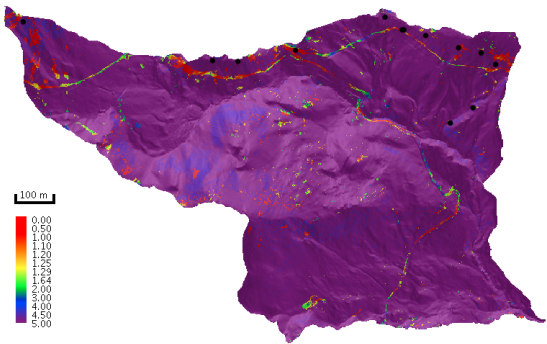
(b) Case 1



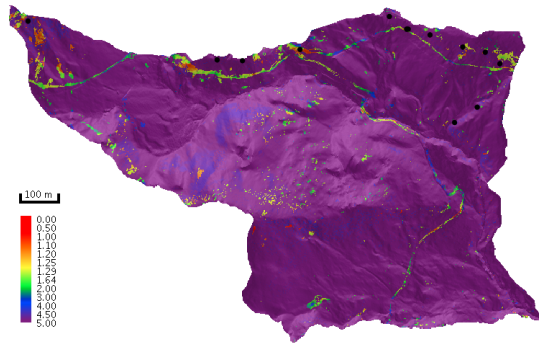
(c) Case 2



(d) Case 2



(e) Field Values



(f) Field values

Figure 5.12: TRIGRS simulation with the "Moena" precipitation (a,c,e) and the "extreme" one (b,d,f); blue dots represent the source areas and black pixels are cells with FoS less than one.

5.4 SLIDE

We used the software SLIDE (Rocscience) to perform a 2D limit equilibrium analysis of the effect of the *Nardetum* grass cover on the hillslope stability. Our analyses focused on the influence of grass mantle roots on the hillslope's factor of safety (FoS).

The analyses were carried out along a 37 m long section located in the north-eastern part of the study area, between the road connecting the Duron pass and "I Frati" location and the watershed divide (Fig. 5.13). The slope ranges between 15° and 35° with an average of 29° . Here the soil is 80 cm thick and the bedrock consists of fine-grained volcanic turbidites alternated with hyaloclastites. We consider this section representative of the hillslope conditions before the landslide event, since it is bounded eastward and westward by shallow landslides.

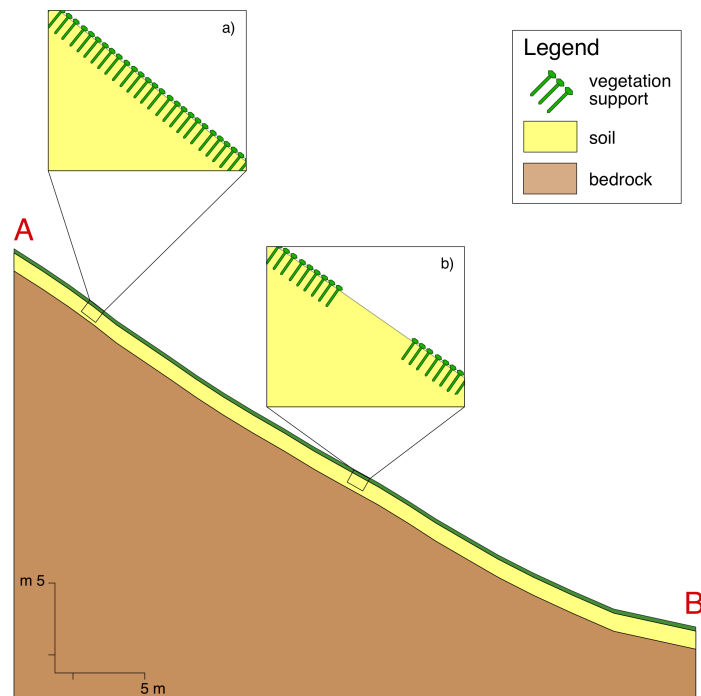


Figure 5.13: Section of the hillslope used for the SLIDE analyses; the two boxes represent the undamaged grass support (a) and the grazed one (b)

5.4.1 Vegetation cover

Turf's roots contribution to slope stability was simulated placing a geotextile support along the slope. We modeled two types of grass cover: the ungrazed turf and the grazed one. In the geotextile, each support represents a single root; in the case of an ungrazed turf, the supports (15 cm long) are spaced by 1 cm and they're set perpendicular to the topographic surface (Fig. 5.14). In order to simulate the soil architecture produced by cattle's grazing, the supports are spaced by 2 cm and we alternated spatially 30 cm of roots regularly spaced (as in the ungrazed turf), to 20 cm with no support (Fig.5.14). This solution was adopted to mimic the effect of the terracettes, where strips of grass are separated by bare soil (Fig. 2.1). The user defines the geotextile properties by setting the tensile strength of the support, which is the maximum load capacity, in force units, per meter width of strip.

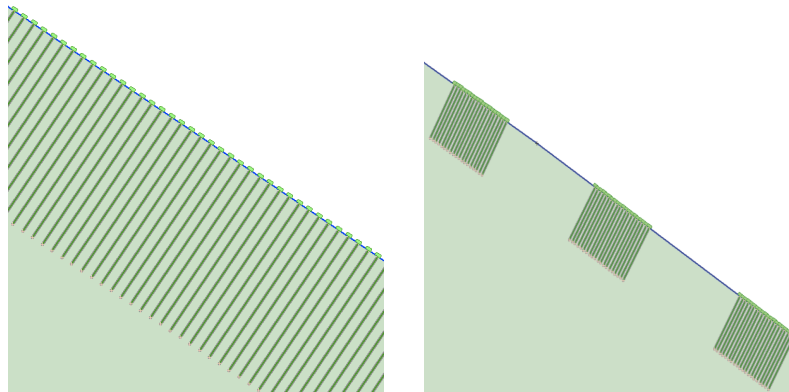


Figure 5.14: Ungrazed and grazed geotextile

5.4.2 Slope stability model

The factor of safety (FoS) is computed using the General Limit Equilibrium (GLE) method on a planar surface placed at 40 cm of depth; in SLIDE, the GLE is essentially equivalent

to the Morgenstern-Price method (Morgenstern and Price, 1965). Stresses and forces vary continuously across the slip; the equilibrium equation is formulated quite generally by solving normal and parallel to the base forces of each slice (Iverson, 1989). Given the sliding surface, the software computes the safety factor of the section. Since the section is located in the northeastern part of the basin, the friction angle is 31° , while we considered a cohesionless soil. This measure has been taken in order to isolate the effect of the tensile strengths of the two types of soil cover. The height of the water table is automatically calculated by the software, based on the inclination of the water surface above any given point of the section.

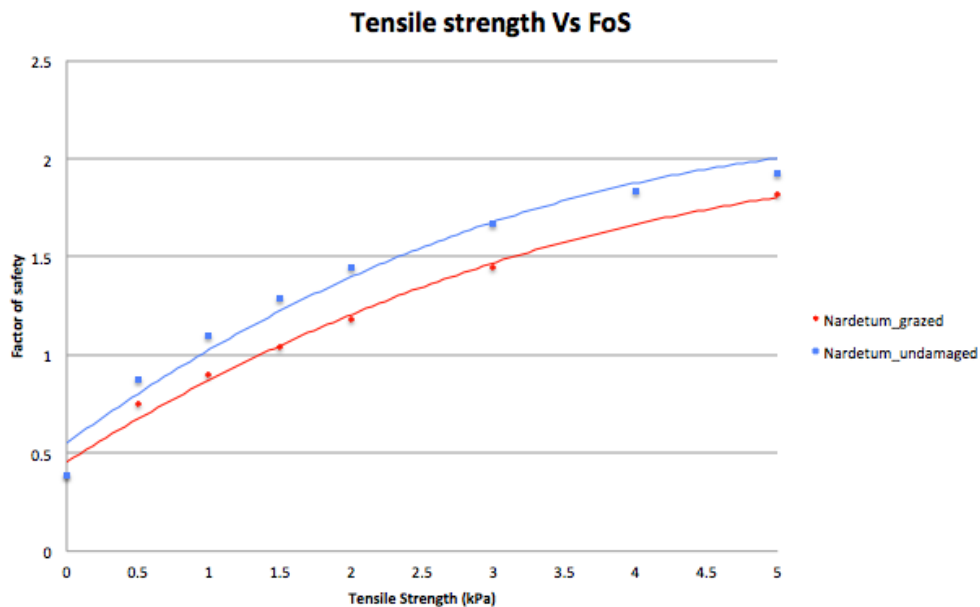


Figure 5.15: Factor of safety trends as a function of increasing support tensile strength for ungrazed grass (blue line) and grazed one (red line).

5.4.3 Results

SLIDE was used in back analysis, varying the tensile strength of the support from 0 to 10000 Pa until the critical condition is reached (FoS=1). The FoS trend as a function of varying

root tensile strengths is shown in Fig. 5.15. According to the back-analysis, the critical root tensile strength for the ungrazed turf resulted 1000 Pa while for the grazed one 1500 Pa. On the other hand, if we attribute no strength to the vegetation cover the factor of safety is lowered to 0.3.

5.5 Discussion

The instability scenarios depicted by the three models indicate that at the hillslope scale (SLIDE), the presence of the vegetation cover is fundamental for the stability and at the basin scale, SHALSTAB tends to overestimates the unstable areas while TRIGRS discriminate more realistically the instability.

All the three models were used in back-analysis, varying the input parameters within a reasonable range of values, function of the soil characteristics and land use conditions.

The SHALSTAB susceptibility map pictures 47% of the catchment's area as unstable, leading to the obvious conclusion that the model framework is not suited for these shallow mass movements. SHALSTAB captures beautifully the effects of topography in the shallow landslides distribution but holds strong limitations related to the steady state assumptions of its hydrological model (TOPOG). Moreover, the version of SHALSTAB we used, implemented on the JGrass platform, returns only the map of the instability divided for classes and doesn't allow choosing the output parameter (such as the classic q/T or the factor of safety).

According to the SHALSTAB analyses, at the critical condition (which should be interpreted as a the instant before the landslide is triggered), very little cohesion is needed (500-1500 Pa). Although the used cohesion values correspond to those used in literature on similar soils (Carrara et al., 2008), they differ markably from the values measured in the field on the land covers (approx. 20000 Pa and 30000 Pa for grazed areas and ungrazed grass respectively; see chapter IV).

Keeping in mind that shallow landsliding susceptibility does not forecast the timing or "how frequent" a landslide will occur (Guzzetti et al., 2006), the SHALSTAB instability distribution shall be interpreted as sites of likely failure in the future, if the same hydrological, geomorphological and geomechanical soil properties persist. Previous works (Simoni et al., 2008; Sorbino et al., 2010) underlined indeed the usefulness of using SHALSTAB as a guide for assessing the initial conditions for transient models (such as TRIGRS).

The EO-based map of the distributed cohesion values improved the model accuracy, even if only by three percentile points. In the source areas, which have been used to evaluate the model accuracy, 80% of the pixels fall into the ungrazed grass, 12% is bare soil, 6% is grazed grass and the remaining 2% are classified as trees and shadows. It is therefore the cohesion value of the most representative land cover class (ungrazed grass), which drives the validation of the model. In the EO land cover map, not all the pixels inside the source areas polygons are located on present-day bare soil or heavily grazed portions of the catchment. To explain this we should take into account the fact that the source areas represent an extremely small portion of the basin (0.4%) and, because of their small dimensions, they might not be representative and they could have suffered from misplacement errors, induced by the representation of these features on the map. Moreover, the EO land cover map has been produced on recent satellite images, while we have no information on the land cover condition when the landslides occurred.

TRIGRS-unsaturated computes a more sophisticated and complex analysis of the instability, introducing the effect of a transient rainfall in the infiltration model. The output however, is very sensitive to the hydrological initial conditions. The initial height of the water table was set at 0.25 m (half of the soil depth), which is a reasonable assumption, given the fact that, particularly in late spring, the investigated soils receive the contribution of the snowmelt-water.

From the simulations performed in different rainfall scenarios we obtained that:

(1) the geomechanical part of the model exerts a strong influence on the distribution of unstable cells. At the same precipitation rate, varying the cohesion within a small range of values (0-1500 Pa), caused a notable change in the number of unstable cells. Moreover, if we use the cohesion values measured in the field, the instability scenario changes dramatically: unstable cells reduce to 0.7 % of the entire catchment and their occurrence is limited to the bare soil class.

(2) keeping in mind that we're dealing with two different precipitation scenarios, which are related to two different time intervals, we cannot assess which one is the most critical. Our simulations suggest that, given the same initial hydrological conditions, the unstable cells are less sensitive to the short and extreme precipitation.

If we assume that the instability scenarios depicted by the model represent with good approximation the real conditions, the first-time landslide occurrence in this alpine context, depends mainly on the geomechanical properties of the soil-root system and the topography. The hydrological model becomes effective in discriminating the instability distribution, once the geomechanical parameters are lowered to residual values. On the other hand, landslide reactivations, which in different context, such as the Appennines represent more than 50% of the cases, is tightly bounded to the hydrological setting of the slopes.

SLIDE simulations represent the link between the effect of land use condition, which in the other models is divided in classes according to the EO-based map, and the slope stability. With SLIDE's back analysis we modeled the resistance of soil and roots in two land cover classes: the grazed grass and the ungrazed grass mantle. The attention here is therefore focused on the role of vegetation in the hillslope stability. With the back-analysis we obtained that the critical condition, expressed in terms of factor of safety, is reached when the root tensile strength is lowered to 1500 Pa and 1000 Pa for grazed and ungrazed grass mantle respectively. Grazed grass requires indeed more resistance (approx. 50%) to reach the stability conditions. Given the steady state conditions of this model, and neglecting at first instance

the different stability methods (infinite slope Vs GLE), SHALSTAB and SLIDE results can be compared to address the issue of grass mantle resistance at the hillslope and basin scale. The tensile strengths, used in the SLIDE simulations fall indeed within the same range of values of the SHALSTAB's back analysis cohesion values (1000 - 15000 Pa).

The TRIGRS analyses set a step forward, adding to the stability analysis the influence of time, expressed as the pore pressure change, induced by a transient rainfall. Our results suggest that if the soil is already close to saturation, as a result of a long precipitation event, the pore-pressure change, induced by a transient rainfall over a short time interval, doesn't change substantially the instability scenario.

The issue that needs to be tackled is which physical process determines the lowering of geomechanical characteristics in this alpine environment. Resistances values measured in the field (see Chapter III) clearly indicate that these alpine soils, and their relative vegetation covers (see Chapter IV), have extremely good geomechanical properties. On the other hand, the resistance values calculated in back analysis show a remarkable discrepancy with the field data.

The decay of the geomechanical properties of these soil is mainly driven, through time, by physical processes such as freeze/thaw cycles and mechanical weathering by water percolation. The velocity of the decay increases if these processes are combined with the mechanical degradation of the grass mantle caused by the hooves of cattle's animals. However, measuring the decay of these properties trough time is outside the aim of this study, since different instruments and sensors would be needed.

5.6 Conclusions

Slope stability analyses performed in the study area acknowledge the high instability of the entire catchment, in the long term analysis, and, at the hillslope's scale, the fundamental

role of the grass mantle condition. More than 20% of the study area suffers from intensive grazing of cows and horses, whose damaging effect lowers the geomechanical properties of the grass mantle. The back-analysis revealed indeed that the grazed portion of the catchment requires 30% more resistance than undamaged grass mantle.

Introducing the EO-based map of the land covers in the stability analyses proved to be a useful tool in discriminating the portions of the land with similar land use conditions. This classified map increased the accuracy of the distribution of cohesion values, providing a user-independent approach to distribute the cohesion parameters across the landscape.

5.7 References

Baum, R.L., Savage, W.Z., and Godt, J.W., 2002, TRIGRS—A Fortran program for transient rainfall infiltration and grid-based regional slope stability analysis: U.S. Geological Survey Open-File Report 02-0424, 35 p., 2 appendices.

Baum, R.L., Savage, W.Z., Godt, J.W., (2008). TRIGRS-A Fortran program for transient rainfall infiltration and grid-based regional slope-stability analysis, version 2.0. US Geological Survey Open-File Report 2008-1159. Available via: <http://pubs.usgs.gov/of/2008/1159/>

Begueria, S., 2006. Validation and evaluation of predictive models in hazard assessment and risk management. *Natural Hazards*, 37(3): 315-329.

Carrara, A., Crosta, G. and Frattini, P., 2008. Comparing models of debris-flow susceptibility in the alpine environment. *Geomorphology*, 94(3-4): 353-378.

Casadei, M., Dietrich, W.E. and Miller, N.L., 2003. Testing a model for predicting the timing and location of shallow landslide initiation in soil-mantled landscapes. *Earth Surface Processes and Landforms*, 28(9): 925-950.

Dietrich, W. E., Wilson, C. J., Montgomery, D. R., McKean, J., and Bauer, R., 1992. Channelization Thresholds and Land Surface Morphology. *Geology*, v.20, p. 675-679.

Dietrich, W. E., Wilson, C. J., Montgomery, D. R., McKean, J., 1993. Analysis of Erosion Thresholds, Channel Networks and Landscape Morphology Using a Digital Terrain Model. *Journal of Geology*, v. 101, p. 259-278

Guzzetti, F., Reichenbach, P., Ardizzone, F., Cardinali, M. and Galli, M., 2006. Estimating the quality of landslide susceptibility models. *Geomorphology*, 81(1): 166-184.

Iverson, R.M., 1989. Slope stability—geotechnical engineering and geomorphology, M. G. Anderson and K. S. Richards (Eds), Wiley, Chichester, 1987. No. of pages: 648. *Earth Surface Processes and Landforms*, 14(3): 271-271.

Iverson, R.M., 2000. Landslide triggering by rain infiltration. *Water Resources Research*, 36(7): 1897-1910.

Li, T.D. and Zhao, Z.S., 1984. A Method of Back Analysis of the Shear Strength Parameters for the First Time Slide of the Slope of Fissured Clay. *Proceedings 4th International Symposium on Landslides*, Toronto, 2, pp. 127-129. Quennell, AM, 1951.

Montgomery, D.R. and Dietrich, W.E., 1994. A physically-based model for the topographic control on shallow landsliding. *Water Resources Research*, 30(4): 1153-1171.

Morgenstern, N.R., and Price, V.E., 1965. The analysis of the stability of general slip surfaces. *Géotechnique*, 15(1): 79–93.

O’Callaghan, J.F. and Mark, D.M., 1984. The extraction of drainage network from digital elevation data. *Computer Vision, Graphics, and Image Processing*, 28(3): 323-344.

O’Loughlin, E. M., Prediction of surface saturation zones in natural catchments by topographic analysis, *Water Resources Research*, 2 2: 794-804, 1986.

Schaap, M.G., Leij, F.J. and van Genuchten, M.T., 2001. ROSETTA: a computer program for estimating soil hydraulic parameters with hierarchical pedotransfer functions. *Journal of Hydrology*, 251(3-4): 163-176.

Simoni, S., Zanotti, F., Bertoldi, G. and Rigon, R., 2008. Modelling the probability of occurrence of shallow landslides and channelized debris flows using GEOtop-FS. *Hydrological Processes*, 22(4): 532-545.

Sorbino, G., Sica, C. and Cascini, L., 2010. Susceptibility analysis of shallow landslides source areas using physically based models. *Natural hazards (Dordrecht)*, 53(2): 313-332.

Tarboton, D.G., 1997. A new method for the determination of flow directions and upslope areas in grid digital elevation models. *Water Resources Research*, 33(2): 309-319.

Taylor, D. W., 1948. *Fundamentals of Soil Mechanics*. Wiley, New York.

CHAPTER 6

Conclusions

Throughout the alpine domain, shallow landslides represent a serious geologic hazard, often causing severe damages to infrastructures, private properties, natural resources and in the most catastrophic events, threatening human lives. Landslides are a major factor of landscape evolution in mountainous and hilly regions and represent a critical issue for mountainous land management, since they cause loss of pastoral lands.

In the alpine environment subject of this study, understanding the triggering mechanisms of shallow landslides must go hand-in-hand with the study of the geomechanical properties of the land covers.

The study area represents a unique place to investigate the land cover properties, because it's one of the few undamaged alpine environment in the eastern Dolomites, that hasn't been yet exploited as ski resort.

All the data collected in the past years provided us with an exclusive database of geomechanical and geotechnical data of the soils and the vegetation cover. The innovative technologies, which were tested in collecting these measurements, proved to be very effective and pictured clearly the strength of this grass mantle (Nardetum).

Preliminary data obtained with the "Turf's comb" device, show that the peak shear strength of undisturbed soil-vegetation blocks is very high, and might exceed 3.0 N/cm^2 . These contributions strongly increase the stability of the soils covering the steep (35° - 40°) hillslopes of the Duron valley and revealed that the root's anchoring contribution can be effective up to a depth of 20 cm or more.

The Duron catchment exhibits regions where the grass mantle is deeply damaged by the intensive grazing activity, which has been going on for the past centuries. Prolonged grazing is responsible for lowering the exceptional geomechanical properties of the grass mantle (*Nardetum*); its effects are visible even in high-resolution satellite images. The "turf's comb" device revealed that grazed portion of the catchment, which occupy 20% of the total area, have a shear resistance 30% lower than undamaged grass mantle.

Using satellite images classification, the damaged portions of the basin can be successfully identified. The proposed classification method combines the NDVI map, the co-occurrence measure and the multispectral bands, and proved to be successful in discriminating portions of the catchment with different geomechanical properties, such as the grazed pasture land from the ungrazed ones.

All the data collected using different methods and techniques were merged into a shallow landsliding stability analysis. Three models were used in back analysis to investigate the instability distribution across the study area.

The results confirmed the high instability of the entire catchment, in the long-term analysis, and, at the hillslope's scale, the fundamental role of the grass mantle condition; also the model's back-analysis simulation revealed that the grazed portions of the catchment, in order to reach a stability condition, require a resistance 30% greater than undamaged grass mantle.

Introducing the EO-based map of the land covers in the stability analyses proved to be a useful tool in discriminating the portions of the land with similar cohesion contribution. Finally, the use of EO-classified maps provides a user-independent approach to assign the cohesion parameters across the territory.